Numerical simulations of the effects of tarpaulin billowing on phosphine movement in bulk-stored grain

by

Sherif Mohamed Gomaa Elsayed

B.S., Cairo University, 2009

M.S., Cairo University, 2015

AN ABSTRACT OF A DISSERTATION

submitted in partial fulfillment of the
requirements for the degree

DOCTOR OF PHILOSOPHY

Alan Levin Department of Mechanical and Nuclear Engineering
Carl R. Ice College of Engineering

KANSAS STATE UNIVERSITY
Manhattan, Kansas

2023

Abstract

Bunker storage is an inexpensive, and thus popular, method for medium- and long-term storage of wheat. To control insect infestations in bunker storages, phosphine (PH_3) fumigant is commonly used, especially in Australia, due to its relatively low price and the near absence of residual chemicals on the grain. Understanding the behavior of phosphine gas inside bunkers is crucial to maintaining a lethal dosage and protecting stored grain from subsequent insect damage.

Gases in bunkers experience pressure drop and a change in velocity due to the presence of wheat. In Computational Fluid Dynamics (CFD) simulations, wheat kernels are not modeled explicitly in the geometry, rather their effect in terms of pressure loss is considered in the governing equations. This study reviews the wheat resistance to gas flow and its characteristics. Physical properties of the isotropic and anisotropic resistances were discussed. Proper coefficients that reasonably describe the presence of wheat in CFD models were chosen. This is important to understand the fumigant distribution in a grain storage facility. To test the implementation of these coefficients in CFD simulations, a CFD model was built and the results agreed well with the published empirical correlations. Detailed explanations on the governing equations used in all the simulations were also discussed. A new technique in obtaining the resistance coefficients without the need for any experimental work was proposed and verified against published experimental data.

Phosphine is available either in gas form or is produced from a solid material, as pellets or tablets of aluminum or magnesium phosphide, that react with moisture in the air. The solid form is the most commonly used; however, limited information is available on the rate of phosphine gas generated from the solid material. In this study, a mathematical equation was formulated, based on previous studies in the literature, to describe the gas generation rate. This equation was incorporated into a CFD model. The computational model developed

here allows prediction of the phosphine concentration within a fumigated grain bulk. The PH_3 sorption was included in the model. The effect of temperature on the sorption rate was investigated based on published data, and the rate change due to temperature was characterized. To validate the model, the gas generated by a single pellet was measured in laboratory experiments in a $0.208\,m^3$ sealed barrel. The measurements confirmed the CFD results with an error of 0.3%, 0.9%, and 7.2% for three different configurations. The deviations seen between the experimental replicates increased the error and showed the need for further investigation of the effects of temperature, grain age and history, leakage, and other factors.

For fumigation to be effective, a lethal concentration of PH_3 for a minimum time period at an optimal temperature throughout the bunker must be ensured. Because bunkers are exposed to ambient conditions, temperature gradients are created throughout the bunker, resulting in natural convection currents that move PH_3 from areas around the fumigation points to the entire bunker. CFD simulations were used to investigate the effect of natural convection on fumigation in bunkers. The model was validated against published benchmarks and a field experiment with a full-scale bin with sorption and leakage. The effects of PH_3 release point locations, bunker shape, bunker orientation, leakage, sorption, ambient temperature fluctuation, and PH_3 motion in three dimensions were studied. Results showed that diffusion and natural convection solely are insufficient in spreading out PH_3 within bunkers.

In addition to diffusion and convection currents, the internal flows driven by the movements of the covering tarpaulin due to the external flow over the bunker, distribute the PH_3 gas. This study also aims to describe the effect of tarpaulin movement on the PH_3 behavior inside bunkers. The motion mechanism of the tarpaulin was investigated using Fluid-Structure Interaction (FSI) simulations under different wind conditions. The FSI study was validated against published benchmarks. The dominant motion of the tarpaulin was then simplified and built in a CFD model with non-linear moving boundaries to study its effect on the PH_3 distribution. Results were concluded using a Deep Neural Network (DNN) model. Results showed that tarpaulin motion, as a free source, can immensely improve the fumiga-

tion effectiveness, if controlled properly. A small change in the motion parameters resulted in a very different PH_3 distribution and a different enhancement rate. The challenges on unifying a certain motion with certain parameters on the currently built bunkers such as the smoothness of the grain surface, the looseness and tightness of the tarpaulin with the side walls of the bunker, etc. were discussed. Highlights on the importance of building a more controlled and semi-sealed tarpaulin mechanism were pointed out.

Numerical simulations of the effects of tarpaulin billowing on phosphine movement in bulk-stored grain

by

Sherif Mohamed Gomaa Elsayed

B.S., Cairo University, 2009

M.S., Cairo University, 2015

A DISSERTATION

submitted in partial fulfillment of the
requirements for the degree

DOCTOR OF PHILOSOPHY

Alan Levin Department of Mechanical and Nuclear Engineering
Carl R. Ice College of Engineering

KANSAS STATE UNIVERSITY
Manhattan, Kansas

2023

Approved by:

Co-Major Professor
Mark E. Casada

Approved by:

Co-Major Professor
Mingjun Wei

Approved by:

Co-Major Professor
Ronaldo G. Maghirang

Copyright

Abstract

Bunker storage is an inexpensive, and thus popular, method for medium- and long-term storage of wheat. To control insect infestations in bunker storages, phosphine (PH_3) fumigant is commonly used, especially in Australia, due to its relatively low price and the near absence of residual chemicals on the grain. Understanding the behavior of phosphine gas inside bunkers is crucial to maintaining a lethal dosage and protecting stored grain from subsequent insect damage.

Gases in bunkers experience pressure drop and a change in velocity due to the presence of wheat. In Computational Fluid Dynamics (CFD) simulations, wheat kernels are not modeled explicitly in the geometry, rather their effect in terms of pressure loss is considered in the governing equations. This study reviews the wheat resistance to gas flow and its characteristics. Physical properties of the isotropic and anisotropic resistances were discussed. Proper coefficients that reasonably describe the presence of wheat in CFD models were chosen. This is important to understand the fumigant distribution in a grain storage facility. To test the implementation of these coefficients in CFD simulations, a CFD model was built and the results agreed well with the published empirical correlations. Detailed explanations on the governing equations used in all the simulations were also discussed. A new technique in obtaining the resistance coefficients without the need for any experimental work was proposed and verified against published experimental data.

Phosphine is available either in gas form or is produced from a solid material, as pellets or tablets of aluminum or magnesium phosphide, that react with moisture in the air. The solid form is the most commonly used; however, limited information is available on the rate of phosphine gas generated from the solid material. In this study, a mathematical equation was formulated, based on previous studies in the literature, to describe the gas generation rate. This equation was incorporated into a CFD model. The computational model developed

here allows prediction of the phosphine concentration within a fumigated grain bulk. The PH_3 sorption was included in the model. The effect of temperature on the sorption rate was investigated based on published data, and the rate change due to temperature was characterized. To validate the model, the gas generated by a single pellet was measured in laboratory experiments in a $0.208\,m^3$ sealed barrel. The measurements confirmed the CFD results with an error of 0.3%, 0.9%, and 7.2% for three different configurations. The deviations seen between the experimental replicates increased the error and showed the need for further investigation of the effects of temperature, grain age and history, leakage, and other factors.

For fumigation to be effective, a lethal concentration of PH_3 for a minimum time period at an optimal temperature throughout the bunker must be ensured. Because bunkers are exposed to ambient conditions, temperature gradients are created throughout the bunker, resulting in natural convection currents that move PH_3 from areas around the fumigation points to the entire bunker. CFD simulations were used to investigate the effect of natural convection on fumigation in bunkers. The model was validated against published benchmarks and a field experiment with a full-scale bin with sorption and leakage. The effects of PH_3 release point locations, bunker shape, bunker orientation, leakage, sorption, ambient temperature fluctuation, and PH_3 motion in three dimensions were studied. Results showed that diffusion and natural convection solely are insufficient in spreading out PH_3 within bunkers.

In addition to diffusion and convection currents, the internal flows driven by the movements of the covering tarpaulin due to the external flow over the bunker, distribute the PH_3 gas. This study also aims to describe the effect of tarpaulin movement on the PH_3 behavior inside bunkers. The motion mechanism of the tarpaulin was investigated using Fluid-Structure Interaction (FSI) simulations under different wind conditions. The FSI study was validated against published benchmarks. The dominant motion of the tarpaulin was then simplified and built in a CFD model with non-linear moving boundaries to study its effect on the PH_3 distribution. Results were concluded using a Deep Neural Network (DNN) model. Results showed that tarpaulin motion, as a free source, can immensely improve the fumiga-

tion effectiveness, if controlled properly. A small change in the motion parameters resulted in a very different PH_3 distribution and a different enhancement rate. The challenges on unifying a certain motion with certain parameters on the currently built bunkers such as the smoothness of the grain surface, the looseness and tightness of the tarpaulin with the side walls of the bunker, etc. were discussed. Highlights on the importance of building a more controlled and semi-sealed tarpaulin mechanism were pointed out.

Table of Contents

List of Figures xiv

List of Tables xxiii

Acknowledgements xxiv

Dedication xxv

1 Introduction 1

2 Numerical Description 6

2.1 Objective 6

2.2 Wheat resistance to gas flow - a literature review 6

2.2.1 Ergun Equation 8

2.2.2 Factors affecting the resistance to airflow 12

2.2.2.1 Moisture content 12

2.2.2.2 Filling method 13

2.2.2.3 Foreign material 14

2.2.2.4 Direction of the flow 14

2.2.3 Implementation test 17

2.3 Governing equations 19

2.3.1 Effective diffusion coefficient 23

2.4 Estimating resistance coefficients 24

3 Releasing Rate of Phosphine 30

3.1 Objective . . . 30
3.2 Relationship for Evolution Rate . . . 30
3.3 CFD Model Development . . . 36
3.3.1 Empty volume . . . 36
3.3.1.1 Experiment . . . 36
3.3.1.2 Simulation . . . 36
3.3.1.2.1 Grid test . . . 38
3.3.1.2.2 Time-step test . . . 38
3.3.2 Wheat-filled volume . . . 39
3.3.2.1 Effect of sorption . . . 40
3.3.2.1.1 Sorption validation . . . 41
3.3.2.2 Simulation and validation . . . 43

4 Phosphine Movement in Bulk-stored Grain . . . 47
4.1 Objective . . . 47
4.2 CFD Models . . . 48
4.2.1 Validation . . . 48
4.2.1.1 Benchmark validation . . . 48
4.2.1.2 Experimental validation . . . 50
4.3 Bunker model . . . 58
4.3.1 Grid refinement and time-step tests . . . 62
4.3.2 CFD Results . . . 63
4.3.2.1 Standard case and effect of convection currents . . . 64
4.3.2.2 Tablet location . . . 66
4.3.2.3 Aspect ratio . . . 67
4.3.2.4 Side wall height . . . 69
4.3.2.5 Leakage . . . 70
4.3.2.6 Bunker orientation . . . 71

4.3.2.7 Diurnal temperature variation . . . 72
4.3.2.8 Phosphine sorption . . . 73
4.3.2.9 Combined diurnal variation, leakage, & sorption . . . 74

5 Effect of Tarpaulin Billowing on Phosphine Behavior . . . 77
5.1 Objective . . . 77
5.2 FSI - external flow . . . 78
5.2.1 Benchmark validation . . . 79
5.2.1.1 Oscillating plate . . . 79
5.2.1.2 Flag . . . 81
5.2.2 Bunker model . . . 85
5.2.2.1 Choosing a slice (CFD) . . . 85
5.2.2.2 FSI simulation . . . 88
5.2.2.2.1 Grid and time-step tests . . . 90
5.2.2.2.2 Constant inlet velocity . . . 91
5.2.2.2.3 Effect of Reynolds number . . . 92
5.2.2.2.4 Oscillating inlet velocity . . . 93
5.2.2.2.5 Multiple bunkers . . . 95
5.3 Dynamic walls – internal flow . . . 97
5.3.1 Equation for tarpaulin motion . . . 97
5.3.2 Bunker with moving boundaries . . . 99
5.3.2.1 Effect of headspace . . . 102
5.3.2.2 Effect of leakage . . . 103
5.3.2.3 Effect of tarpaulin billowing . . . 104
5.3.3 Predicting the mortality fraction . . . 105

6 Summary and Conclusion . . . 111
6.1 Significance and contribution . . . 115

6.2 Limitations 116
6.3 Recommendations for future work 116

Bibliography 118

A Extra Material 129
A.1 Inhomogeneous porosity with anisotropic resistance 129
A.2 Corn resistance to airflow - CFD test 130

List of Figures

2.1 Pressure drop per unit length ($\mathrm{Pa\,m^{-1}}$) vs air velocity ($\mathrm{m\,s^{-1}}$); a comparison between Eq. 2.9 (——) and published data of Hood and Thorpe (1992) (——), Molenda et al. (2005a) (- - -), and Li and Sokhansanj (1994) (-·-·). . . . 11

2.2 Pressure drop per unit length ($\mathrm{Pa\,m^{-1}}$) vs air velocity ($\mathrm{m\,s^{-1}}$) at 12.7% moisture content with funnel filling method (Molenda et al., 2005a) (-·-·) in comparison with results of Shedd (1953) (——), Ergun (1952) (- - -), and Hukill and Ives (1955) (- - -). 11

2.3 Pressure drop per unit length ($\mathrm{Pa\,m^{-1}}$) vs air velocity ($\mathrm{m\,s^{-1}}$) using resistances coefficients of Hood and Thorpe (1992) (——) and at the minimum (——) and maximum (- - -) porosity using constants of Molenda et al. (2005a). 17

2.4 Contours of superficial velocity (a), true velocity (b), and pressure (c) along with a comparison (d) between the pressure drop per unit length ($\mathrm{Pa\,m^{-1}}$) vs velocity ($\mathrm{m\,s^{-1}}$) between the CFD results (◆), results of Eq. 2.5 (——) with Hood and Thorpe (1992) coefficients, and Darcy's (1856) model (- - -). . . 19

2.5 Comparison between different definitions for the effective diffusion coefficient of PH_3 in wheat. 24

2.6 Different views of the wheat kernel with dimensions obtained from a 3D scanned image – before and after cleaning. 25

2.7 Three different periodic patterns obtained from the wheat kernel; (a) horizontal flow, (b) vertical flow, (c) flow from the side of the kernel, and (d) one period from each orientation (a, b, c). 25

2.8 Computational domain with boundary conditions for four different orientations of wheat kernels; (a) horizontal flow, (b) flow from the side of the kernel, (c) vertical flow, and (d) two layers of the vertical flow orientation. 26

2.9 Mosaic mesh (polyhedral and hexahedral) generated for the two layers scenario. 27

2.10 Contours of static pressure (Pa) resulted from the CFD simulation; (a) horizontal flow, (b) flow from the side of the kernel, (c) vertical flow, and (d) two layers of the vertical flow orientation. 27

2.11 Pressure drop per unit length ($\mathrm{Pa\,m^{-1}}$) versus the magnitude of the velocity ($\mathrm{m\,s^{-1}}$) in each flow direction; vertical (—●—), horizontal (- -■- -), and side (- -▲- -). 28

2.12 Pressure drop per unit length ($\mathrm{Pa\,m^{-1}}$) versus the magnitude of the velocity ($\mathrm{m\,s^{-1}}$) for three different kernel sizes (original —●—, small - -■- -, large - -▲- -) of flow from vertical direction. 29

2.13 Comparison between the experimental data of Molenda et al. (2005a) at two different porosities (Red Wheat $\varepsilon = 0.35$ ——, Red Wheat $\varepsilon = 0.45$ - - -, White Wheat $\varepsilon = 0.35$ ——, and White Wheat $\varepsilon = 0.45$ - - -) that represents the heights and lowest pressure drop observed from the experiment and results from the CFD model of the two layers scenario as the maximum resistance (- -●- -) and the flow from the side case that represents the minimum resistance (—●—) obtained. 29

3.1 Maximum phosphine released from ten AlP tablets at different temperature and relative humidity levels for the experimental data from Tan (1994) (symbols) and the results from Eq. 3.1 (——). 32

3.2 Evolution rate of PH_3 ($\mathrm{g\,h^{-1}}$) from ten AlP tablets versus time (s) at different temperature and relative humidity levels for data from Tan (1994) (·····) and results from Eq. 3.4 (——). 34

3.3 Time for partial phosphine release (10%, 50%, and 90%) from 1 g of PH_3 between results of Eq. 3.4 I and experimental data of Tan (1994) ◆ & Couch and Shaheen (1984) ◉. Data from Tan were available at 20 °C and 50% *RH* and at 20 °C and 90% *RH*, while data from Couch and Shaheen were available as a range for 85% to 95% *RH* with multiple trials but with a fixed value for 45% to 55% *RH* with one trial. 35

3.4 Dimensions of the barrel used in laboratory experiments, computational domain for the empty case, and boundary conditions (not to scale). 37

3.5 Structure mesh generated for the barrel simulation, zoomed-in around the AlP pellet. 37

3.6 PH_3 concentration (ppm), at a distance of 12.5 cm from the bottom of the barrel, with (a) three different mesh sizes (fine —, medium - - -, coarse ·····) and (b) three different time-steps (15 s —, 30 s - - -, 60 s ·····). 38

3.7 Comparison between CFD results (T = 29 °C — and T = 33 °C - - -) and experimental data (T = 29 °C ▲, T = 30 °C ×, and T = 33 °C ●) based on PH_3 concentration (ppm) versus time (h). 39

3.8 PH_3 adsorption by wheat at different temperatures based on CFD results (lines) and Darby's (2008; 2011) experimental data (symbols). 42

3.9 Schematic and dimensions of the experimental setup (not to scale). 43

3.10 Comparison between CFD results (T = 29 °C — and T = 33 °C - - -) and experimental data (T = 29 °C ▲, T = 32 °C ×, and T = 33 °C ●) for the half-filled case based on PH_3 concentration (ppm) versus time (h). 44

3.11 Comparison between CFD results (T = 29 °C — and T = 33 °C - - -) and experimental data (T = 30 °C ▲, T = 32 °C ×, and T = 33 °C ●) for the full of wheat case based on PH_3 concentration (ppm) versus time (h). 44

3.12 Comparison of the experimental data for the full (—) and half-filled (- - -) with wheat cases based on PH_3 concentration (ppm) versus time (h) at T = 32 °C. 46

3.13 Contours of PH_3 concentration (ppm) at T = 24 h in each case: (a) empty (Sec. 3.3.1), (b) half-filled (Sec. 3.3.2), and (c) full of wheat (Sec. 3.3.2). . . . 46

4.1 Isotherms from Baytas and Pop (1999) at Ra_m = 1000 (a), compared to results from this work (b). . . . 50

4.2 Computational domain of the bin with all details. . . . 51

4.3 Mosaic (polyhedral and hexahedral) mesh for the bin simulation. . . . 52

4.4 Free stream velocity ($m\,s^{-1}$) (——) and temperature (°C) (- - -) along with the windrose at a location near the bin. . . . 52

4.5 Local heat transfer coefficient ($W\,m^{-2}\,K^{-1}$), top view, at 120 h resulted from the external flow model of the bin. . . . 54

4.6 The average heat transfer coefficient ($W\,m^{-2}\,K^{-1}$) from the CFD results (——) of the external flow model of the bin compared to results of the empirical correlation of Žukauskas (1972) (- - -). . . . 54

4.7 Temperature contours (°C) along with velocity vectors for the steady state model of the bin. . . . 56

4.8 The average PH_3 concentration (ppm) between the CFD results of the main model at three different depths (0.4 m ——, 1.1 m - - -, and 1.8 m -·-·) of the bin and the experimental data at the same three depths (0.4 m ○, 1.1 m ▲, and 1.8 m ■). . . . 57

4.9 Contours plots at North-South section (NS) of PH_3 (ppm) from both the CFD results of the bin model (left) and the experimental data (right) at t = 24 h. . . 57

4.10 Contours plots at East-West section (EW) of PH_3 (ppm) from both the CFD results of the bin model (left) and the experimental data (right) at t = 24 h. . . 58

4.11 2D bunker shape with the dimensions used for the simulation. The drawing indicates four different configurations (C1 – C4) for the PH_3 location; highlighted in green. . . . 59

4.12 Boundary conditions used for the bunker simulation with the PH_3 evolution rate curve (—) of 102 AlP tablets at $T = 45\,°C$. Line S (- - -) is for the grid and time-step tests. 59
4.13 Structured mesh generated for the bunker simulation, zoomed-in at the left PH_3 location and the corner. 59
4.14 Computational domain along with the dimensions for the 3D bunker case. . . 61
4.15 Mosaic (polyhedral and hexahedral) mesh for the 3D bunker simulation with inflation layers. 62
4.16 Velocity magnitude ($m\,s^{-1}$) along segment S with three different mesh sizes (coarse —, medium - - -, fine —). 62
4.17 PH_3 concentration along segment S at 24 h with three different time-steps (90 s —, 60 s - - -, 1 s —). 63
4.18 Temperature contours (°C) of the 2D bunker at three different modified Rayleigh numbers; (a) $Ra_m = 0$, (b) $Ra_m = 100$, and (c) $Ra_m = 1000$. 65
4.19 Plots of the velocity vector ($m\,s^{-1}$) (a) and the streamlines (b). 65
4.20 PH_3 concentration (ppm) for pure diffusion case (a, b) and diffusion + convection (c, d) at 24 h and 48 h. 66
4.21 PH_3 concentration (ppm) at three different locations of the AlP tablets at 24 h (a, b, c) and 48 h (d, e, f). 67
4.22 PH_3 concentration (ppm) for the case with ARH = 1.00 (a, c) and $ARH = 0.25$ (b, d) at 24 h (a, b) and 48 h (c, d). 68
4.23 Velocity magnitude ($m\,s^{-1}$) at segment S for the three different ARHs (0.25 —, 0.50 - - -, 1.00 - · - · -). 68
4.24 PH_3 concentration (ppm) for the case with $ARh = 0.20$ (a, c) and $ARh = 0.05$ (b, d) at 24 h (a, b) and 48 h (c, d). 69
4.25 Velocity magnitude ($m\,s^{-1}$) at segment S for the three different ARhs (0.05 —, 0.10 - - -, 0.20 - · - · -). 70

4.26 PH_3 concentration (ppm) resulted from different leakage rates at two 24 h (a – f) and 24 h (g – l). 71
4.27 Contours of temperature (°C) (a, b, c) and PH_3 concentration (ppm) (d, e, f) illustrating the effect of bunker orientation for three different cases, T_1, T_2, and T_3 detailed in Table 4.2. 72
4.28 Contours of velocity ($m\,s^{-1}$) and streamlines (a), temperature (°C) (c), PH_3 concentration (ppm) at 24 h and 48 h (b, d) for the T_4 scenario. 72
4.29 The effect of temperature fluctuation; (a) contours of velocity ($m\,s^{-1}$) and streamlines, (c) temperature (°C), (b and d) PH_3 concentration (ppm) at 24 h and 48 h, respectively. 73
4.30 PH_3 contours (ppm) at 24 h (a) and 48 h (b) for the sorption case. 74
4.31 The exponential change in PH_3 (ppm) with time (h) due to absorption resulted from a hypothesis scenario of a 2D bunker that is initially at 400 ppm concentration everywhere in the domain with no AlP tablets in the governing equations. 74
4.32 PH_3 contours (ppm) at 24 h (a) and 48 h (b) for a case with sorption, 0.001 $m\,s^{-1}$ leakage, and sinusoidal temperature as boundary conditions. 75
4.33 PH_3 concentration (ppm) for the 3D results; (a) top view at 1.5 m height (b) lateral side view at the center, (c) longitudinal side view in the middle, and (d) longitudinal side view that cuts through the PH_3 release points. 76

5.1 Computational domain along with the boundary and initial conditions for the oscillating plate case of Glück et al. (2001) used for validation. 80
5.2 Structure mesh created for the oscillating plate problem with zoom-in around the flexible plate. 80
5.3 The change in the x–displacement (m) with time (s) at the tip of the flexible plate; a comparison between this study (—) against results of Glück et al. (2001) (●) and Namkoong et al. (2005) (□). 81

5.4 Computational domain, boundary and initial conditions, and fluid and solid properties used for the second validation scenario of Turek and Hron (2006). . 82
5.5 Hexahedral mesh generated in the vicinity of the cylinder and a segment of the flexible structure. 82
5.6 The dimensionless y–displacement ($\frac{\xi_y}{D}$) at the dimensionless time ($\frac{t\overline{U}}{D}$) between the current work (—) and results of Turek and Hron (2006) (●). 84
5.7 The dimensionless x–displacement ($\frac{\xi_x}{D}$) at the dimensionless time ($\frac{t\overline{U}}{D}$) between the current work (—) and results of Turek and Hron (2006) (●). 84
5.8 Vorticity contours obtained from this study at a dimensionless time of 13.6 s and 13.8 s show the fluid response to the motion of the flexible plate. 85
5.9 Top-view illustration of the three bunker orientations for the external flow model. 86
5.10 Section of the mesh generated for the $AoA0^\circ$ CFD model. 87
5.11 Pressure coefficient on the tarpaulin surface of a bunker at different orientations; 0° (a), 45° (b), and 90° (c). 88
5.12 The computational domain, boundary conditions, and fluid and solid properties used for the FSI bunker simulations. 89
5.13 Structure mesh generated in the fluid domain for the FSI bunker simulation with zooming in at two locations showing the gradual increase in the mesh size as it moves away from the bunker bottom and the bunker walls. 90
5.14 The dimensionless y–displacement ($\frac{\xi_y}{H}$) at three points ($p-$ —, $p0$ -·-·, $p+$ - - -), the frequency (Hz) of the y–displacement at point $p0$ (●), and the drag and lift forces per unit depth (N m^{-1}) (—) at the left wall of the tarpaulin resulted from the constant inlet velocity case versus time (s). 92
5.15 The dimensionless y–displacement ($\frac{\xi_y}{H}$) at point $p0$ at three Reynolds numbers of 1×10^5 (—), 5×10^5 (- - -), and 2×10^6 (-·-·) versus time (s). 93

5.16 The dimensionless y–displacement ($\frac{\xi_y}{H}$) at three points located on the left side of the tarpaulin ($p-$ ——, $p0$ ·-·-·, and $p+$ - - -) resulted from the oscillating inlet velocity case versus time (s). 93

5.17 The motion mechanism of the tarpaulin at different times resulted from the oscillating inlet velocity case. 94

5.18 Contours of vorticity at 25 s from the oscillating inlet velocity scenario. 95

5.19 Turbulent intensity (%) from steady state CFD simulation on a single bunker (a), two bunkers spaced 5 m (b), and two bunker spaced 25 m (c). 96

5.20 The dimensionless y–displacement ($\frac{\xi_y}{H}$) at the center of the left side wall in a case with a single bunker (——) and a case with 5 m spaced two bunkers (- - -) in which the left wall of the second bunker downstream was the target versus time (s). 96

5.21 Illustration on the number of loops constructed on the top left side of the bunker surface. 98

5.22 Results of a dynamic wall case at 0.2 s in 10 s simulation that mimics a tarpaulin billowing with $n = 4$ loops, $f = 1$Hz, $A = 0.15$m, and $\Delta t = 0.1$ s. 99

5.23 Zones and boundary conditions set for internal flow simulations of the bunker. 100

5.24 The computational domain with dimensions used for the internal flow simulations of bunkers. Line G (- - -) was used for the grid test. 100

5.25 Hexahedral mesh generated for the internal flow simulations of bunkers with zooming in at the top center. 101

5.26 PH_3 concentration (ppm) along line G (Figure 5.24) at 24 h with three different mesh sizes (coarse - - -, medium ·-·-·, fine ——). 101

5.27 PH_3 contours (ppm) at 24 h showing the effect of headspace on PH_3 distribution; (a) no headspace and (b) with headspace. 103

5.28 PH_3 contours (ppm) at 24 h of a 3D slice of the bunker with neither leakage nor tarpaulin movement. 103

5.29 PH_3 contours (ppm) at 24 h for three different leakage rates; 0.0005 (a), 0.001 (b), and 0.005 $kg\,s^{-1}$ (c). . . . 104
5.30 PH_3 contours (ppm) at 24 h and tarpaulin moving continuously with 0.1 Hz, 5 cm amplitude, 10 loops (a), and 1 loop (b). . . . 105
5.31 The DNN structure with a flowchart of the main steps of the algorithm. . . . 107
5.32 The mean squared error of both the training (- - -) and validation (—) data at each epoch. . . . 108
5.33 The mean absolute error of both the training (- - -) and validation (—) data at each epoch. . . . 108
5.34 Comparison between the DNN model prediction and the CFD results of the mortality fraction (η) on the testing dataset. . . . 109
5.35 PH_3 contours (ppm) at two different number of loops; $n = 1$ (a – e) and $n = 10$ (b – f). (a, b) only the right wall moves, (c, d) only the left wall moves, and (e, f) both walls move. . . . 110
5.36 PH_3 contours (ppm) at two different amplitudes; (a) $A = 0.01$ m and (b) $A = 0.05$ m, with the same number of loops ($n = 1$) and both walls moving. . . . 110

A.1 Porosity contours along with its linear function (a), the viscous (b, c) and inertial (d, e) resistances to airflow of an inhomogeneous porosity. (c, d) are the contour lines. . . . 130
A.2 Contours of velocity (a) and pressure (b) of the bin of corn simulation. . . . 131
A.3 Magnitude of velocity ($m\,s^{-1}$) along the non-demonopolized radius of the bin resulted from the CFD simulation (—) compared to the experimental data of Bartosik and Maier (2006) (●). . . . 132
A.4 Pressure drop (Pa) vs velocity ($m\,s^{-1}$) using coefficients of Molenda et al. (2005a) for corn at three different porosities; minimum ($\varepsilon = 0.34$ —), average ($\varepsilon = 0.365$ - - -), and maximum ($\varepsilon = 0.365$ —). . . . 132

List of Tables

3.1 Values for coefficient of irreversible binding (K_{bind}) at different temperatures (T). 42

3.2 A quantitative comparison between results obtained from this study and work of Turek and Hron (2006). 45

4.1 Comparison of $\overline{Nu}$ with previous publications at two different (Ra_m = 100 and Ra_m = 1000), with Da = 10^{-7} for laminar and steady state flow in a square domain filled with porous media. 49

4.2 Temperature boundary conditions for the effect of orientation scenarios. 61

4.3 Factors investigated by modeling studies. 64

5.1 A quantitative comparison between results obtained from this study and work of Turek and Hron (2006). 83

5.2 Frequencies of the displacements and forces reported in Turek and Hron (2006) compared to values obtained from this study. 84

5.3 The non-dimensionalized y–displacement ($\frac{\xi_y}{H}$) and its frequency (f) resulted from the three different time-step sizes (Δt = 0.08, 0.05, 0.01 s) at points ($p-$, $p0$, and $p+$) on the top left wall of the bunker. 91

5.4 The range and limitations of the mortality fraction DNN model. 107

Acknowledgments

There are many people I wish to thank in helping me completed my Ph.D. Firstly, I would like to express my gratitude to my advisors Dr. Mark Casada, Dr. Ronaldo Maghirang, and Dr. Mingjun Wei, who guided and encouraged me throughout my academic career. Without their endless support, this work would not have come to fruition.

Secondly, I am grateful to my committee members Dr. Thomas Phillips and Dr. Kaliramesh Siliveru for their time and help in reviewing this work.

Thirdly, I wish to thank Dr. Danial Brabec for his useful discussions and help with the experiments. I also wish to thank Dr. Dennis Tilley and Rania Buenavista for their help with the experiments.

Fourthly, I'd like to thank Dr. Dirk Maier for his input and also Dr. Lester Pordesimo and Elizabeth Maghirang for their encouragement and support. I'd like to thank all my lab mates at the Computation Science for Fluids and Acoustics Lab in the Department of Mechanical and Nuclear Engineering and all my colleagues at USDA-ARS-CGAHR in Manhattan, KS.

Finally, I wish to thank my mother, my wife, and my children, all without whom I never would have pursued a Ph.D., my brothers, and my in-laws. Your love and support encouraged me to complete my academic journey.

Dedication

To my family and friends.

Chapter 1

Introduction

Wheat or other grain bulks, in general, construct a porous structure with interconnected pores (Bakker-Arkema et al., 1969). Gas flow exhibits pressure loss and an increase in velocity through the void paths. A relationship between the velocity and the pressure loss caused by the porous medium is needed to describe the flow. In Computational Fluid Dynamics (CFD), a grain bulk is modeled as a porous medium (Casada and Young, 1994a,b; Isa et al., 2016; Nguyen, 1985; Thorpe, 2008). Chapter 2 discusses the available theoretical and empirical correlations, in literature, between the pressure gradient and velocity. Chapter 2 also extracts coefficients that can reasonably mimic the presence of wheat in a CFD model. A new technique that estimates the resistance coefficients of wheat to gas flow without experimental work was introduced. The governing equations used in the CFD models of this study were also discussed.

Fumigation is a process used to chemically kill harmful insects in a grain storage facility. To be effective, the chemical, or fumigant, must fill the entire volume of the facility with a lethal dosage. Phosphine gas (PH_3) is widely used as a fumigant for grain protection against all life stages of insects (Chaudhry, 2000) due to its relatively low price and minimal residue left on the grain (Hackenberg, 1972). Phosphine gas is available in either gas (Cavasin et al., 2006) or solid formulations (Proudfoot, 2009). The solid formulation produces phosphine gas when the material comes into contact with the moisture in the air and is available in three

forms; aluminum, magnesium, and zinc phosphides (Waterford et al., 1994). Aluminum phosphide (AlP) is the most commonly used solid formulation for producing PH_3 due to its effectiveness (Hackenberg, 1972). The AlP decomposition rate is not constant with time and depends on temperature and relative humidity (Tan, 1994).

A PH_3 dosage of 200 to 300 parts per million by volume (ppmv) for an exposure period of 5 to 7 days (Wrigley et al., 2015) is a recommended treatment target for killing insects in grain facilities. The fumigation process will be less effective or may even fail to control insects significantly if a proper dosage is not achieved throughout the grain facility. The PH_3 concentration varies within a treated grain facility, more so for larger facilities, which means that some locations may have a lethal concentration while other locations do not. To track the desired PH_3 concentration in the entire grain facility volume, an adequate number of sensors should be installed at different locations, which is costly.

CFD, which involves solving the governing equations of fluid flow, coupled with adequate validation with either or both of the published benchmarks and experimental data, can be used to understand the behavior of PH_3 in an enclosed area based on predefined boundary conditions. For the gas form of PH_3, which is applied using compressed gas cylinders, implementing the boundary conditions is a relatively simple process because the controlled gas release rate is known. For solid formulations, such as AlP tablets or pellets, the variable evolution rate of PH_3 must be known for accurate results.

Few studies have examined modeling the evolution of PH_3 from AlP tablets. Annis and Banks (1993) used a simplified model. Isa et al. (2016) developed a mathematical formula that accounts for the evolution rate of the PH_3 based on experimental data from Tan (1994). Tan's experiment was conducted with an assembled apparatus to pass controlled air with a constant temperature ($\pm 0.5\,^{\circ}C$) and constant humidity ($\pm 5\%$) into a chamber containing ten AlP tablets. The tablets started to decompose when exposed to the air. The evolved PH_3 was then collected with an automatic gas sampler, and the concentration was determined using colorimetric analysis. However, the formula developed by Isa et al. is valid only at a temperature of $25\,^{\circ}C$ and a fixed relative humidity that is not mentioned explicitly in their work. In Chapter 3, a mathematical relationship on the releasing rate from AlP formulation

as a function of both temperature and relative humidity was developed based on published experimental data of Tan (1994).

Grain bunkers are large grain piles, usually constrained by a retaining wall at the base, and covered with a tarpaulin. Bunker fumigation methods use diffusion and various convection currents, including the internal flows driven by movement of the covering tarpaulin due to external flow over the bunker, to distribute the gas. When those processes do not transport gas to every point in the treated space, the resulting low dosage causes failure of the treatment and survival of some targeted insects. The survival of insects potentially selects for resistance to phosphine, a growing problem that could render phosphine ineffective for stored product insect control (e.g., Afful et al., 2018; Collins et al., 2001). Experiments fail to provide detailed information on the motion mechanisms of fumigant PH_3 inside grain bunkers. CFD simulations, on the other hand, can reasonably predict the PH_3 behavior affected by surrounding variables such as different weather conditions, leakage, or sorption by grain.

The bunkers are exposed to the weather, and the fluid occupying the void volume of this constructed porous medium is highly affected by convection currents. Natural convection occurs because of the density gradient caused by temperature variations inside bunkers. The density of PH_3 is very close to the density of air (specific gravity = 1.15), i.e., PH_3 is carried by the air and follows the motion patterns of the air. A sufficient concentration of PH_3 must be achieved for sufficient time to kill insects in grain. Although fluid velocity induced by natural convection is very low, it helps move PH_3 from high concentration areas to low or zero concentration areas. Natural convection in enclosures filled with the porous medium, in general, have been established and well defined (Baytas and Pop, 1999; Bejan, 1979; Gross et al., 1986; Lauriat and Prasad, 1989).

CFD was used to study both heat and mass transfer in grain beds and results obtained were well validated (Casada and Young, 1994a,b; Nguyen, 1987; Singh and Thorpe, 1993). Nguyen (1985) studied the fumigant motion induced by natural convection in 2D square-shaped storage facilities and triangular-shaped bunkers. His results were physically reasonable, but the model did not include the species (fumigant) equation nor the other factors that

disturb the fumigant motion such as location(s) of fumigant release points, leakage of the tarpaulin, or sorption by the commodity. Those factors are unavoidable and highly impact the PH_3 distribution in bunkers.

Other studies were done with focuses on PH_3 transport in wheat (Agrafioti et al., 2020; Isa et al., 2016). Agrafioti et al., used field experiments on a grain silo. In contrast, no comparison to theoretical or experimental data were done to validate the work of Isa et al. instead, two different CFD software were used as a model accuracy test. In addition, Isa et al.'s model was under the assumption of uniform and constant temperatures as their computational domains were relatively small. Although Agrafioti et al. considered both convection and solar radiation effects, that model did not consider the spatial variation of those effects. In Chapter 4 CFD was used to examine different physical configurations and important factors for PH_3 fumigation of bunkers. The CFD model was validated with published benchmarks on natural convection in porous media and experimental data from a full-scale grain bin subject to natural convection, leakage, and PH_3 sorption into wheat.

PH_3 moves slowly through the porous space in the grain mass due to diffusion and when carried by natural convection air currents, and it leaves the pore space when absorbed by the grain or when leaking from the storage container. An additional and unique free source that may enhance the PH_3 distribution, at a much faster rate than diffusion and natural convection combined, is available for those grain storage facilities with plastic covers i.e., bunkers. When wind hits bunker surfaces, it causes the tarpaulin to billow which in turn forces the PH_3 to move from areas near the surface to other locations within the bunker.

Understanding the motion mechanism of PH_3 caused by tarpaulin movements requires obtaining information on these movements. Fluid-Structure Interaction (FSI) simulation, as the name suggests, can describe the interaction of a solid structure (e.g., tarpaulin) and fluid (e.g., air + PH_3) subject to different wind conditions. The plastic cover of a bunker is a very thin flexible material. FSI technique was applied on a membrane and tent structures (e.g., Cuomo and Lanza, 2019; Glück et al., 2001; Knight et al., 2010; Wüchner et al., 2007).

In grain storage, one attempt at the effect of tarpaulin billowing on the PH_3 behavior was given on Australian bunkers (He, 2016) with unrealistic assumptions and was difficult

to conclude. In this attempt, many external CFD analyses on different bunker shapes and configuration were conducted with a few FSI simulations. In the FSI scenarios, highly unrealistic thickness of the tarpaulin, solid-to-fluid density ratio, bunker dimensions, and material properties were adopted. While turbulent flow was assumed for the external flow study, laminar flow was the input for the FSI cases. As a result of these choices, it was concluded that the deformation of the tarpaulin occurred only in one direction with no oscillation. Finally, an internal flow CFD model was built for the fumigant behavior with unrealistic boundary conditions e.g., oscillating inlet pressure on the entire surface of the bunker with PH_3 as the outside surrounding fluid and unjustified pressure amplitude (He, 2016). Thus, no study whatsoever has reasonably described the effect of tarpaulin billowing on PH_3 and its contribution to the fumigant distribution.

In Chapter 5, FSI simulations were used to describe the tarpaulin movements under different wind conditions. The FSI model was validated against published benchmarks (Glück et al., 2001; Turek and Hron, 2006). This motion was then simplified and defined mathematically. The mathematical equation was used as a non-linear boundary condition in a CFD model to capture the response of PH_3 to different motion parameters. Results from the CFD were used as an input to a deep learning neural network (DNN) to predict and correlate the fumigation effectiveness to the motion parameters without further CFD modeling.

The main objectives of this study were to: (1) Develop and evaluate CFD models to predict phosphine gas transfer in grain storage bunkers and (2) Deliver recommendations for best management practices for phosphine fumigation in bunkers to minimize the phosphine loss and reduce insect resistance to phosphine. This dissertation includes contents of self-publication: published [1] (Chapter 3; ASABE has granted permission to include this item.), submitted for publication [2] (Chapter 4), and in preparation [3] (Chapter 5).

[1]Elsayed, Sherif, Casada, Mark E., Maghirang, Ronaldo G., & Wei, Mingjun. (2021). Evolution of phosphine from aluminum phosphide pellets. Transactions of the ASABE, 64(2):615–624.

[2]Elsayed, Sherif, Casada, Mark E., Maghirang, Ronaldo G., Wei, Mingjun, & Maier, Dirk E. (2022). Numerical simulation of phosphine movement in bulk-stored grain. Manuscript submitted for publication.

[3]Elsayed, Sherif, Casada, Mark E., Maghirang, Ronaldo G., Wei, Mingjun, & Maier, Dirk E. (2022). Effect of tarpaulin billowing on phosphine movement in bunkers – numerical simulations. Manuscript in preparation.

Chapter 2

Numerical Description

2.1 Objective

This chapter (1) Discusses the published theoretical and empirical correlations between the pressure gradient and velocity induced by the presence of wheat as a porous medium, (2) Chooses the reasonable resistance coefficients of wheat to gas flow and tests them numerically, (3) Provides the full set of customized governing equations used for the simulations in Chapters 3, 4, and 5, and (4) Introduces a new technique using CFD that can replace experimental work for estimating the resistance coefficients.

2.2 Wheat resistance to gas flow - a literature review

Wheat or grain bulks, in general, construct a porous structure with interconnected pores. Fluid flow exhibits pressure loss and an increase in velocity through the void paths. A relationship between the velocity and the pressure loss caused by the porous medium is needed to describe the flow. In CFD, a grain bulk is modeled as a porous medium. This section aims to find the appropriate coefficients that describe the resistance of wheat bulks to gas flow. This is important to understand the fumigant distribution in a grain storage facility.

For a steady state, incompressible fluid, and constant porosity, the conservation of mass still holds true and can be described as

$$\nabla \cdot \vec{v} = 0 \tag{2.1}$$

where v is the superficial velocity which is the velocity the fluid would have in the absence of the porous medium. It has many different names: Darcy velocity, average velocity, superficial velocity, filtration velocity, and seepage velocity (Nield and Bejan, 2017), face velocity (Hood and Thorpe, 1992), or empty-tower velocity (McCabe et al., 1993). It is the mean velocity – flow rate divided by the cross-sectional area, $\frac{1}{A_c}\iint v\ dA_c$. The physical, the true, or the interstitial velocity, is the fluid velocity around the grain kernels. Both velocities are related as $v_{superficial} = \varepsilon\ v_{physical}$, in which ε is the porosity or the void fraction.

The relationship between the drop in pressure and velocity has been investigated for decades, either experimentally or semi-theoretical. Shedd (1953), experimentally studied the pressure drop in grain beds. He fitted the obtained results of different grains to an equation of this form

$$\frac{\nabla p}{L} = -a_o\ v^{b_o} \tag{2.2}$$

where, ∇p is the pressure drop (Pa), L is the thickness of the grain bulk, and a_o and b_o are empirical constants that depend on the grain type. Hukill and Ives (1955) came up with another correlation as

$$\frac{\nabla p}{L} = \frac{a_1\ v^2}{\ln(1 + b_1\ v)} \tag{2.3}$$

In Eq. 2.3, a_1 and b_1 are also empirical constants that vary with the type of grain. These two equations, Eqs. 2.2 and 2.3, have been widely used to estimate the pressure drop across a bulk of grain. While Hukill and Ives's equation has the nonlinear term of velocity which makes it more accurate, Shedd's equation may give better results. For instance, Kumar and Muir (1986) found that Shedd's equation, Eq. 2.2, was best fit to his data with less error than Hukill and Ives's equation, Eq. 2.3. Attempts were made to generalize both Eq. 2.2 and Eq. 2.3 (e.g., Jayas and Sokhansanj, 1989). In CFD modeling, these equations have some

drawbacks, for example, they do not provide any information on the fluid or the porous medium properties (Hood and Thorpe, 1992; Li and Sokhansanj, 1994) and the velocity in Eq. 2.3 is difficult to be defined explicitly in terms of the pressure drop which make it complicated to implement mathematically (Hood and Thorpe, 1992).

Darcy (1856) through his experiments on a steady state flow, unidirectional, and uniform porous medium, found out that the velocity is linearly related to the gradient of the pressure. The coefficient of the proportionality carries out information from both the fluid through the dynamic viscosity, μ ($\mathrm{kg\,m^{-1}\,s^{-1}}$), and the porous medium through the permeability, K ($\mathrm{m^2}$). The permeability describes the ease of a fluid to flow through a porous medium. In a generalized vector form Darcy's equation can be expressed as

$$\nabla p = -\frac{\mu}{K}\,\vec{v} = -R\,\vec{v} \tag{2.4}$$

where ∇p is the pressure gradient ($\mathrm{Pa\,m^{-1}}$) and $R = \dfrac{\mu}{K}$ ($\mathrm{Pa\,m^{-2}\,s^{-1}}$) is the resistance to fluid flow. The negative sign describes that the pressure decreases in the direction of the flow. Darcy's equation, Eq. 2.4, has been utilized successfully in the momentum equation to describe the heat and mass transfer in a grain bulk (Casada and Young, 1994b; Nguyen, 1987). It is valid if the particle Reynolds number, $Re_p = \dfrac{\rho\,|\vec{v}|\,d_p}{(1-\varepsilon)\mu}$, in which ρ ($\mathrm{kg\,m^{-3}}$) is the fluid density and d_P (m) is the particle diameter, is less than unity (Nield and Bejan, 2017). It may even be valid for $Re_p < 10$ (Prasad and Kladias, 1991). In other words, it is valid when the relationship between the pressure gradient and velocity is linear where the viscous forces are dominant. At $Re_p > 1$, inertial forces may grow near the boundary of the pores.

2.2.1 Ergun Equation

Forchheimer (1901) developed a formula that considers both the viscous and inertial effects and can be expressed in a generalized vector form as

$$\nabla p = -\left(R\,\vec{v} + S\,|\vec{v}|\vec{v}\right) \tag{2.5}$$

Eq. 2.5 was the basis for Ergun's (1952) equation which is widely used in many fields. This equation considers the effect of both viscous and inertial forces caused by the porous medium. It does not, however, consider the no-slip conditions at the boundaries i.e., the boundary effects are ignored. To account for the viscous effects at the walls, the Brinkman term was added initially to Darcy's equation (Nield and Bejan, 2017). It is a second order partial differential term, $\mu\nabla^2\vec{v}$. The transient, body force, or external source terms could be easily added to construct a full momentum equation. The argument is on the contribution of adding a convective term, $(\vec{v}\cdot\nabla)\vec{v}$ (Lage, 1992).

Ergun's equation which expanded the viscous resistance coefficient, R ($\mathrm{Pa\,m^{-2}\,s^{-1}}$), and the inertial resistance coefficient, S ($\mathrm{Pa\,s^2\,m^{-3}}$), is

$$\nabla p = -\left(150\frac{(1-\varepsilon)^2}{\varepsilon^3\ d_p^2}\mu\ \vec{v} + 1.75\frac{(1-\varepsilon)}{\varepsilon^3\ d_p}\rho\ |\vec{v}|\vec{v}\right) \tag{2.6}$$

Ergun's equation is very sensitive to the value of the porosity (ε) (McCabe et al., 1993) as a small change in this value may result in a significant change in the pressure gradient. Comparing Eq. 2.4 (Darcy) and Eq. 2.6 (Ergun), the permeability can be calculated as

$$K = \frac{\varepsilon^3\ d_p^2}{150(1-\varepsilon)^2} \tag{2.7}$$

In some references (e.g., Thorpe, 2002), the 150 in Eq. 2.7 is replaced by 180 and it was shown to be a reasonable representation for the permeability of wheat. The 180 is coming from Carman and Kozeny's correlation (Carman, 1937; Kozeny, 1927). Ergun's equation with modified constants can describe applications involving grains (Bakker-Arkema et al., 1969; Giner and Denisienia, 1996; Kay et al., 1989; Li and Sokhansanj, 1994; Molenda et al., 2005a; Patterson et al., 1971; Yang and Williams, 1990).

Bakker-Arkema et al. (1969), for example, on his study on cherry pits found that multiplying Ergun's equation, Eq. 2.6, by a single constant, can describe the pressure drop caused by that grain. Yang and Williams (1990) on sorghum, found that the weight for each term in Ergun's equation, laminar and turbulent, is different so, two different constants for each

term are needed to describe the pressure drop. Li and Sokhansanj (1994) came to the same conclusion of Yang and Williams using a different approach. Molenda et al. (2005a) followed Li and Sokhansanj's method by utilizing Ergun's equation to fit his experimental data of different types of grains. Rearranging the equation in Molenda et al.'s work to match with Ergun's, it takes the form

$$\nabla p = -\left(a_2 \frac{(1-\varepsilon)^2}{\varepsilon^3 \; d_p^2} \mu \; \vec{v} + b_2 \frac{(1-\varepsilon)}{\varepsilon^3 \; d_p} \rho \; |\vec{v}|\vec{v}\right) \tag{2.8}$$

where a_2 and b_2 are 397 and 3.256, respectively, for white wheat or 247.8 and 4.352 for red wheat instead of 150 and 1.75 in Eq. 2.6. Li and Sokhansanj, whose approach was followed by Molenda et al., found higher values of 475.2 and 4.594, respectively, for wheat. The pressure drop results from Li and Sokhansanj match with the results of Hood and Thorpe (1992). Yang and Williams on their study on grain sorghum found values of 358.35 and 2.82 for a_2 and b_2, respectively. However, it might not be accurate comparing those values to the original constants of Ergun. If one is to drive Ergun's 1952 equation, at some point it includes the tortuosity factor and sphericity. Substituting these values of wheat, for example, the resulted constants would be very comparable to values found empirically by either Molenda et al. (2005a) or Li and Sokhansanj (1994). Ergun's equation in terms of the tortuosity factor and sphericity might be expressed as (McCabe et al., 1993, pp.153–154)

$$\nabla p = -\left(72 \frac{\tau}{\theta^2} \frac{(1-\varepsilon)^2}{\varepsilon^3 \; d_p^2} \mu \; \vec{v} + 1.75 \frac{1}{\theta} \frac{(1-\varepsilon)}{\varepsilon^3 \; d_p} \rho \; |\vec{v}|\vec{v}\right) \tag{2.9}$$

where τ is the tortuosity factor and θ is the sphericity. In Ergun's equation, Eq. 2.6, these values are 2.1 and 1 (spheres), respectively. For wheat, $\tau = 2.4$ (Neethirajan et al., 2008) and $\theta = 0.6$ (Kheiralipour et al., 2008). That gives the constants a_2 and b_2 of 480 and 2.9, respectively. Figure 2.1 compares between the results of Eq. 2.9 to published experimental work (Hood and Thorpe, 1992; Li and Sokhansanj, 1994; Molenda et al., 2005a). As seen, Eq. 2.9 can describe the pressure loss across bulks of grain when included both τ and θ.

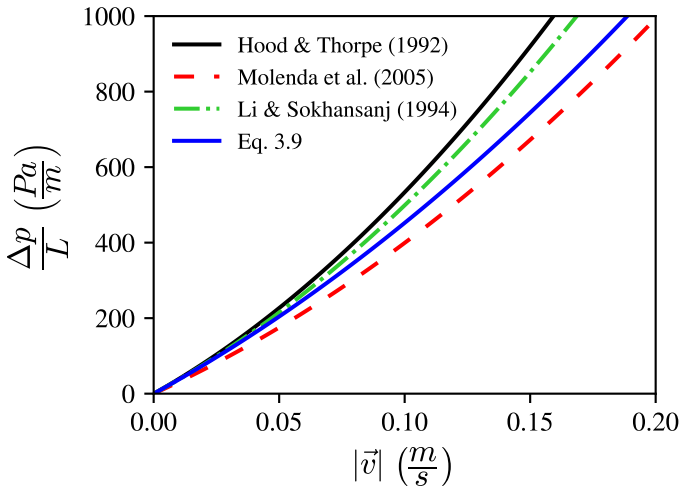

Figure 2.1: Pressure drop per unit length ($\mathrm{Pa\,m^{-1}}$) vs air velocity ($\mathrm{m\,s^{-1}}$); a comparison between Eq. 2.9 (——) and published data of Hood and Thorpe (1992) (——), Molenda et al. (2005a) (- - -), and Li and Sokhansanj (1994) (-·-·-).

Comparing the results of Molenda et al. (2005a), in Eq. 2.8, for white wheat with $\varepsilon = 0.4$ and $d_p = 0.0037$m (Funnel filling method and 12.7% moisture content) to the data of Shedd (1953) and Hukill and Ives (1955), both were reported in Hunter (1983), they are almost identical. Figure 2.2 shows this comparison in addition to results from Ergun's equation, without any modifications and with the same ε and d_p. This shows the applicability of both formulas of Shedd and Hukill and Ives.

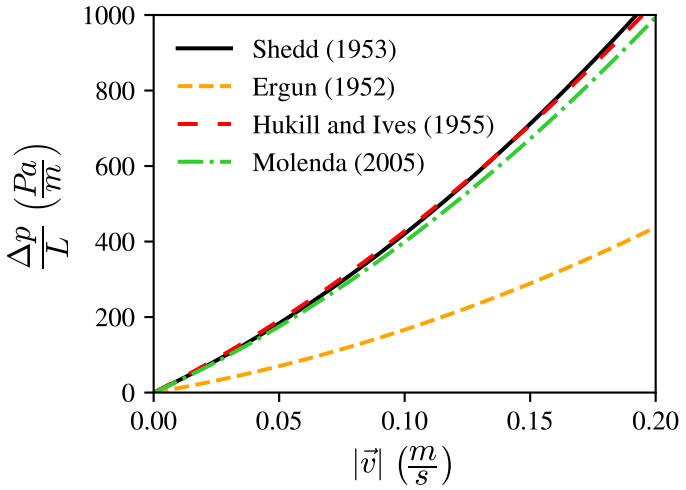

Figure 2.2: Pressure drop per unit length ($\mathrm{Pa\,m^{-1}}$) vs air velocity ($\mathrm{m\,s^{-1}}$) at 12.7% moisture content with funnel filling method (Molenda et al., 2005a) (-·-·-) in comparison with results of Shedd (1953) (——), Ergun (1952) (- - -), and Hukill and Ives (1955) (- - -).

2.2.2 Factors affecting the resistance to airflow

There are many factors that affect the resistance to fluid flow in a grain bulk which in turn affects the resulted pressure drop. These factors could be listed as: the filling method, bulk density, porosity, tortuosity, moisture content, depth of the grain bulk, kernel orientation, size and shape of the kernel, surface roughness of the grain kernel, size and distribution of the foreign material, direction of the flow, velocity, and viscosity of fluid. In modelling applications that involves grain bulk, the variation in the fluid properties on the pressure drop could be ignored. As a result, the variability of the fluid parameters could be excluded, as the contribution of their change to the pressure drop is insignificant.

The contribution of most of those factors end up as a change in one parameter which is the porosity. In turn, it affects the pressure drop across the grain bulk. This is clear from Ergun's (1952), Eq. 2.6. In this equation, the media properties are the equivalent particle diameter and porosity. The pressure drop is more sensitive to the porosity than the particle diameter. Analyzing Ergun's equation, a 10% change in the particle diameter results in a pressure drop that is equivalent to a 4% change in the porosity at the initial particle diameter. Nevertheless, a change in the volume equivalent particle diameter affects the porosity itself, as well. The contribution of those factors on the porosity and the pressure losses, as a result, vary. Results from different publications might be different slightly or vastly because it is impossible to reproduce an experiment that involves a bulk of grain with all those factors and get the exact same results; unless all parameters can be controlled and the focus is on a single parameter at a time, which might not be practical.

2.2.2.1 Moisture content

When moisture content increases, bulk density decreases, and porosity increases. This results in a decrease in the airflow resistance. In wheat with moisture contents ranging between 10.2% and 15%, no significant change was observed on the pressure drop (Molenda et al., 2005b). The same author, Molenda et al. (2005a), observed up to a 43% increase in the pressure drop (at $0.2\,\mathrm{m\,s^{-1}}$ velocity) when increasing the moisture content from 10.5% to

12.7%. A change in the resistance of less than 20% for a moisture content ranging between 10.5% to 14.6% was observed by Montross and McNeill (2005). Haque et al. (1982) fitted his experimental data of corn, sorghum, and wheat, and came up with a correlation for the pressure drop and moisture content, rearranging his equation and putting it in a vector form so, it is suitable for modelling, it can be expressed as

$$\nabla p = -\left[\left(a_3 - c\ M\right)\vec{v} + b_3\ |\vec{v}|\vec{v}\right] \tag{2.10}$$

where a_3, b_3, and c are grain constants, and M is the moisture content ($\%wb$). So, the resistance is $R = a_3 - cM$. For wheat, $a_3 = 5573.9$, $b_3 = 9634.6$, and $c = 200.3$. It is noticed that the coefficient of the linear term at 12.7% moisture content is $R = 3030\,\mathrm{Pa\,s\,m^{-2}}$, which is very close to resistance from Molenda et al. (2005a) of white wheat and at the same moisture content, $R = 3016\,\mathrm{Pa\,s\,m^{-2}}$. Applying this correlation on wheat, an increase in the moisture content from 10.5% to 12.7% results in an 8% decrease in the pressure drop at $0.2\,\mathrm{m\,s^{-1}}$. This is not far from Giner and Denisienia (1996) who concluded that an increase of moisture content of wheat ranging from 12.8% to 22.3% resulted in a decrease in the pressure drop by 12% to 22%.

2.2.2.2 Filling method

Filling method by far has the most significant effect on the pressure drop in a fixed bed of grain (Chang et al., 1983; Jayas et al., 1987; Kumar and Muir, 1986; Molenda et al., 2005a; Stephens and Foster, 1978). The two common filling methods are the funnel (spout) and the sprinkle (grain spreader). The funnel method provides low bulk density while the sprinkle method provides high bulk density. High bulk density decreases the bulk porosity, hence higher airflow resistance.

Wheat with the spreader filling method results in an increase in the resistance by 25% to 75% more than the spout method (Kumar and Muir, 1986), depending on the airflow direction. This percentage can go to a 100% increase in the pressure drop (Chang et al., 1983; Molenda et al., 2005a; Stephens and Foster, 1978). Jayas et al. (1987) studied the

effect of the filling method on rapeseed also concluded that airflow resistance is doubled when using a sprinkle fill. Montross and McNeill (2005), reported a 25% increase but their study was at low airflow velocities, so this percentage is expected to be higher at higher air velocities. While the kernel orientation is affected by the filling method, it did not show any significance on the pressure drop according to Molenda et al. (2005a) but it shows up to 60% based on work done by Kumar and Muir (1986).

2.2.2.3 Foreign material

Another important factor on the airflow resistance is the presence of a foreign material (Stephens and Foster, 1978). A 10% to 20% increase in the pressure drop due to dockage was observed by Kumar and Muir (1986). This percentage can vary based on the amount of material. This material can fill in between the grain kernel and change the bulk porosity. This change in bulk density causes the resistance to be position dependent. The distribution of the fine content was found to be the same in bins regardless of the filling method (Chang et al., 1983) – the porosity has a low value in the center of the storage facility and increases gradually towards the walls. This was supported by Lawrence and Maier (2011) by implementing a linear variation of porosity along the horizontal axes (small porosity in the middle that increase linearly to the wall) in CFD simulations. Haque (2011) studied analytically the vertical variation of porosity. He concluded that the porosity has higher value at the top and lower value at the bottom. Those spatial dependencies, either horizontally, vertically, or both, cause the airflow resistance to vary with position (inhomogeneous porous medium).

2.2.2.4 Direction of the flow

When the resistance to airflow depends on the direction that means it is anisotropic, otherwise it is isotropic. If this resistance is a spatial dependent that means it is heterogenous (inhomogeneous), otherwise it is homogenous. So, the resistance to airflow could be anisotropic and homogenous, anisotropic and heterogenous, isotropic and homogenous, or isotropic and heterogenous. Individual grain will naturally align horizontally on their longer side due to

gravity (Hood and Thorpe, 1992). So, the resistance to airflow will behave differently based on the airflow direction. In the case of anisotropic, the resistance to airflow is a second-rank tensor, $[3 \times 3]$ matrix.

Resistance to airflow in the bulk of grain used to be assumed isotropic (Hood and Thorpe, 1992). The isotropic assumption is not necessarily wrong because it depends on the type of the grain, its shape, and the geometry of the storage facility. A few publications have studied the effect of airflow direction on the resistance. It was pointed out that the resistance to airflow from the vertical direction is different from the one in the horizontal direction (ASABE Standards, 2016; Hood and Thorpe, 1992; Jayas and Muir, 1991; Kay et al., 1989; Khatchatourian et al., 2009; Kumar and Muir, 1986; Łukaszuk et al., 2008; Neethirajan et al., 2006). In this case the resistance is orthotropic. Applying this to Darcy's equation, Eq. 2.4, in a matrix form

$$\begin{pmatrix} u \\ v \\ w \end{pmatrix} = -\frac{1}{\mu} \begin{pmatrix} K_{xx} & 0 & 0 \\ 0 & K_{yy} & 0 \\ 0 & 0 & K_{zz} \end{pmatrix} \begin{pmatrix} \frac{\partial p}{\partial x} \\ \frac{\partial p}{\partial y} \\ \frac{\partial p}{\partial z} \end{pmatrix} \tag{2.11}$$

where u, v, w are the velocity components in x, y, z, respectively. Since the permeability does not change between the two axial directions, x and y, i.e., $K_{xx} = K_{yy}$, the resistance is said to be transversely orthotropic (Hood and Thorpe, 1992).

For wheat, the resistance to vertical airflow is 20% – 60% higher than the horizontal resistance while it is 65% – 115% for barley according to Kumar and Muir (1986). The vertical resistance is 72% – 122% greater than the one in the horizontal direction for shelled corn (Kay et al., 1989). Hood and Thorpe (1992) studied the anisotropic effect on ten different types of grain bulks. For wheat, the coefficient of the viscous term, R in Eq. 2.5, in the vertical direction is 11% greater than the one in the horizontal direction. While for the coefficient of the inertial term, S in Eq. 2.5, is 46% greater than the horizontal resistance. For grain that is almost spherical, the resistance was almost isotropic. Neethirajan et al. (2006) used X-ray images to capture the airpaths in each direction on six types of grains.

For wheat, the air paths in the horizontal direction was found to be 100% more than air paths in the vertical direction, which shows that the resistance in the vertical direction is much higher than the horizontal resistance. Łukaszuk et al. (2008) found that the resistance is different even between the two horizontal axes but still higher in the vertical direction: $R_{zz} = 1.3R_{xx} = 1.95R_{yy}$. Khatchatourian et al. (2009) from his experimental and numerical study, found that the anisotropy ratio, $\left(\frac{K_{xx}}{K_{yy}}\right)$, is related to the airflow velocity. According to ASABE Standards (2016), the resistance in the horizontal direction is 60% – 70% of the one in the vertical direction. On the contrary, Montross and McNeill (2005) through their experiments on wheat, did not observe any significant variations in the resistance between the two directions. It was concluded that the filling ratio and kernel orientation significantly affect the variation between the horizontal and vertical resistance. Figure A.1 in Appendix A.1, shows an anisotropic resistance with inhomogeneous porosity that varies linearly applied on a 2D bunker shape.

In this study, wheat is the primary grain with no variability in the moisture content. Hood and Thorpe's (1992) resistance coefficients as an anisotropic model were considered. Comparing Hood and Thorpe's coefficients of vertical flow to the results of Molenda et al. (2005a), Figure 2.3, of white wheat with $\varepsilon = 0.35$ and $\varepsilon = 0.4$, as the minimum and maximum measured values resulted from two different filling methods, and $d_p = 0.037$m at 12.7% moisture content. It is clear that Hood and Thorpe's coefficients serves as a medium base between the two extremes. For the flow in the horizontal direction, ASABE Standards (2016) recommends that the pressure drop in the horizontal direction be 60% – 70% of the one in the vertical direction. This percentage is applied to both terms, viscous and inertial, equally. While Hood and Thorpe's coefficients has more physics into it by applying different weights to each term; $R_H \approx 0.9R_V$ and $S_H \approx 0.68S_V$. The inertial term is satisfied with the ASABE Standards recommendation, while the viscous term of Hood and Thorpe provides more pressure drop. Nonetheless, the assumption of $R_H \approx 0.9R_V$ is still of the range observed by (Kay et al., 1989; Kumar and Muir, 1986), although it was on a different grain. Hood and Thorpe's coefficients provide pressure drop higher than results of Shedd (1953) and, Hukill and Ives (1955) but almost identical to results of Li and Sokhansanj (1994). The permeability of

the bulk of wheat ranging K =7.29×10^{-9}m^2 to 1.15×10^{-8}m^2 (Montross and McNeill, 2005) compared to $K \approx 5 \times 10^{-9}$m^2 of Hood and Thorpe, which is slightly lower.

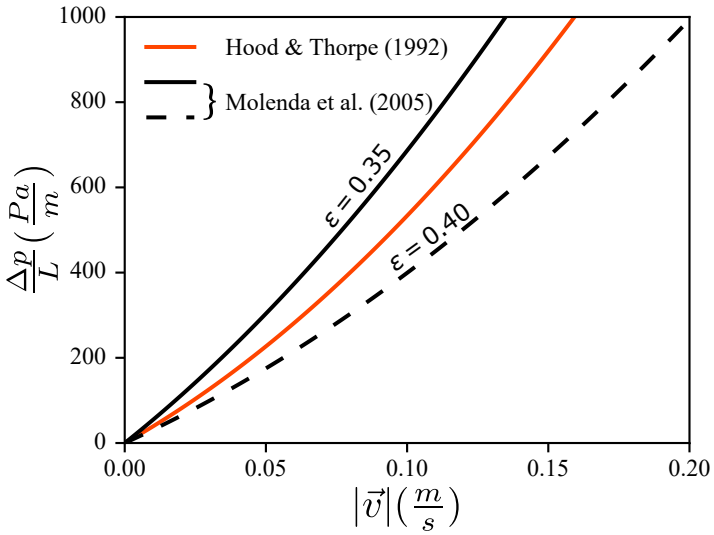

Figure 2.3: Pressure drop per unit length (Pa m^{-1}) vs air velocity (m s^{-1}) using resistances coefficients of Hood and Thorpe (1992) (—) and at the minimum (—) and maximum (- - -) porosity using constants of Molenda et al. (2005a).

2.2.3 Implementation test

A 2D, steady-state flow, isothermal, and incompressible fluid was implemented in a CFD model. This was built to ensure the accuracy of utilizing an anisotropic resistance. The model utilized Hood and Thorpe (1992) resistance coefficients for wheat with a constant porosity (ε = 0.4). Properties of air were taken at 20 °C. In this model, the airflow is horizontal and goes through a 0.5 m length non-porous region then a 0.25 m porous region followed by 1.0 m non-porous region. Seven different superficial velocities ranging from 0.025 m s^{-1} to 0.2 m s^{-1} were considered in this test case and the body force was assumed to be negligible. No-slip condition at the top and bottom walls were defined with pressure outlet at the exit. The domain size was chosen to prevent reverse flow. No grid refinement test was performed because the domain is relatively small and sufficient elements of structure cells were used. The problem was solved using the superficial velocity formulation in addition to the physical velocity formulation.

In this model ANSYS Fluent 2021R1 was used for solving the governing equations. The

resistance coefficients were added as a sink term in the momentum equations (x, y). The continuity, x–momentum, and y–momentum can be expressed as

$$\frac{\partial u}{\partial x} + \frac{\partial v}{\partial y} = 0 \tag{2.12}$$

$$\rho\left(u\frac{\partial u}{\partial x} + v\frac{\partial u}{\partial y}\right) = -\frac{\partial p}{\partial x} + \mu\left(\frac{\partial^2 u}{\partial x^2} + \frac{\partial^2 u}{\partial y^2}\right) - \left[D_{xx}\ \mu\ u + C_{xx}\frac{1}{2}\rho\ |\vec{v}|u\right] \tag{2.13}$$

$$\rho\left(u\frac{\partial v}{\partial x} + v\frac{\partial v}{\partial y}\right) = -\frac{\partial p}{\partial y} + \mu\left(\frac{\partial^2 v}{\partial x^2} + \frac{\partial^2 v}{\partial y^2}\right) - \left[D_{yy}\ \mu\ v + C_{yy}\frac{1}{2}\rho\ |\vec{v}|v\right] \tag{2.14}$$

where u and v are the superficial velocity ($\mathrm{m\,s^{-1}}$) components in x and y directions, p is the pressure (Pa), ρ is the air density ($\mathrm{kg\,m^{-3}}$), μ is the dynamic viscosity ($\mathrm{kg\,m^{-1}\,s^{-1}}$), $D_{xx} = \dfrac{R_{xx}}{\mu}$, $D_{yy} = \dfrac{R_{yy}}{\mu}$, $C_{xx} = 2\dfrac{S_{xx}}{\rho}$, and $C_{yy} = 2\dfrac{S_{yy}}{\rho}$. $R_{xx} = 3369\,\mathrm{Pa\,s\,m^{-2}}$, $R_{yy} = 3740\,\mathrm{Pa\,s\,m^{-2}}$, $S_{xx} = 10\,940\,\mathrm{Pa\,s^2\,m^{-3}}$, and $S_{yy} = 15\,940\,\mathrm{Pa\,s^2\,m^{-3}}$ (Hood and Thorpe, 1992). More information on the governing equations and their implementations are discussed in Section 2.3.

Figure 2.4 shows the contours of the superficial velocity (a), the physical velocity (b), and the pressure (c) at $0.05\,\mathrm{m\,s^{-1}}$ inlet velocity. As seen, the superficial velocity technique does not consider the presences of the porous medium in the velocity whatsoever while the true velocity does. However, it is a very accurate technique when the pressure drop caused by a bulk of grain is of the interest. The superficial formulation is the default method in most commercial CFD codes. In Figure 2.4(d), a comparison between the CFD output and results from Eq. 2.5 using Hood and Thorpe's coefficients were made. Results from the CFD matches exactly with the results from Eq. 2.5 which ensure the accuracy of the implementation. The circled region, in red, shows no deviation between the results with and without the inertial resistance. This confirms that the use of Darcy's (1856) equation (viscous resistance) is reasonable at low velocities. Appendix A.2 shows an additional test using the same CFD model applied on corn.

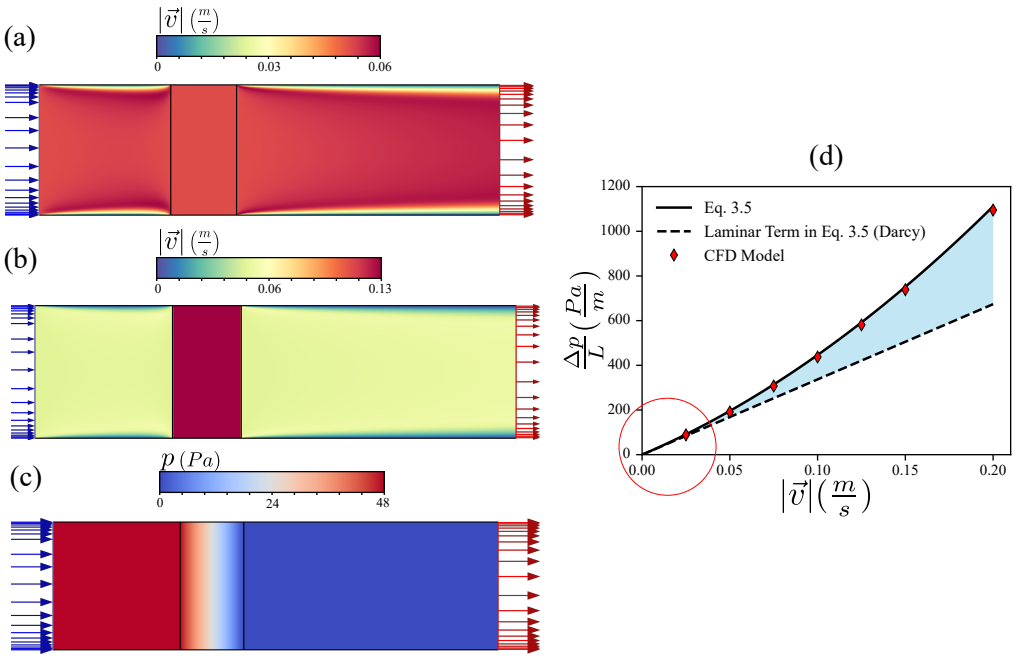

Figure 2.4: Contours of superficial velocity (a), true velocity (b), and pressure (c) along with a comparison (d) between the pressure drop per unit length ($\mathrm{Pa\,m^{-1}}$) vs velocity ($\mathrm{m\,s^{-1}}$) between the CFD results (◆), results of Eq. 2.5 (——) with Hood and Thorpe (1992) coefficients, and Darcy's (1856) model (- - -).

2.3 Governing equations

The main equations that govern the fluid flow in all the models are the continuity, momentum, species, and energy. The continuity equation takes the form

$$\frac{\partial(\varepsilon\rho_g)}{\partial t} + \nabla\cdot(\varepsilon\rho_g\vec{v}) = S \tag{2.15}$$

In Equation 2.15, ρ_g ($\mathrm{kg\,m^{-3}}$) is the density of the gas mixture (air + PH_3), ε is the porosity, and S[1] is the source term ($\mathrm{kg\,m^{-3}\,s^{-1}}$). This source term was defined based on the nature of the computational zone. Here a zone is either the entire computational domain or sub-domain where specific governing equations are to be employed or customized. In any locations where

[1]Not to be confused with the inertial resistance coefficient (S) in Eq. 2.5.

AlP tablets are placed $S = S_{PH_3}$ and is defined as

$$S_{PH_3} = \varepsilon \frac{\dot{m}}{V} \tag{2.16}$$

where $\dot{m}$ ($\mathrm{kg\,s^{-1}}$) is the PH_3 releasing rate ($\dot{m}$ is x in Eq. 3.4, discussed in Chapter 3). The evolution rate of PH_3 is temperature and relative humidity dependent, which was also included in the simulations, so the response of the rate in each PH_3 region depends on the average temperature in that region. The area weighted average of temperature in each AlP zone was calculated as $\frac{1}{A}\iint T\, dA$. In any zone without AlP, S_{PH_3} was set to zero.

In zones where wheat is present, sorption occurs (Darby, 2008). The two coupled ordinary differential equations of Darby (2008) were adopted. These equations are discussed in Chapter 3. The effect of sorption was added as a source term. In this case, $S = S_{sorp}$ and it takes the form

$$a_1 \varepsilon \rho_g Y_{PH_3 \to air} + a_2 \varepsilon \rho_g Y_{PH_3 \to kernel} \tag{2.17}$$

where $Y_{PH_3 \to air}$ is the mass fraction of PH_3 in air and $Y_{PH_3 \to kernel}$ is the mass fraction of PH_3 in the wheat kernel. To calculate the mass fraction of PH_3 in the wheat kernel, a user scalar equation was written and linked to ANSYS Fluent and it takes the form

$$\frac{\partial(\rho_g Y_\omega)}{\partial t} = a_3 \varepsilon Y_{PH_3 \to air} - a_4 \varepsilon \rho_g Y_{PH_3 \to kernel} \tag{2.18}$$

a_1, a_2, a_3, and a_4 are constants of Eq. 3.8 in Chapter 3.

In zones with no AlP tablets nor wheat i.e., headspace, $S_{PH_3} = S_{sorp} = 0$. The momentum equation can be described as

$$\frac{\partial(\varepsilon \rho_g \vec{v})}{\partial t} + \nabla \cdot (\varepsilon \rho_g \vec{v}\vec{v}) = -\varepsilon \nabla p + \nabla \cdot (\varepsilon \overline{\overline{\tau}}) + \rho_g \vec{g} + \vec{S}_p + S\vec{v} \tag{2.19}$$

Eq. 2.19 without the last two terms is the standard momentum equation in vector form. The additional two terms were added to capture other physics in the problem. The last term, $S\vec{v}$, is the fluid velocity multiplied by S_{PH_3} in AlP tablet zones or S_{sorp} in a wheat zone.

The change in pressure caused by the presence of wheat (Section 2.2) was added through the term $\vec{S}_p$ and is defined as

$$\vec{S}_p = S_i = -\varepsilon^2 \left[D_{ij}\mu_g v_j + \varepsilon C_{ij} \frac{1}{2} |\vec{v}| v_j \right] \tag{2.20}$$

where v_j is the velocity component ($u = v_1$, $v = v_2$, $w = v_3$) in (x, y, z), respectively. The resistance that fluid experiences within the porous medium was assumed to be orthotropic (Hood and Thorpe, 1992). D_{ij} and C_{ij} have values only if $i = j$, (D_{xx}, D_{yy}, D_{zz}; C_{xx}, C_{yy}, C_{zz}), otherwise their values are zeros. The first term in Eq. 2.20 accounts for the viscous resistance while, the second term accounts for the inertial resistance. Values of D_{ij} and C_{ij} were calculated from Hood and Thorpe's data as discussed in Section 2.2.

In the energy equation, the thermal inertia of the solid is included in the transient term as

$$\begin{aligned} &\frac{\partial}{\partial t}\left[\left(\varepsilon\rho_g c_{p_g} + (1-\varepsilon)\rho_s c_{p_s}\right) T\right] + \nabla \cdot \left(\vec{v}\left(\rho_g c_{p_g} T + p\right)\right) = \\ &\nabla \cdot \left[k_e \nabla T - \rho_g c_{p_g} T \; D_{PH_3,e} \nabla Y_{PH_3} + \overline{\overline{\tau}} \cdot \vec{v}\right] + \left(c_{p_g} T\right) S \end{aligned} \tag{2.21}$$

In Eq. 2.21, c_{p_g} and c_{p_s} ($\mathrm{J\,kg^{-1}\,K^{-1}}$) are the specific heat at constant pressure of the gas mixture and the solid (wheat), respectively, ρ_s ($\mathrm{kg\,m^{-3}}$) is the density of the solid, T (K), is the temperature, $\overline{\overline{\tau}}$ is the shear stress tensor, $D_{PH_3,e}$ ($\mathrm{m^2\,s^{-1}}$) is the effective diffusion coefficient of PH_3 into air within the porous medium, and Y_{PH_3} is the mass fraction of PH_3. The last term is an additional source term in which $S = S_{PH_3}$ in a region of AlP tablets or $S = S_{sorp}$ whenever wheat is present.

The density of the mixture was calculated as

$$\rho_g = \frac{p_{atm} + p}{\frac{R}{Mw_g} T} \tag{2.22}$$

where p_{atm} (Pa) is the atmospheric pressure (operating pressure), p (Pa) is the predicted pressure, R ($\mathrm{J\,kmol^{-1}\,K^{-1}}$) is the universal gas constant, and Mw_g ($\mathrm{kg\,kmol^{-1}}$) is the molec-

ular weight of the gas mixture and it can be obtained from

$$Mw_g = X_{PH_3} Mw_{PH_3} + X_{air} Mw_{air} = \left(\frac{Y_{PH_3}}{Mw_{PH_3}} + \frac{Y_{air}}{Mw_{air}} \right)^{-1} \tag{2.23}$$

In Eq. 2.23, X_{PH_3} and X_{air} are the mole fraction of the PH_3 and air, respectively, and can be obtained from the mass fraction as $Y_i = X_i \frac{Mw_i}{Mw_g}$, with i is the PH_3 or air. In all simulations, the air was assumed to be a single component without dealing with its composition. So, only two mass fractions needed to be solved, air and PH_3. However, only one species equation, for PH_3, was solved as

$$\frac{\partial(\varepsilon \rho_g Y_{PH_3})}{\partial t} + \nabla \cdot (\varepsilon \rho_g \vec{v} Y_{PH_3}) = \nabla \cdot (\rho_g D_{PH_3,e} \nabla Y_{PH_3}) + S \tag{2.24}$$

Since $Y_{PH_3} + Y_{air}$ must equal 1, the mass fraction of air was obtained. As before, S is defined based on the type of the zone in which it was assigned to AlP tablets or wheat. For both the thermal conductivity and the viscosity of the mixture, they were calculated based on the kinetic theory as

$$k_g \text{ or } \mu_g = \sum_i \frac{X_i \ \mu_i}{\sum_j X_j \ \varphi_{ij}} \tag{2.25}$$

$$\varphi_{ij} = \frac{\left[1 + \left(\frac{\mu_i}{\mu_j} \right)^{0.5} \left(\frac{Mw_j}{Mw_i} \right)^{0.25} \right]^2}{\left[8 \left(1 + \frac{Mw_i}{Mw_j} \right) \right]^{0.5}} \tag{2.26}$$

and the specific heat, at constant pressure, was calculated from

$$c_p = Y_{PH_3} \ c_{p_{PH_3}} + Y_{air} \ c_{p_{air}} \tag{2.27}$$

2.3.1 Effective diffusion coefficient

Diffusion of PH_3 into air as a function of temperature can be estimated as a binary mixture using Lennard-Jones parameters (for details, see Chapman and Cowling, 1990). As bulk wheat constructs porous media, the diffusion coefficient is restricted by the pore volume, which varies along the diffusion path, as well as the tortuosity of the wheat bed. Therefore, it needs to be adjusted. The effective diffusion coefficient in Eqs. 2.21 and 2.24, is the molecular diffusion coefficient multiplied by some factor that accounts for the presence of wheat. This factor is a function of the porous media properties, porosity and tortuosity. The variation of the cross sections and tortuosity is usually combined into one parameter and is called the obstructive coefficient (Thorpe, 1981). For wheat, this coefficient was found to be 0.53 (Thorpe, 1981) which lies in range found experimentally by Van Brakel and Heertjes (1974) of 0.5 to 0.6 for non-uniform packed beds of deformed and undeformed spheres. A comparison was made between published experimental work on the effective diffusion coefficient of wheat (Bundus et al., 1996; Oxley and Henderson, 1944; Shunmugam et al., 2005; Singh et al., 1984) in addition to results of Thorpe (1981) with two commonly used correlations for effective diffusion coefficients in porous media (Bruggeman, 1935; Millington and Quirk, 1961). Some of those results were for CO_2 and that was adjusted by eliminating the molecular diffusion of CO_2 and replacing it with the one of PH_3. Figure 2.5 shows a plot of the comparison as a function of temperature. Shunmugam et al. (2005) concluded that his results are higher than other experimental data of Oxley and Henderson (1944) and Singh et al. (1984) and he suggested the increase is because of the effect of viscous flux in this experiment. Based on this, both the results of Bundus et al. (1996) and Shunmugam et al. were seen as higher values and eliminated from the choice. Both correlation of Bruggeman (1935) and Millington and Quirk (1961) show reasonable results and could be considered for granular materials. However, results of Millington and Quirk act as an average value and was taken for all simulation in this study.

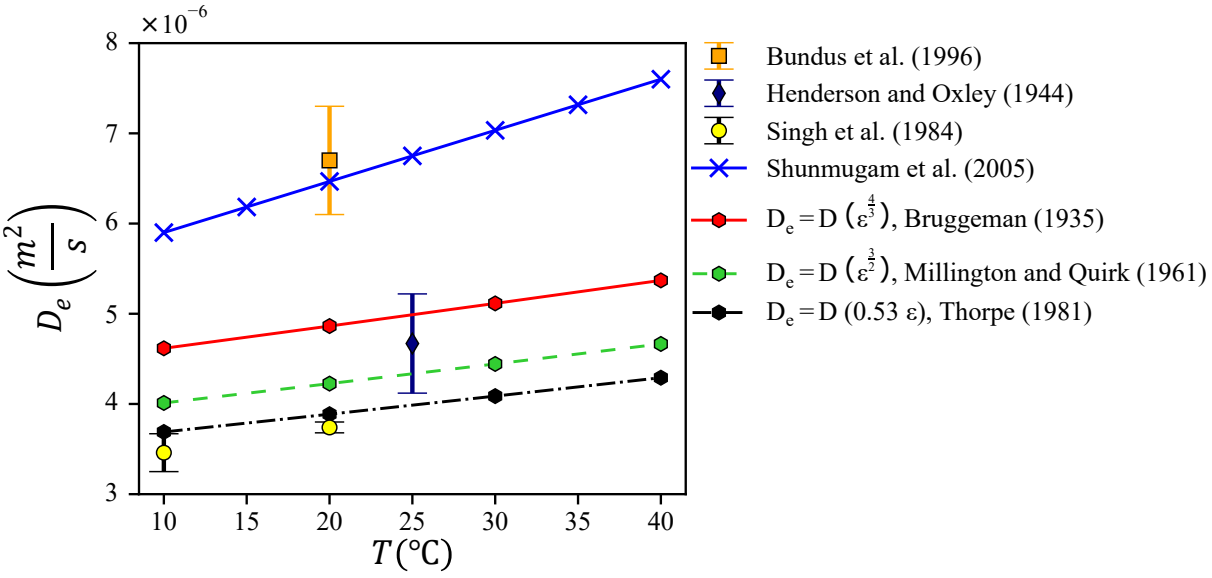

Figure 2.5: Comparison between different definitions for the effective diffusion coefficient of PH_3 in wheat.

ANSYS Fluent uses a finite volume method to discretize the governing equations. Unless otherwise stated, the coupled scheme was used for the velocity–pressure coupling. Schemes used for the spatial discretization are: PRESTO for pressure and the second order upwind for the momentum, energy, species, and scalar (user defined equation for PH_3 in wheat kernels) equations. The first order implicit scheme was used for temporal discretization.

2.4 Estimating resistance coefficients

In Section 2.2, experiments were the only method used for obtaining the resistant coefficients of wheat or any other grain to gas flow. In this section, a new technique is proposed that does not require any experimental work rather just CFD simulations. The minimum and the maximum coefficients of the resistance could be reasonably estimated through a set of simulations. The main advantage of this method is one can understand the the actual weight or contribution to the coefficients caused by different factors discussed in Section 2.2.2.

The process starts by obtaining a 3D scanned image of a grain kernel of any size. Then using a 3D CAD modeling software, the image is cleaned up and smoothed. ANSYS SpaceClaim 2021R1 was used for this step. Figure 2.6 shows the final output of a wheat kernel

with dimensions. The second step is by orienting the wheat kernels in such a way that they construct a periodic pattern. As the kernel has an irregular shape, different orientations can create periodicity. In this case, three configurations were obtained. Figure 2.7 shows the three different periodic patterns constructed from the single kernel. From each configuration, one period is needed for the CFD model. Pressure loss was found to be highest in the vertical direction. As a result, with two successive layers of the vertical orientation, the worst case scenario is obtained, i.e., the maximum resistance occurs. Figure 2.8 shows the computational domain for four different configurations including the worst case scenario.

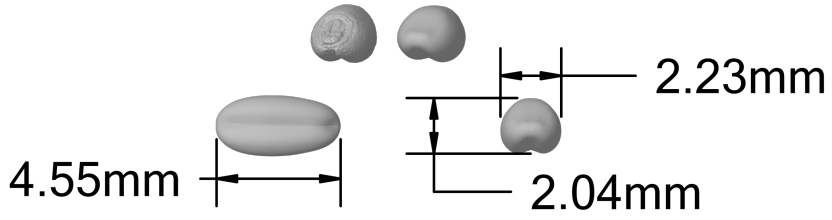

Figure 2.6: Different views of the wheat kernel with dimensions obtained from a 3D scanned image – before and after cleaning.

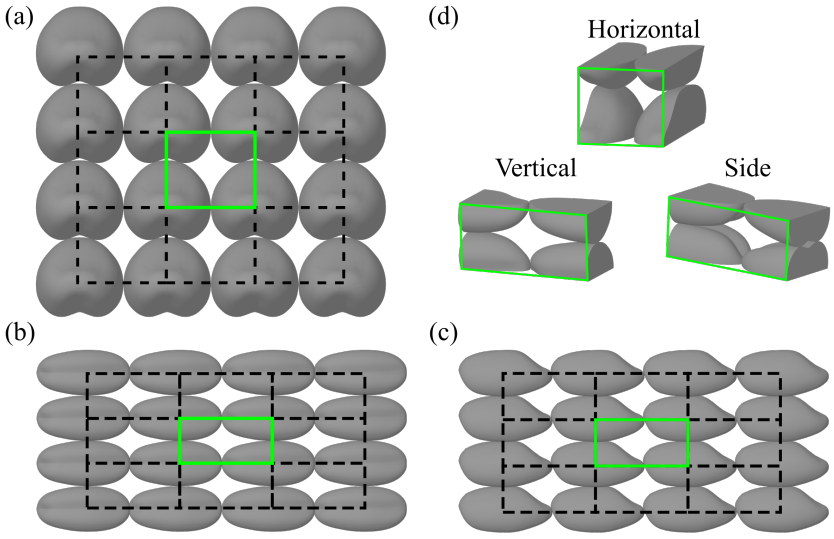

Figure 2.7: Three different periodic patterns obtained from the wheat kernel; (a) horizontal flow, (b) vertical flow, (c) flow from the side of the kernel, and (d) one period from each orientation (a, b, c).

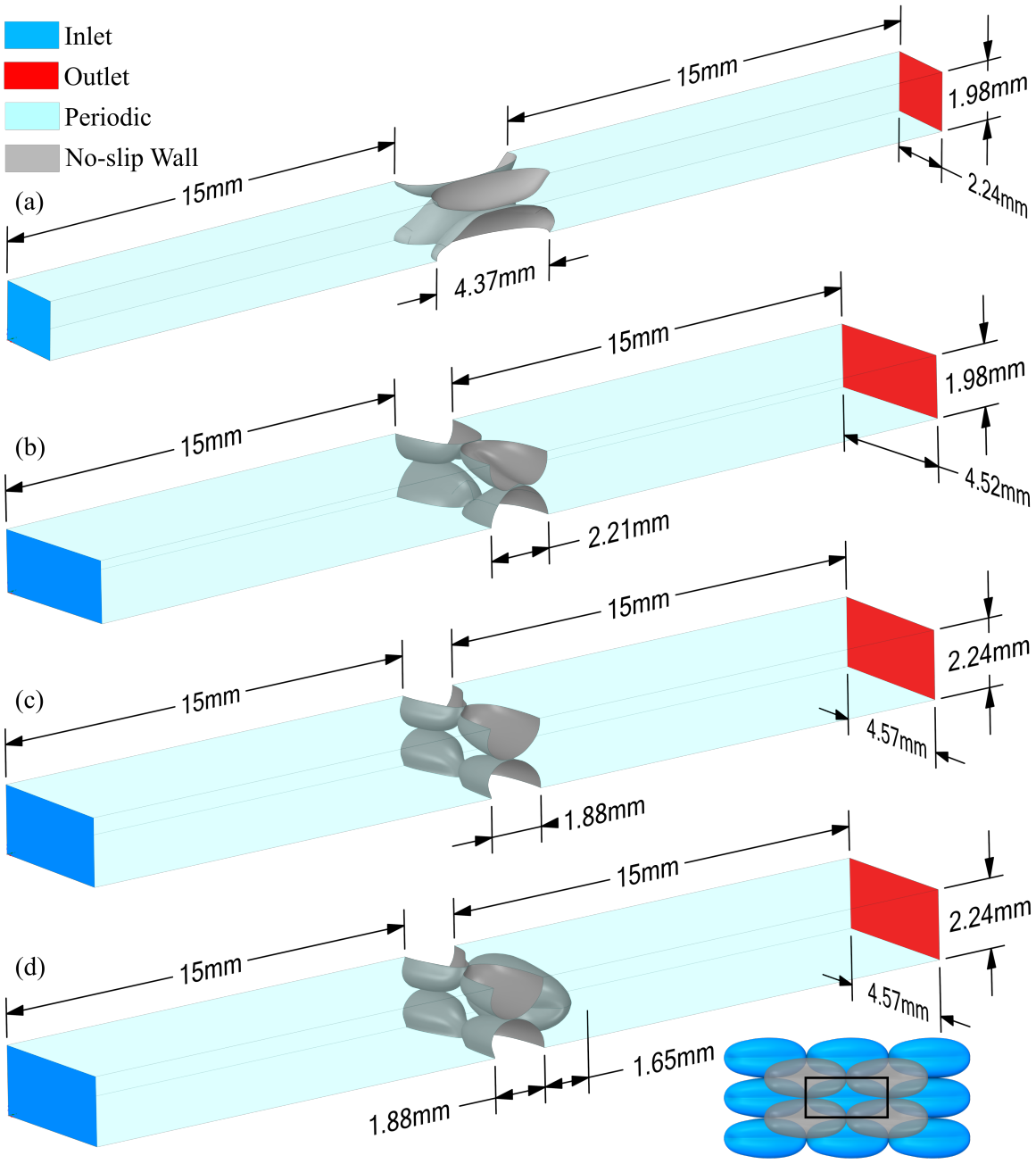

Figure 2.8: Computational domain with boundary conditions for four different orientations of wheat kernels; (a) horizontal flow, (b) flow from the side of the kernel, (c) vertical flow, and (d) two layers of the vertical flow orientation.

Generating a good mesh for those domains is a very critical process because of the very small gaps between kernels. Mosaic mesh is a useful technique in this case, as those gaps are filled with polyhedral elements of any size while the rest of the domain is filled with

hexahedral elements. Figure 2.9 shows the generated mesh for the worst case scenario. In this simulation, the main governing equations of fluid flow were utilized with no customization. Figure 2.10 shows the static pressure contours of (a) the horizontal orientation, (b) the side orientation, (c) the vertical orientation, and (d) the worst case scenario.

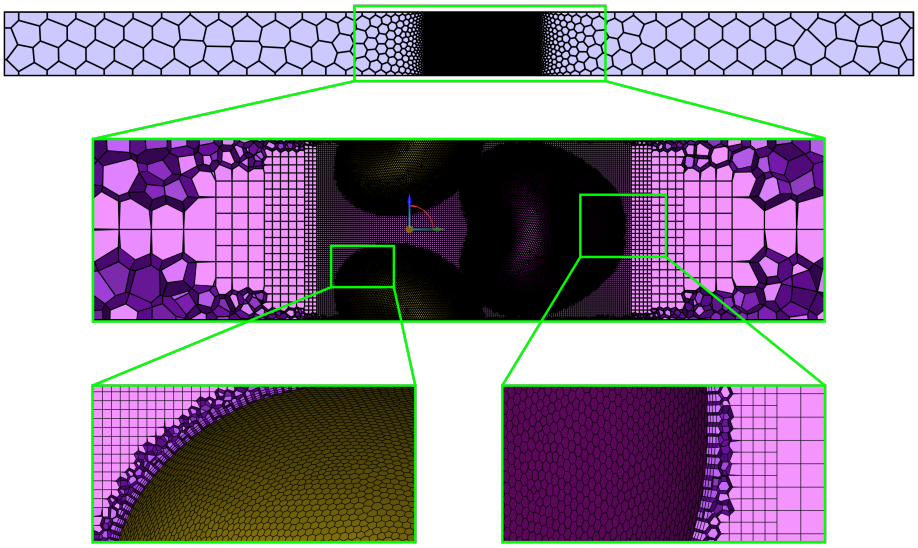

Figure 2.9: Mosaic mesh (polyhedral and hexahedral) generated for the two layers scenario.

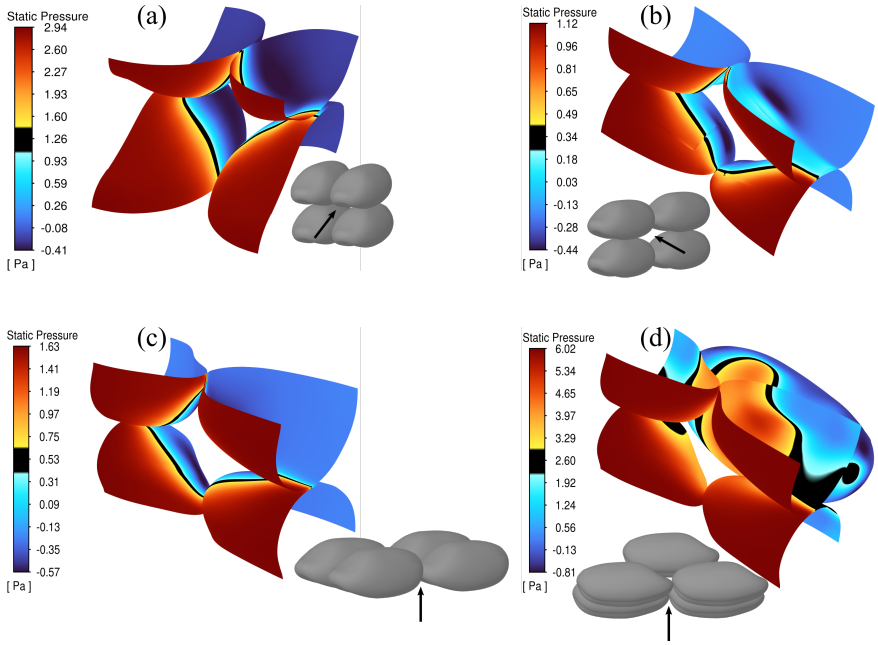

Figure 2.10: Contours of static pressure (Pa) resulted from the CFD simulation; (a) horizontal flow, (b) flow from the side of the kernel, (c) vertical flow, and (d) two layers of the vertical flow orientation.

The effects of the flow direction are shown in Figure 2.11. As seen, from the relationship between the pressure drop per unit length ($\mathrm{Pa\,m^{-1}}$) versus the magnitude of the velocity ($\mathrm{m\,s^{-1}}$) in each direction, the highest pressure drop resulted from the vertical direction followed by the horizontal direction, while the lowest resistance resulted from the side direction. Figure 2.12 shows the relationship between the pressure drop and velocity at three different sizes. Since the velocity is non-linear, the size of the pore changes the pressure drop; the smaller the kernel the higher the loss in pressure. Finally, Figure 2.13 shows a comparison between the experimental data of Molenda et al. (2005a) at two different porosities ($\varepsilon = 0.35$ and $\varepsilon = 0.45$) and the CFD results. Both the experimental data and the CFD results represent the highest and lowest resistance obtained. As seen, the maximum pressure loss resulted from the CFD simulation coincides with the experimental data of the smallest porosity, while the minimum pressure loss of the CFD simulation is higher than the minimum pressure loss from the experiment. This is because the CFD results used in the comparison was for one kernel size. Figure 2.12 showed that bigger kernels will result in lower pressure loss. More research may reveal the exact weight and contribution of each factor such as kernel size, other different orientations, or even fine materials.

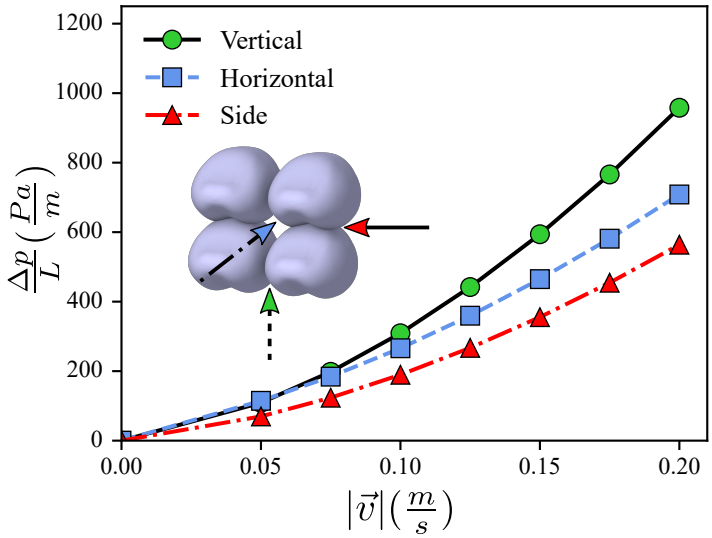

Figure 2.11: Pressure drop per unit length ($\mathrm{Pa\,m^{-1}}$) versus the magnitude of the velocity ($\mathrm{m\,s^{-1}}$) in each flow direction; vertical (—●—), horizontal (- -■- -), and side (-·-▲-·-).

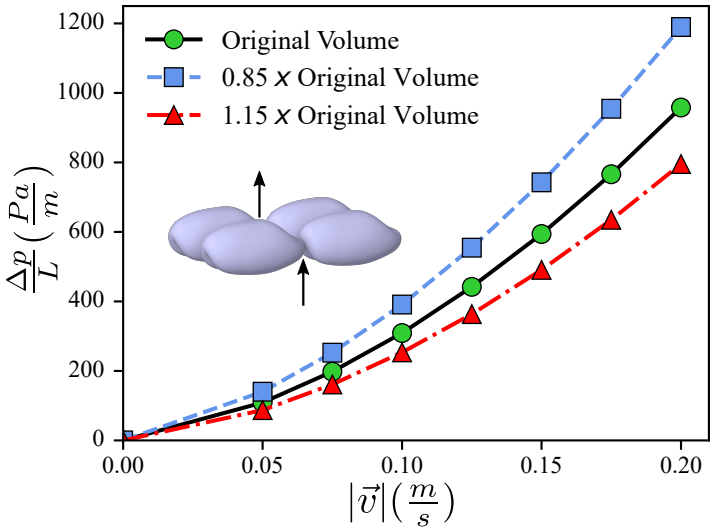

Figure 2.12: Pressure drop per unit length ($\mathrm{Pa\,m^{-1}}$) versus the magnitude of the velocity ($\mathrm{m\,s^{-1}}$) for three different kernel sizes (original —●—, small - -■- -, large - -▲- -) of flow from vertical direction.

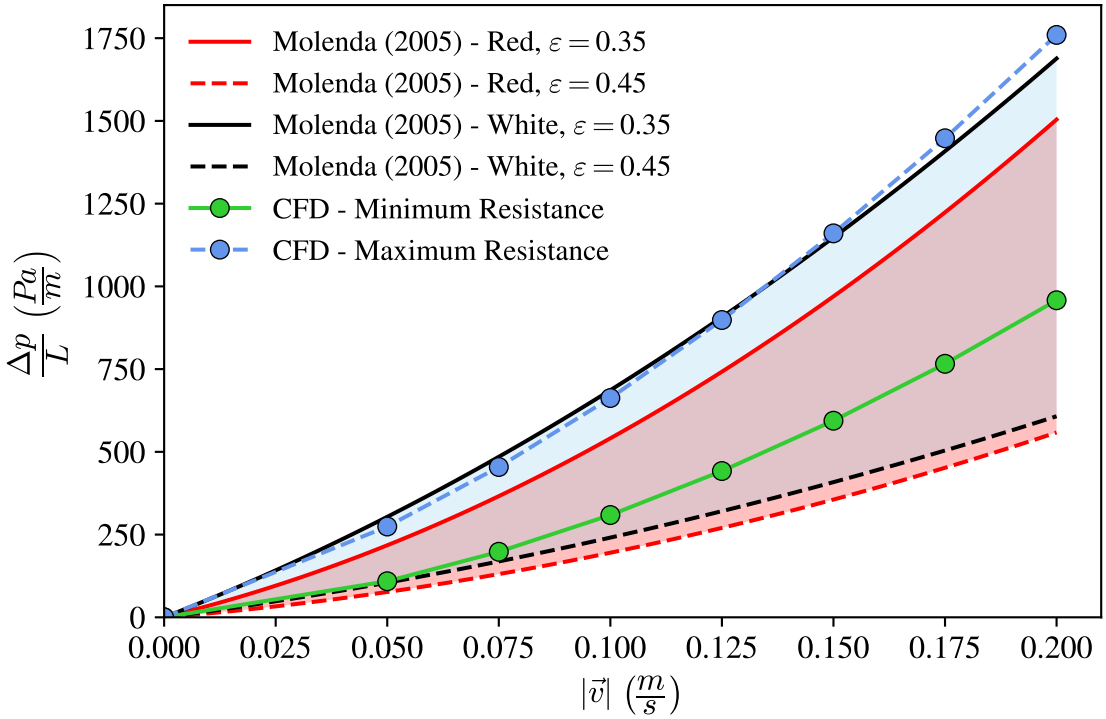

Figure 2.13: Comparison between the experimental data of Molenda et al. (2005a) at two different porosities (Red Wheat ε = 0.35 —, Red Wheat ε = 0.45 - - -, White Wheat ε = 0.35 —, and White Wheat ε = 0.45 - - -) that represents the heights and lowest pressure drop observed from the experiment and results from the CFD model of the two layers scenario as the maximum resistance (- -●- -) and the flow from the side case that represents the minimum resistance (—●—) obtained.

Chapter 3

Releasing Rate of Phosphine

3.1 Objective

The main objectives of this chapter were to (1) Derive a mathematical relationship for the PH_3 decomposition rate as a function of both temperature and relative humidity (RH) based on published data (Tan, 1994), (2) Develop a CFD model that utilizes the derived relationship, and (3) Describe the effect of sorption (Darby, 2008, 2011) of PH_3 into wheat as a function of temperature into the developed model. The releasing rate equation was compared to experimental data of Couch and Shaheen (1984) and the CFD model was validated against laboratory experiments.

3.2 Relationship for Evolution Rate

An AlP (aluminum phosphide) tablet weighs approximately 3 g and produces 1 g of PH_3 when in contact with moist air, while an AlP pellet weighs 0.6 g and produces 0.2 g of PH_3 (Formato et al., 2012). The decomposition of the AlP formulation is affected by temperature (T) and relative humidity (RH) (Rajeshekar et al., 2006; Tan, 1994). A mathematical relationship was developed based on the experimental data from Tan (1994) to account for the decomposition rate. The maximum evolution rate as a function of the absolute humidity

was well described by the following kinetic equation for a single tablet weighing 3 g and producing 1 g of PH_3 (Banks, 1991)

$$X = \phi \, (\alpha \, \omega + \beta \, \omega^2) \tag{3.1}$$

where X is the maximum evolution rate ($g\,h^{-1}$), ϕ is the number of tablets, ω is the absolute humidity ($g\,m^{-3}$), and α and β are constants. When ϕ has a value of 1, this equation describes the evolution from one tablet that weighs 3 g and produces 1 g of PH_3. The values of α and β were chosen to match the experimental data of Tan (1994). A MATLAB code was written to iterate over a broad range of values for α and β for a given T and RH combination; the process was repeated for all other T and RH values. The values that gave a maximum evolution rate with the smallest deviation, when compared to Tan's data, were chosen and used in this study: $\alpha = 2.35 \times 10^{-3}\,m^3\,h^{-1}$ and $\beta = -0.75 \times 10^{-5}\,m^6\,g^{-1}\,h^{-1}$, with a standard error of $0.04\,g\,h^{-1}$ and R^2 of 0.965. The absolute humidity as a function of both T and RH was obtained from the definition of the RH and the ideal gas law. Relative humidity is the ratio of the actual vapor pressure (P_w) at any T to the saturated vapor pressure of water (P_s) at that T. P_s can be obtained from the empirical formula derived by Bolton (1980) and is expressed as

$$P_s = 611.2 \; e^{\frac{17.67 \; T}{T + 243.5}} \tag{3.2}$$

where P_s is in Pa, and T is in °C. By substituting $P_w = P_s \cdot RH$ in the ideal gas law, the absolute humidity ($g\,m^{-3}$) can be expressed as

$$\omega = \frac{13.243 \; RH \; e^{\frac{17.67 \; T}{T + 243.5}}}{T + 273.15} \tag{3.3}$$

A comparison between the maximum evolution rate obtained from Eq. 3.1 and the experimental results of Tan (1994), with 10 AlP tablets ($\phi = 10$), against the absolute humidity is shown in Figure 3.1. The equation agreed with the data, especially in the normal range

of moisture content for wheat (Molenda et al., 2005a). As shown in Figure. 3.1, the maximum deviation occurred at 20 °C and 90% RH, with about 0.35 g h^{-1} of PH_3 from Eq. 3.1 compared to 0.4193 g h^{-1} from the experiment. The values from Eq. 3.1 for 30 °C and 50% RH and for 30 °C and 70% RH, which are the likely range of conditions for field fumigation, matched well with the experiment, with percentage error of 3% and 7.5%, respectively.

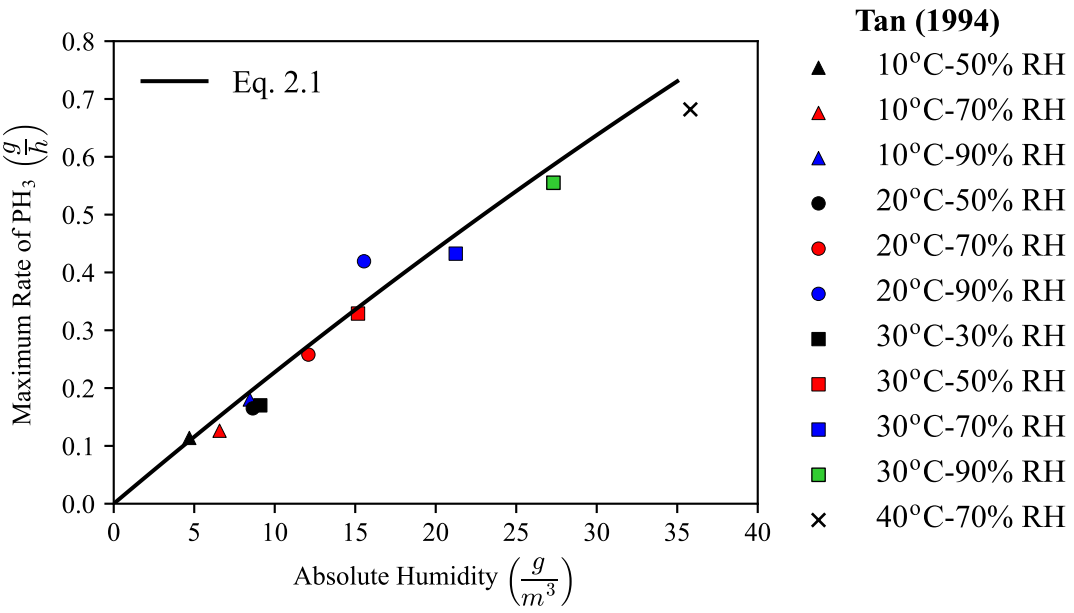

Figure 3.1: Maximum phosphine released from ten AlP tablets at different temperature and relative humidity levels for the experimental data from Tan (1994) (symbols) and the results from Eq. 3.1 (—).

From Tan's (1994) data, it was observed that the shape of the decomposition rate at any T and RH is similar to a Rayleigh distribution. After evaluating the mathematical formulas that capture these curve shapes, the evolution rate was found to follow a function of the form

$$x(t) = X\ e^{-\left(\frac{t}{\gamma}\right)^2} \tag{3.4}$$

where x is the evolution rate (g h^{-1}), t is the time (h), and the value of γ (h) was found to be dependent on the maximum rate (X) and the number of tablets (ϕ) as

$$\gamma = \frac{10\phi}{9X} \tag{3.5}$$

A MATLAB code was written for estimating γ by comparing the area under the curve from Tan's (1994) data and Eq. 3.4 with a standard error of 0.51 g of PH_3. In this case, the area under the curve represents the amount of PH_3 released. With 1 g of PH_3 per one AlP tablet, the expected amount of PH_3 is 10 g. Another parameter considered while finding γ is to maintain the amount of PH_3 released as close to 10 g as possible with a maximum error of 2.71%. Eq. 3.4 can be evaluated for any number of tablets or pellets, and the amount of phosphine released at any time can be estimated.

Comparisons between the results obtained from Eq. 3.4, with $\phi = 10$ and the experimental data from Tan (1994) for different T and RH levels are shown in Figure 3.2. The initial rise to a peak for the experimental data did not yield any consistent shape and was ignored in Eq. 3.4 as a result. Apparently, there was insufficient temporal resolution in Tan's (1994) data to capture the quick initial ramp to the peak value. The resulting error due to the assumption of an immediate peak was less than 5% based on comparing the area under the curve between the experimental data and the analytical results. Both the final time, when PH_3 was fully released, and the maximum decomposition rate are almost identical for the results of Eq. 3.4 and Tan's data, with minor deviations for 20 °C and 50% RH and for 20 °C and 90% RH. The final release time for those two deviated cases varied by about 10 h for a small amount of PH_3, less than 0.05 g h^{-1}, while the maximum rate, Eq. 3.1, deviated from Tan's data by about 0.05 g h^{-1}. An AlP pellet releases $\frac{1}{5}$g of PH_3, so the relationship in Eq. 3.4 could also be used for pellets simply by replacing ϕ with 0.2ϕ.

The evolution rate formula in Eq.3.4 was compared with other experimental data from Couch and Shaheen (1984). Their experiment was conducted in a 1 m^3 gas-tight chamber. The dosage tested was 1 g of phosphine. Temperatures ranged from 20 °C to 22 °C. The humidity inside the chamber was controlled to achieve RH levels of 85% to 95% and 45% to 55%. Figure 3.3 shows a quantitative comparison between the results obtained from Eq. 3.4 for 1 g of PH_3 and the two experimental data (Couch and Shaheen, 1984; Tan, 1994). Data from Tan that capture the full range of Couch and Shaheen are not available, so the closest values were used for the comparison: at 20 °C and 50% RH and at 20 °C and 90% RH from Figure 3.2. The predicted values do not fully span the experimental measurements

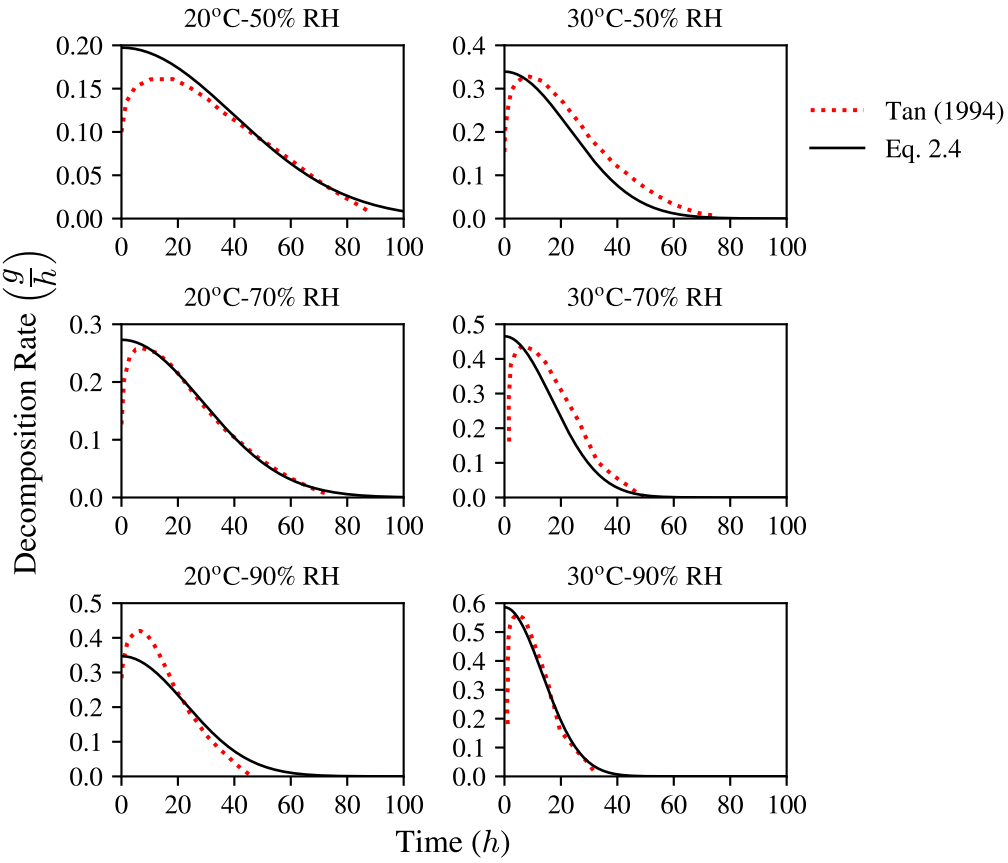

Figure 3.2: Evolution rate of PH_3 ($g\,h^{-1}$) from ten AlP tablets versus time (s) at different temperature and relative humidity levels for data from Tan (1994) (·····) and results from Eq. 3.4 (——).

from Couch and Shaheen at 90% PH_3 release for RH of 85% to 95%, but they are much closer to Tan's data. Based on Eq. 3.4, 90% of the 1 g of PH_3 was released within 35.75±35.75h, compared to about 30 h for Tan and 23.3±4.0h for Couch and Shaheen, i.e., using Eq. 3.4, 90% of the PH_3 required more time to be released than in Couch and Shaheen's experiment by 4.9 h to 20 h, compared to about 5 h for Tan. In addition, as shown in Figure 3.2, the results from Eq. 3.4 and from Tan's data at 20 °C and 90% RH deviated the most compared to the results at other temperature and RH levels.

A similar result occurred for 50% release at 45% to 55% RH, for which the calculated value was 24.75±3.6h compared to 24 h from Tan (1994), while the experimental value from Couch and Shaheen (1984) was 32.5 h, which differs from both the predicted values and from Tan's data. However, Couch and Shaheen's data for this range of temperature and

RH was for only one trial, so the range of the experimental values is not known but may well overlap with the calculated values because the smallest deviation was about 4.1 h. Tan's experiment was more robust than Couch and Shaheen's because temperature, relative humidity, and airflow rate were controlled, and multiple trials were conducted, while Couch and Shaheen performed a basic experiment with limited trials. For all other values of PH_3 release, the calculated values overlapped with the experimental data.

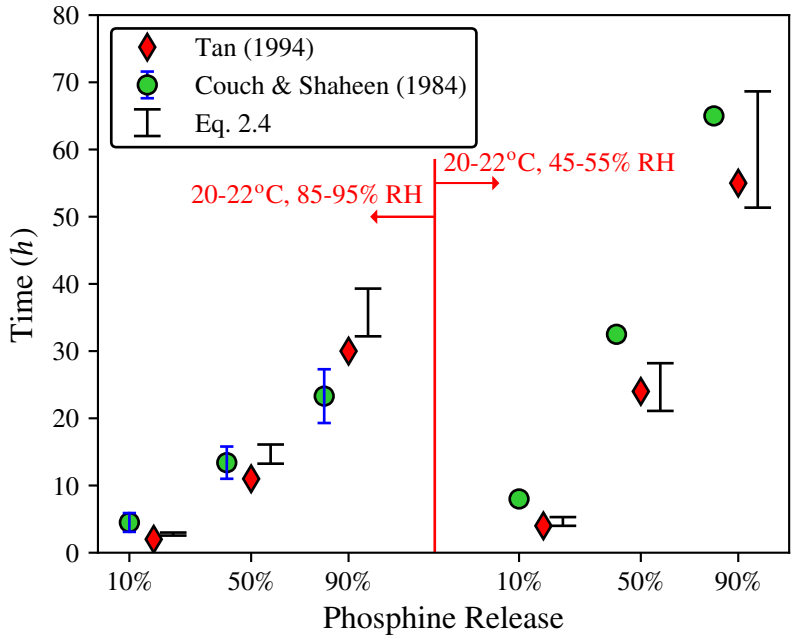

Figure 3.3: Time for partial phosphine release (10%, 50%, and 90%) from 1 g of PH_3 between results of Eq. 3.4 I and experimental data of Tan (1994) ◆ & Couch and Shaheen (1984) ●. Data from Tan were available at 20 °C and 50% *RH* and at 20 °C and 90% *RH*, while data from Couch and Shaheen were available as a range for 85% to 95% *RH* with multiple trials but with a fixed value for 45% to 55% *RH* with one trial.

3.3 CFD Model Development

The main purpose of the releasing rate relationship (Eq. 3.4) was to be utilized in CFD modeling. To test its applicability, 2D CFD simulations using ANSYS Fluent 19.1 software, with and without wheat, were built. Laboratory experiments were conducted to validate both the CFD models and Eq. 3.4.

3.3.1 Empty volume

3.3.1.1 Experiment

An experiment on a 0.208 m^3 empty sealed barrel was conducted. The barrel was treated with 1 AlP pellet placed at its bottom in the center. A wireless sensor (Centaur Analytics, Ventura, Cal.) was placed in the center of the barrel (next to the pellet) to measure both PH_3 concentration and temperature. This sensor has a range of 0 ppm to 2000 ppm with an accuracy of ±5% for PH_3 and a range of −40 °C to +80 °C with an accuracy of ±0.5 °C for temperature. It sends data through a cellular device to cloud-based software. Data from the sensor were collected hourly. The barrel was placed in a closed, empty grain bin to minimize the effect of temperature fluctuations.

3.3.1.2 Simulation

Because the barrel used in the laboratory experiment was cylindrical and both the pellet and the sensor were placed in the center bottom, a 2D axisymmetric model was built for half of the domain in r–z coordinates. Figure 3.4 shows the computational domain with dimensions and the boundary conditions. The computational domain was divided into two distinct zones; one for the barrel while the other for the AlP pellet. Dividing the domain into zones allowed solving customized equations for each zone. The entire domain was discretized into small control volumes. The quality of the mesh is the basis for an accurate simulation. A structured quadrilateral grid was built with a finer grid around the pellet, as shown in Figure 3.5. ANSYS ICEM CFD 19.1 was used for both the geometry and the mesh

generation.

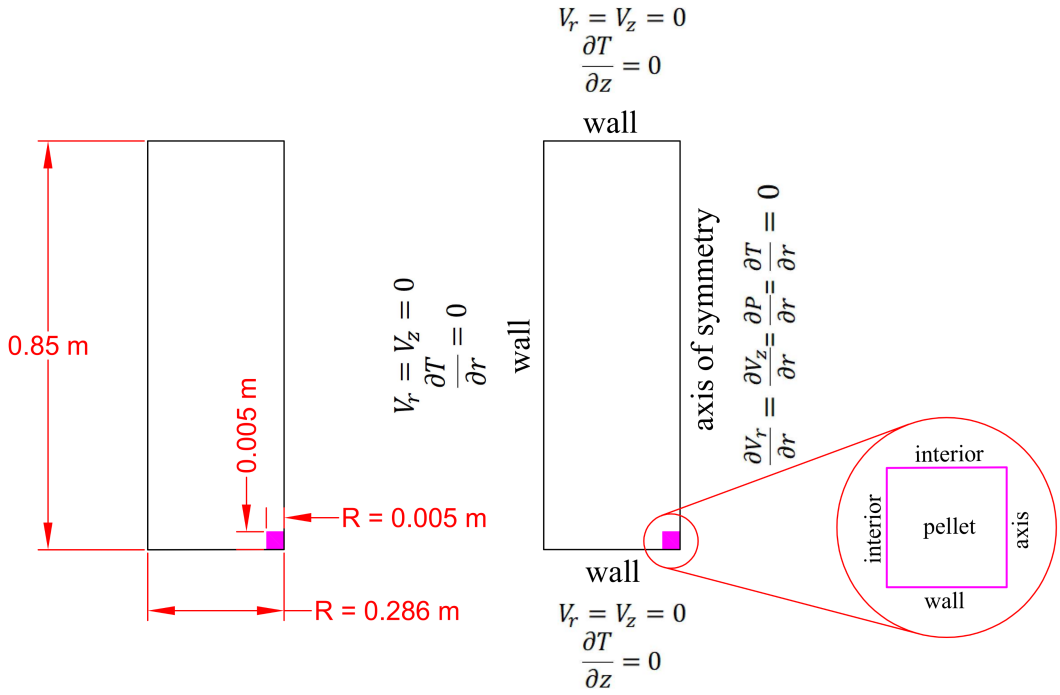

Figure 3.4: Dimensions of the barrel used in laboratory experiments, computational domain for the empty case, and boundary conditions (not to scale).

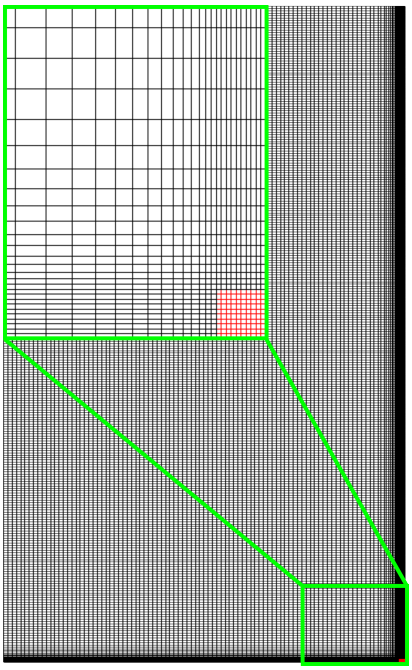

Figure 3.5: Structure mesh generated for the barrel simulation, zoomed-in around the AlP pellet.

3.3.1.2.1 Grid test a grid independence test, with three different mesh sizes (fine, medium, and coarse) was performed to ensure convergence. The fine mesh had 130,088 elements, the medium mesh had 32,924 elements, and the coarse mesh had 8,432 elements. The results from the three mesh sizes coincided, as shown in Figure 3.6(a), and the medium mesh was chosen for all simulations.

3.3.1.2.2 Time-step test a time-step test was also performed to ensure stability, and no significant variation was observed for times steps up to 60 s as shown in Figure 3.6(b). The time-step of 60 s was selected to minimize the computational time.

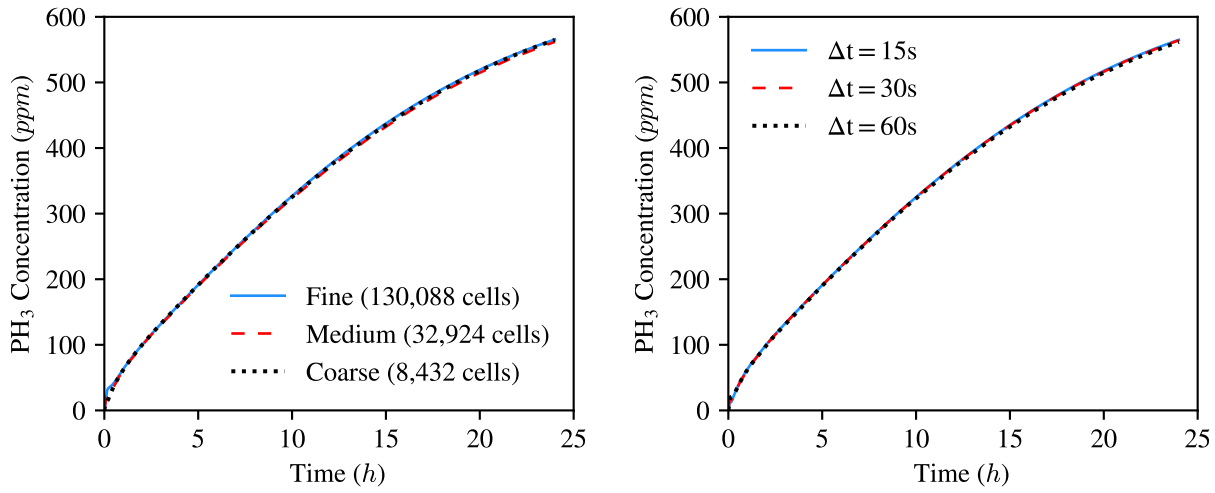

(a) Grid test (b) Time-step test

Figure 3.6: PH_3 concentration (ppm), at a distance of 12.5 cm from the bottom of the barrel, with (a) three different mesh sizes (fine ——, medium - - -, coarse ·····) and (b) three different time-steps (15 s ——, 30 s - - -, 60 s ·····).

The results from the CFD model were compared with the laboratory experiment. Figure 3.7 shows the change in the PH_3 concentration (ppm) with time (h). Data from the wireless sensors were collected hourly for the duration of the experiments. However, data for every 2 h to 4 h are shown in the plots for easy visualization without loss of the curve shapes. The CFD solution was at T = 29 °C and 33 °C, while the experiments were conducted at T = 29 °C, 30 °C, and 33 °C in the replications. The reported temperatures from the experiments are averages over the time of the test. The results from the CFD model are in good

agreement with the experimental data at $T = 33\,°C$ because of the use of the evolution rate formula (Eq. 3.4); however, there was some deviation between the predicted results and the experiment at $T = 29\,°C$ and $30\,°C$ (Figure 3.7). Theoretically, all three replications should end up at the same concentration, which was the case between the CFD results at $T = 29\,°C$ and $33\,°C$, because the pellet released $0.2\,g$ of PH_3 within the same volume regardless of the temperature. A mass balance check was performed by employing the equation of state for a constant volume, and the results showed that the final concentration of the case at $T = 33\,°C$ is correct, while the other two replicates were lower than the mass balance result. In addition, at $T = 29\,°C$ and $30\,°C$, from the experiment, the concentration started to decline at $40\,h$, which was not expected because there was no wheat and therefore no obvious sink due to sorption existed. There may have been leakage around the barrel lid, or possibly an interaction occurred between the barrel material and the PH_3. At $T = 33\,°C$, there was almost no change in concentration after $40\,h$ until the end of the experiment.

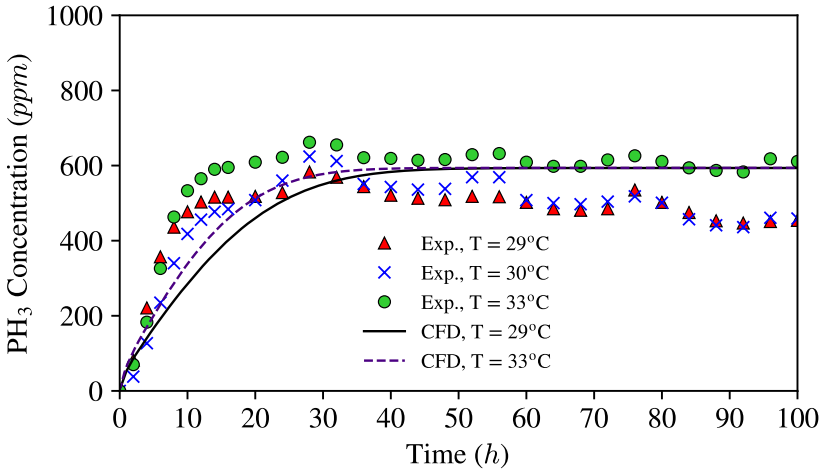

Figure 3.7: Comparison between CFD results ($T = 29\,°C$ —— and $T = 33\,°C$ - - -) and experimental data ($T = 29\,°C$ ▲, $T = 30\,°C$ ×, and $T = 33\,°C$ ●) based on PH_3 concentration (ppm) versus time (h).

3.3.2 Wheat-filled volume

Wheat bulks provide a porous media (Bakker-Arkema et al., 1969). The governing equations were discussed in Chapter 2. In Fluent, these effects are modeled by adding a sink term to

the momentum equation. This term acts as an external body force to account for the pressure drop, within the porous medium. Besides those changes in pressure and velocity, wheat may absorb and desorb some of the surrounding PH_3 (Banks, 1986; Daglish and Pavic, 2008; Darby, 2008; Reddy et al., 2007). The rate at which the grain absorbs the PH_3 must be defined in the governing equations; otherwise, the dosage needed to efficiently fumigate the storage facility may be miscalculated. The full set of the governing equations are also discussed in Chapter 2.

3.3.2.1 Effect of sorption

Darby (2008) developed three models to account for the effect of sorption. In this study, the second model was selected because it was simpler than the first model and both models have almost identical results when compared to his experimental data for wheat-PH_3, while the third model showed the poorest fit to the experimental data. Although experiments showed that the sorption rate increased as the temperature increased (Darby, 2011), those models were only valid at a constant temperature of 25 °C. In the second model, sorption is governed by two coupled ordinary differential equations as

$$\frac{dC}{dt} + \frac{S_{sorp}\ K_f}{B_{fill}}\ C - \frac{S_{sorp}\ K_f}{B_{fill}\ F}\ \omega = 0 \tag{3.6}$$

$$\frac{d\omega}{dt} - \frac{S_{sorp}\ K_f}{1-\varepsilon}\ C + \frac{S_{sorp}\ K_f}{(1-\varepsilon)\ F}\ \omega + K_{bind}\ \omega = 0 \tag{3.7}$$

and can be rearranged in a matrix form as

$$\begin{pmatrix} C'(t) \\ \omega'(t) \end{pmatrix} = \begin{pmatrix} -a_1 & a_2 \\ a_3 & -a_4 \end{pmatrix} \begin{pmatrix} C \\ \omega \end{pmatrix} \tag{3.8}$$

where C is the gas concentration in the intergranular air ($\mathrm{g\,m^{-3}}$), S_{sorp} is the specific surface area ($\mathrm{m^2\,m^{-3}}$), K_f is the linear mass transfer coefficient ($\mathrm{m\,h^{-1}}$), F is the partition factor

($\mathrm{kg\,kg^{-1}}$), K_{bind} is the coefficient of irreversible binding ($\mathrm{h^{-1}}$), ω is the gas concentration within the grain kernel ($\mathrm{g\,m^{-3}}$), and

$$B_{fill} = \varepsilon + \frac{1 - R_f}{R_f} \tag{3.9}$$

where ε is the porosity, and R_f is the filling ratio. In Eq. 3.8, a_1, a_2, a_3, and a_4 are constants, and their values depend on the type of grain and the fumigant being used (e.g., wheat and PH_3). Eq. 3.8 can be decoupled and solved analytically. The general solution can be expressed as

$$C(t) = b_1\ e^{r_1 t} + b_2\ e^{r_2 t} \tag{3.10}$$

$$\omega(t) = b_3\ \left(e^{r_1 t} - e^{r_2 t}\right) \tag{3.11}$$

where r_1 and r_2 are the roots of the auxiliary equation, and b_1, b_2, and b_3 are constants that depend on the initial conditions. Eq. 3.10 and Eq. 3.11 can be employed in a CFD model for PH_3 of gas forms but not for solid forms. With the gas form, the initial concentration of PH_3 is known and can be used for determining the constants in Eqs. 3.10 and 3.11. With solid forms, the PH_3 concentration varies with time. As a result, Darby's (2008) equations were solved numerically and validated against Darby's experimental results as well as the analytical solution (Eq. 3.10).

3.3.2.1.1 Sorption validation a 2D 1 m × 1 m CFD model was built to test the implementation of Darby's (2008) equations as well as to search for the parameter(s) that responds to the increase in the sorption rate as temperature increases. In the CFD model, Eq. 3.8 was solved numerically through a user-defined function (UDF) written in C and linked to the solver (information on the implementation is provided in Chapter 2.3). A time-step of 60 s was found to give results identical to the analytical solution of Eq. 3.10. Running multiple simulations and changing the values of the parameters in Eqs. 3.6 and 3.7, it was found that the change in sorption due to temperature is affected by the value of K_{bind}. The simulation results were compared to Darby's (2011) data until they fit for each temperature. Table 3.1

Table 3.1: Values for coefficient of irreversible binding (K_{bind}) at different temperatures (T).

T (°C)	K_{bind} (h^{-1})
15	0.025
22	0.035
25	0.050
30	0.065
35	0.500

shows the values of K_{bind} at each temperature.

Figure 3.8 shows the predicted results compared to Darby's experimental data (2008; 2011) at different temperatures. The CFD results at different temperatures with the corresponding K_{bind} from Table 3.1 agree fairly well with the experimental data at T = 15 °C, 22 °C, 25 °C, 30 °C, and 35 °C with R^2 values of 0.92, 0.97, 0.91, 0.94, and 0.96, and standard errors of 0.053, 0.053, 0.067, 0.07, and 0.057 g m^{-3}, respectively. The CFD results coincide with the results from the analytical solution, Eq. 3.10, which ensures the accuracy of the CFD model.

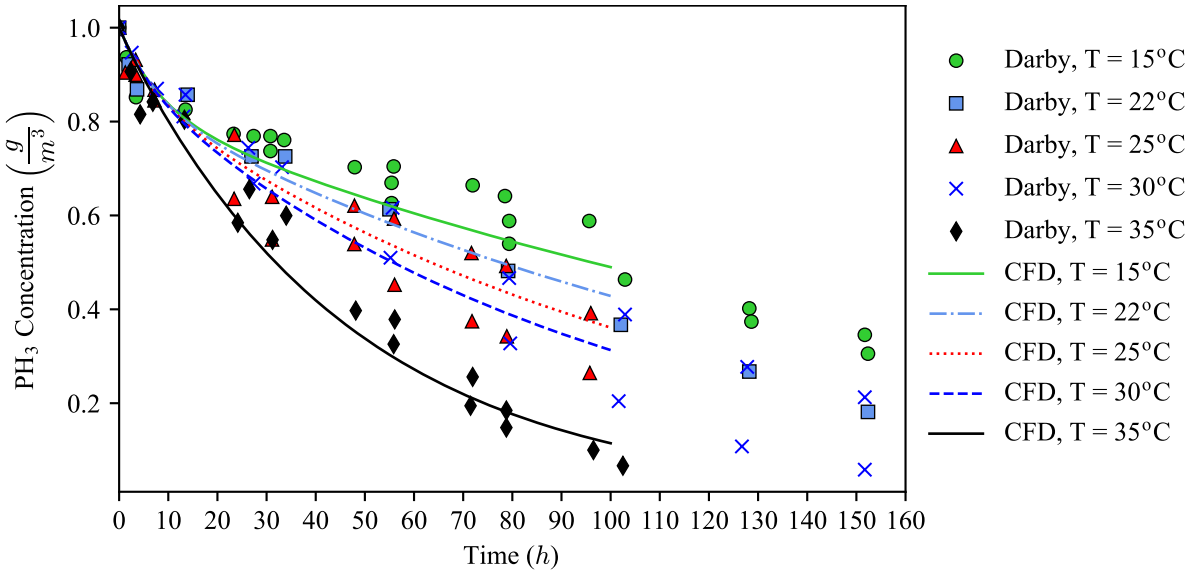

Figure 3.8: PH_3 adsorption by wheat at different temperatures based on CFD results (lines) and Darby's (2008; 2011) experimental data (symbols).

3.3.2.2 Simulation and validation

Two experiments similar to the one discussed in Section 3.3.1 were conducted but with wheat; one was half-filled with wheat while the other was full of wheat. This experiment used fresh hard red winter wheat. Figure 3.9 shows the experimental setup along with the location of the wireless sensor and the AlP pellet in the barrels. Ultimately, testing these varying configurations provided more robust validation of the model.

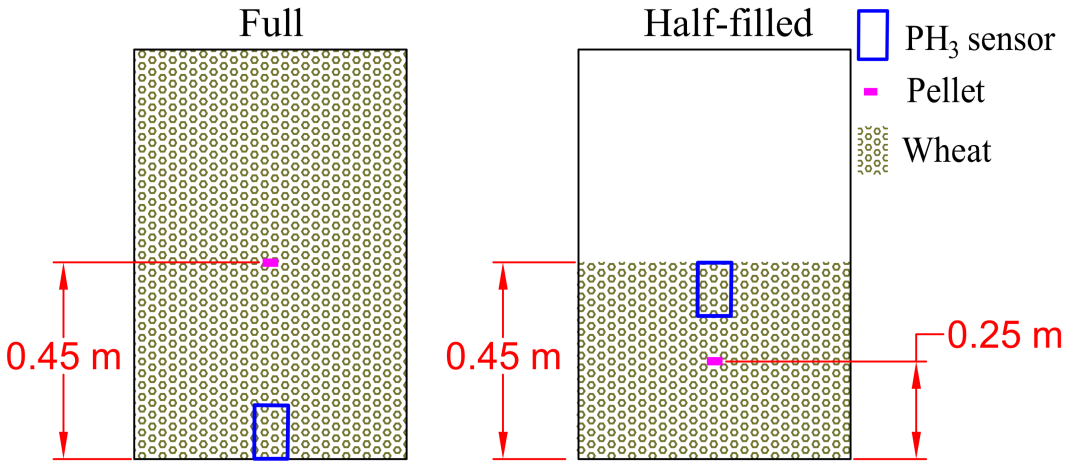

Figure 3.9: Schematic and dimensions of the experimental setup (not to scale).

For the half-filled with wheat case, experiments were conducted at average temperatures of 29 °C, 32 °C, and 33 °C. The CFD simulation of this scenario was performed at T = 29 °C and 33 °C. The PH_3 concentrations from the two CFD results showed only a slight difference, which indicates that a 4 °C temperature change is small. Figure 3.10 shows a comparison between the experimental and predicted data. The CFD results at T = 33 °C matched best with the experimental data of T = 29 °C but showed greater deviation from the experimental data at T = 32 °C and 33 °C.

For the full of wheat case, experiments were conducted at average temperatures of 30 °C, 32 °C, and 33 °C. The CFD simulation of this case was also performed at T = 29 °C and 33 °C. As shown in Figure 3.11, in the middle of the curve, the PH_3 concentration decreased as temperature increased due to sorption, and the final concentration at T = 30 °C was lower than the concentration at T = 32 °C. This was not expected and could be due to temperature

fluctuations or to leakage. The data at 30 °C and 32 °C are similar, while the data at 33 °C are noticeably different. This should not be the case because 1 °C should not be significant enough to create such a drastic change. After 50 h, the results obtained from the CFD model at T = 29 °C and 33 °C matched reasonably well with the experiments at 30 °C and 32 °C.

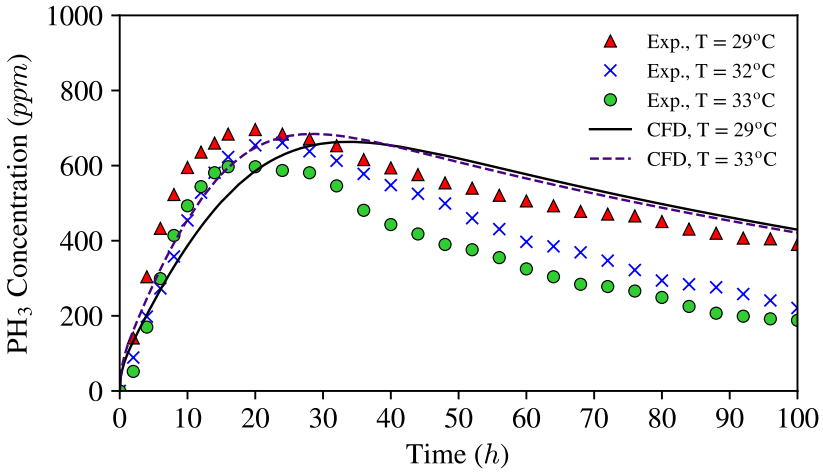

Figure 3.10: Comparison between CFD results (T = 29 °C —— and T = 33 °C - - -) and experimental data (T = 29 °C ▲, T = 32 °C ×, and T = 33 °C ●) for the half-filled case based on PH_3 concentration (ppm) versus time (h).

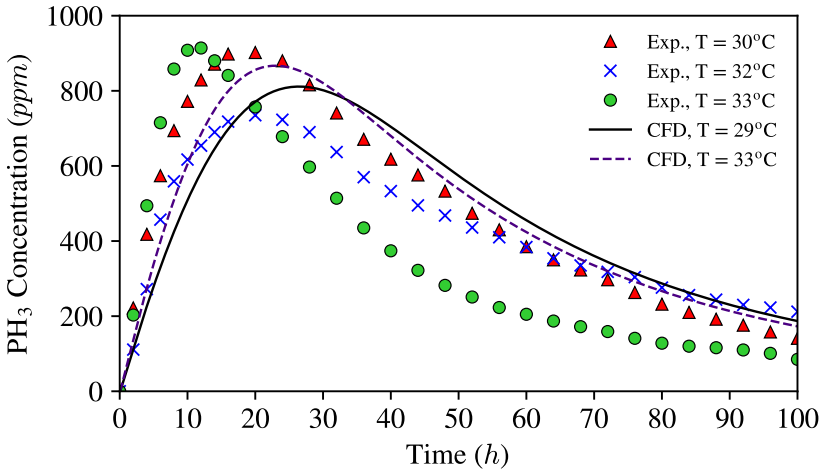

Figure 3.11: Comparison between CFD results (T = 29 °C —— and T = 33 °C - - -) and experimental data (T = 30 °C ▲, T = 32 °C ×, and T = 33 °C ●) for the full of wheat case based on PH_3 concentration (ppm) versus time (h).

Table 3.2 shows the percentage error for the two cases. The smallest error between the CFD results and the experimental data for the half-filled case was 0.9% with 0.3% for the

full of wheat case. The error increased as the deviation between the experimental replicates increased. This ensures the applicability of the evolution rate formula (Eq. 3.4) and sorption (Eq. 3.8) in a real-world situation.

Table 3.2: A quantitative comparison between results obtained from this study and work of Turek and Hron (2006).

Experiment T (°C)	Filling Volume	CFD (29 °C) Error %	CFD (30 °C) Error %
29		0.9	3.1
32	Half	23.7	26.4
33		43.7	46.8
30		0.6	0.3
32	Full	10.4	11.5
33		33.8	35.2

Figure 3.12 shows a comparison between the experimental data for the full of wheat and half-filled cases at $T = 32\,°C$. The results almost coincide, which was unexpected because it implies that the sorption rate was not affected by the amount of wheat. This reinforces the need for more robust experiments to minimize the number of factors that might affect the results, such as leakage, reaction of PH_3 with the barrel material, temperature fluctuations, and variation between pellets. Overall, the results showed a slightly faster PH_3 release from the experiments than predicted by the CFD models. This may be due to ignoring the effect of RH, which was assumed constant for all simulations and was not monitored during the experiments. In addition, the apparent PH_3 sorption rates were greater in the experiments than predicted by the CFD models, and this may be due to some sort of leakage, reaction of PH_3 with the barrel material, temperature fluctuations, or because a more accurate approximation of the effect of temperature on sorption is required rather than adjusting K_{bind} in Darby's (2008) equation (Eq. 3.7).

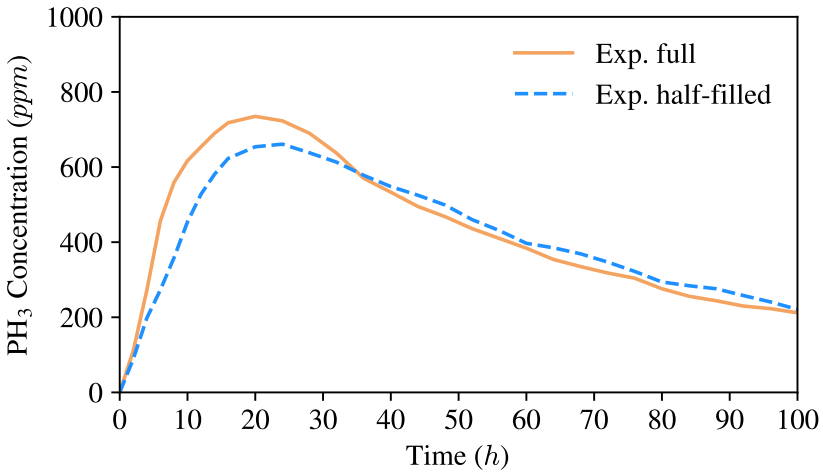

Figure 3.12: Comparison of the experimental data for the full (——) and half-filled (- - -) with wheat cases based on PH_3 concentration (ppm) versus time (h) at $T = 32\,^{\circ}C$.

Figure 3.13 shows the PH_3 concentration (ppm) contours for the three cases discussed in Sections 3.3.1 and 3.3.2 at 24 h. The highest concentration was at the pellet location at the bottom for the empty case and in the middle of the grain for the half-filled and full of wheat cases, and the concentration gradually decreased farther from the pellet.

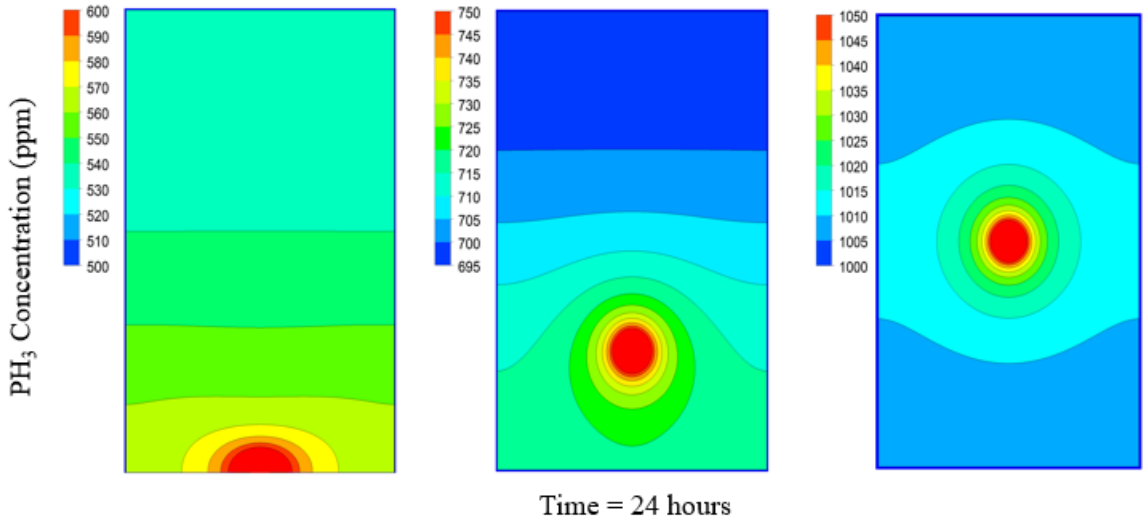

Figure 3.13: Contours of PH_3 concentration (ppm) at $T = 24$ h in each case: (a) empty (Sec. 3.3.1), (b) half-filled (Sec. 3.3.2), and (c) full of wheat (Sec. 3.3.2).

Chapter 4

Phosphine Movement in Bulk-stored Grain

4.1 Objective

The complete mechanisms of PH_3 movement in grain bunkers are difficult or impossible to observe and measure experimentally, but a validated CFD model can reveal those important aspects. The objectives of this chapter were to (1) Develop a CFD model that can examine different physical configurations and important factors for PH_3 fumigation of bunkers, including: (a) the contribution of the convection currents to the motion of PH_3, (b) location of PH_3 releasing points, (c) bunker shape, (d) leakage, (e) sorption, (f) bunker orientation, (g) temperature fluctuation, and (h) PH_3 movement in three dimensions and (2) Validate the CFD model with published benchmarks on natural convection in porous media and experimental data from a full-scale grain bin subject to natural convection, leakage, and PH_3 absorption into wheat.

4.2 CFD Models

The primary models developed were: (1) a 2D CFD model designed to study factors that affect the PH_3 distribution in bunkers: the location of the AlP tablets, different aspect ratios, bunker orientations, temperature fluctuations, leakage, and sorption and (2) a 3D case designed to study the PH_3 behavior in volumes instead of areas; the 3D model was implemented for a cylindrical grain bin and for a grain storage bunker. Two techniques were designed for validating these models; verification against published benchmarks and a comparison against experimental data of a full-scale grain bin. The same set of equations and techniques used for the bin model were used for the bunker simulations.

4.2.1 Validation

4.2.1.1 Benchmark validation

Validation and verification of the model was obtained by several comparisons to published benchmarks of similar configurations that deal with natural convection in a porous medium (Baytas and Pop, 1999; Bejan, 1979; Braga and de Lemos, 2004; Gross et al., 1986; Lauriat and Prasad, 1989). The domain shape in all benchmark cases was for a square domain filled with a porous medium. Structure mesh with 100 divisions on each side of the square was generated. The top and bottom walls were insulated. The left wall has higher constant temperature than the right wall. No-slip conditions are at all walls. Steady state flow and an incompressible fluid were assumed with no viscous heating. The fluid and the porous structure were assumed to be in a thermal equilibrium with constant porosity. The quantity of interest was the average Nusselt number ($\overline{Nu}$) at the hot wall (at $x = 0$ and $y = 0 \rightarrow H$) and it is defined as

$$\overline{Nu} = \int_0^H Nu|_{x=0}\, dy \tag{4.1}$$

Darcy number, $Da = \frac{K}{H^2} = 10^{-7}$ was considered. Two different values of the modified

Rayleigh number (Ra_m) were chosen for the comparison: $Ra_m = 10^2$ and $Ra_m = 10^3$. Ra_m is defined as

$$Ra_m = \frac{\rho g \beta \Delta T K H}{\mu \alpha} \tag{4.2}$$

Here, K (m^2) is the permeability, H (m) is the height of the porous domain, ρ ($kg\,m^{-3}$) is the fluid density, g ($m\,s^{-2}$) is the gravitational acceleration, β (K^{-1}) is the coefficient of the thermal expansion, ΔT (K) is the temperature difference between the hot and the cold ($\Delta T = T_h - T_c$), μ ($kg\,m^{-1}\,s^{-1}$) is the dynamic viscosity, and α ($m^2\,s^{-1}$) is the thermal diffusivity.

Table 4.1 shows the agreement between the published benchmarks and the current work. Figure 4.1 compares the isotherms, at $Ra_m = 1000$, with results of Baytas and Pop (1999). In this figure, the dimensionless temperature, θ, is $\frac{T(x,\ y) - T_f}{T_h - T_c}$. In which $T(x,\ y)$ is the temperature at any point in x and y, T_f is the film temperature, $\frac{T_h + T_c}{2}$, T_h is the temperature at the hot wall, and T_c is the temperature at the cold wall.

Table 4.1: Comparison of $\overline{Nu}$ with previous publications at two different ($Ra_m = 100$ and $Ra_m = 1000$), with $Da = 10^{-7}$ for laminar and steady state flow in a square domain filled with porous media.

Author	$\overline{Nu}$	
	$Ra_m = 100$	$Ra_m = 1000$
Bejan (1979)	4.20	15.80
Gross et al. (1986)	3.14	13.45
Lauriat and Prasad (1989)	3.08	13.35
Baytas and Pop (1999)	3.16	14.06
Braga and de Lemos (2004)	3.08	12.89
This study	3.11	13.55

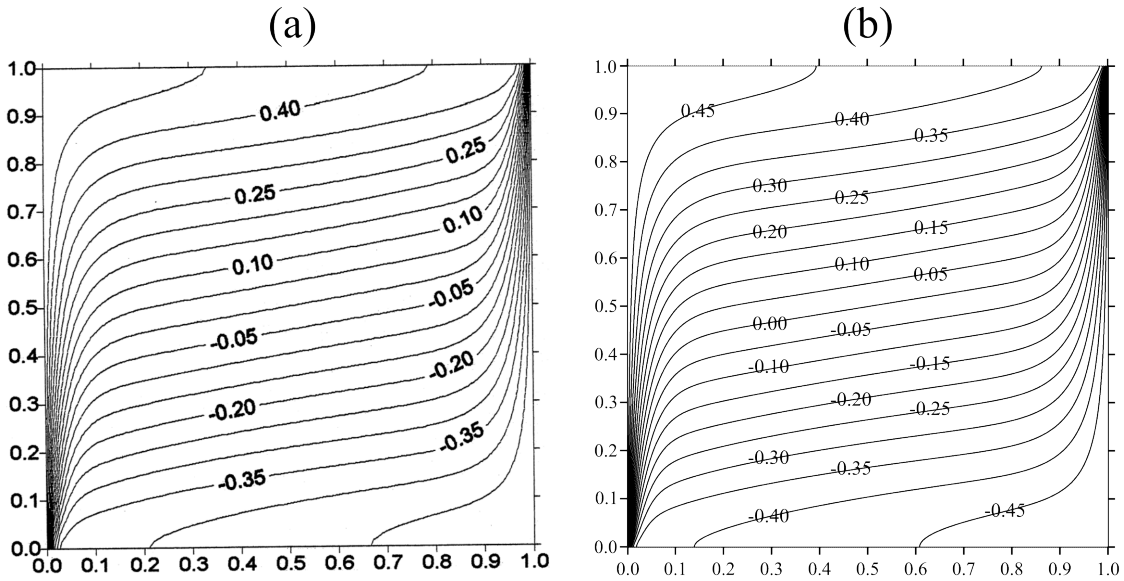

Figure 4.1: Isotherms from Baytas and Pop (1999) at Ra_m = 1000 (a), compared to results from this work (b).

4.2.1.2 Experimental validation

In this test, a CFD model of grain bin was built. The fluid (air + PH_3) in this bin was highly affected by the convection currents. Part of the bin, up to 3.6 m from the bottom, was filled with wheat while the rest is a headspace. The AlP tablets were applied at 27 locations distributed at three different heights (or grain depths). At each location 24 AlP tablets were placed i.e., 648 tablets total. The experimental bin had multiple leakage points distributed ununiformly at 4.2 m height with a very slight leakage from the duct on the bottom. These leakage points were visible to the naked eye from inside the bin during daylight. Figure 4.2 shows the domain with all details described. A mosaic (polyhedral and hexahedral) mesh with 285,520 elements was built as shown in Figure 4.3.

Figure 4.4 shows the wind speed and direction as well as the outside temperature during the time of the experiment. As seen, the magnitude of the velocity of the wind is highly variable, oscillating with time. From the wind rose on Figure 4.4, the wind direction is mostly coming from the south towards the north with dominant speed ranges from 2 $m\,s^{-1}$ to 6 $m\,s^{-1}$. As a result, the wind direction in the simulation was from the south. No-slip

velocity boundary condition was applied to all bin walls, except for the leakage points. Pressure outlets were assigned to all leakage points in the headspace while, velocity inlet boundary condition was assigned to the leakage from the bottom. The incoming velocity was considered as 10^{-6} of the freestream velocity in Figure 4.4 i.e., nearly zero leakage from the bottom. To consider the solar effect on the bin, the solar ray tracing algorithm of ANSYS Fluent was employed. In this algorithm the actual longitude, latitude, time zone, solar irradiant of where the bin is located were used. In addition to the solar effect, heat convection conditions were applied to all walls except a constant temperature was assigned to the bottom wall. The value of the heat transfer coefficient is needed for the heat convection boundary conditions at the bin wall.

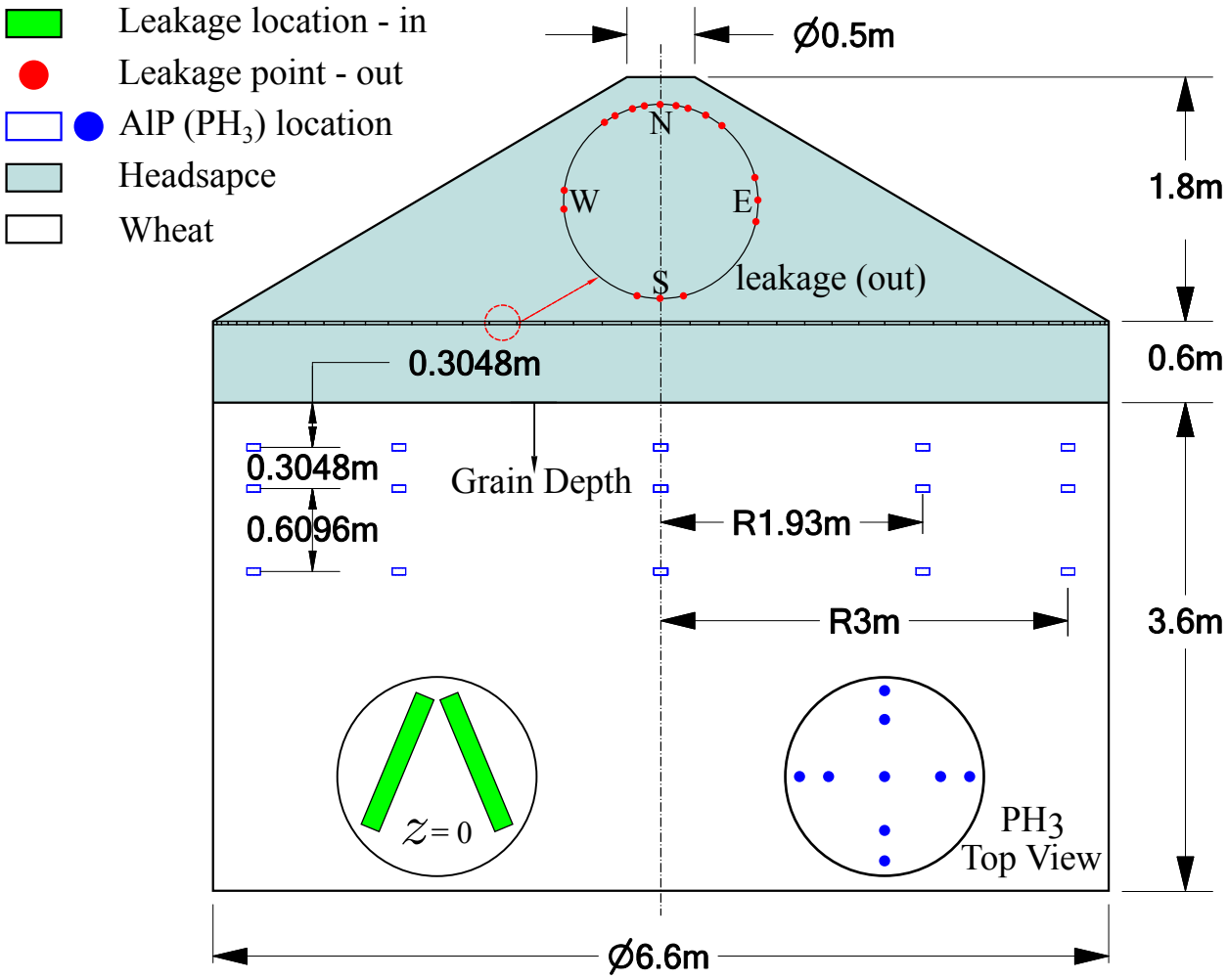

Figure 4.2: Computational domain of the bin with all details.

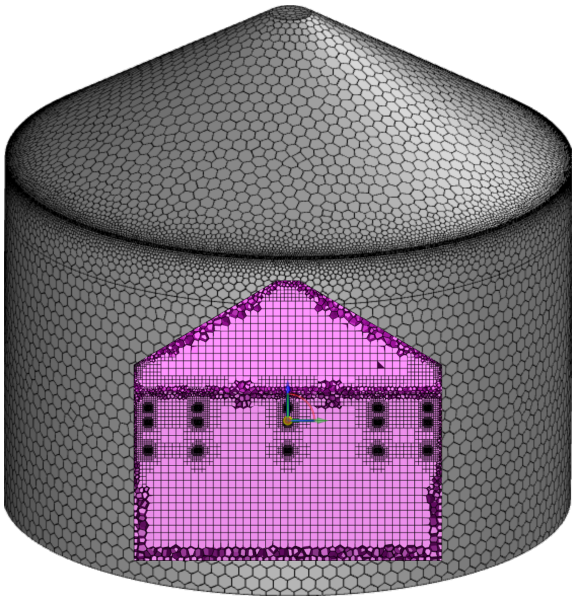

Figure 4.3: Mosaic (polyhedral and hexahedral) mesh for the bin simulation.

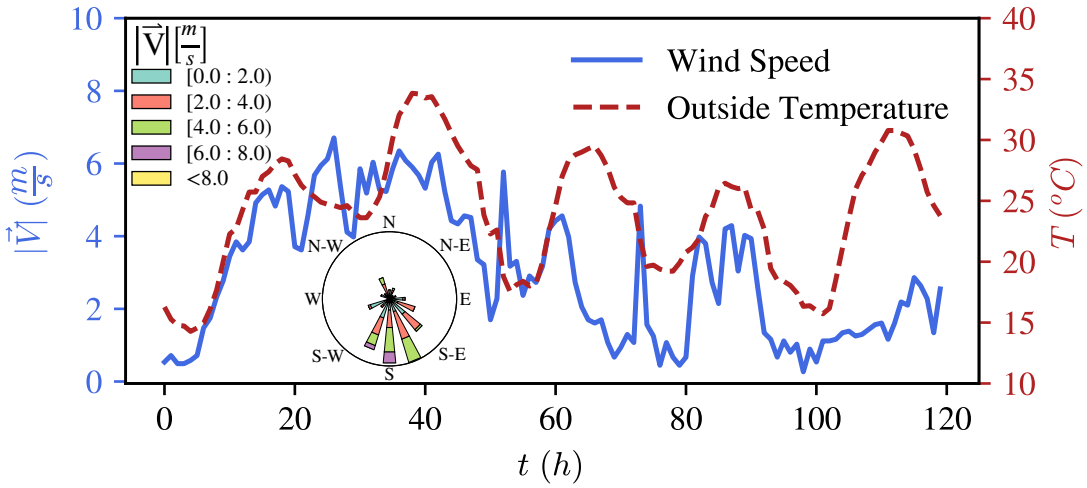

Figure 4.4: Free stream velocity ($\mathrm{m\,s^{-1}}$) (——) and temperature (°C) (- - -) along with the windrose at a location near the bin.

There are many available empirical correlations (Morgan, 1975) for the average heat transfer coefficient around a circular cylinder at different Reynolds numbers (Re). Most of them, if not all, are at low Re. For accurate results, the value of the local heat transfer coefficient needs to be determined. The local heat transfer coefficient varies along the bin wall surface. This variation is mainly caused by the wind speed, wind direction, and the

geometrical shape of the bin such as the bin diameter and the ratio of the length to the diameter. At the stagnation point, where the velocity is zero, the fluid will accelerate and decelerate based on the value of the pressure gradient along the bin circumference. At some point, boundary layer separation occurs, and the wake region is formed. As in Figure 4.4, the wind speed as well as the free stream temperature varies with time. To capture all these variabilities, a 3D transient external flow model with air velocity coming from the south was built. The purpose of this model is to generate the heat transfer coefficients as a function of position and time. Then these results were fed back to the main model of the bin as boundary conditions at each time-step. The effect of the atmospheric boundary layer, Eq. 4.3 of the turbulent boundary layer on a flat plate, was employed.

$$V(z) = |\vec{V}| \left(\frac{z}{H_{bin}} \right)^{\frac{1}{7}} \tag{4.3}$$

where $V(z)$ ($\mathrm{m\,s^{-1}}$) as the air velocity is a function of the vertical coordinate z (m), $|\vec{V}|$ is the freestream velocity ($\mathrm{m\,s^{-1}}$), and H_{bin} is the maximum height of the bin (6 m). Figure 4.5 shows a top view section of the heat transfer coefficient at $t = 120$ h obtained from the external flow model. It can show the effect of the wind direction coming from the south on the spatial variation of the heat transfer coefficient. It also shows the effect of Reynolds number when fluid separation occurs. Figure 4.6 shows a comparison between the average heat transfer coefficient as a function of time at all walls, including the truncated cone shape of the bin roof, and results from the empirical correlation of Žukauskas (1972), Eq. 4.6. Results from the correlation acts as an average for the CFD results, which shows that the model agrees well with the correlation and the Žukauskas's correlation for flow around circular cylinders was effective even though it does not involve the ratio of the length to the diameter of cylinders. The local heat transfer coefficient ($h = f(x,\ y,\ z,\ t)$), were generated at each time-step and was used for the main model of the bin.

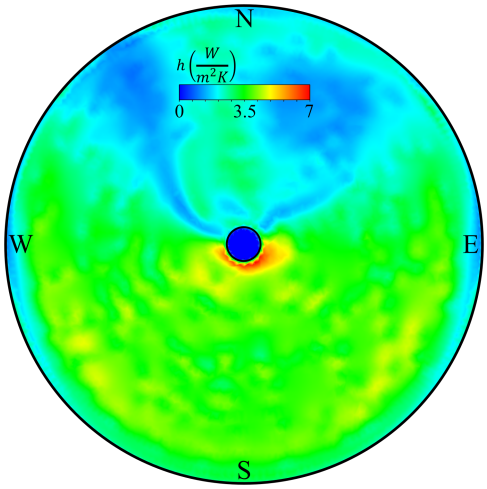

Figure 4.5: Local heat transfer coefficient ($\mathrm{W\,m^{-2}\,K^{-1}}$), top view, at 120 h resulted from the external flow model of the bin.

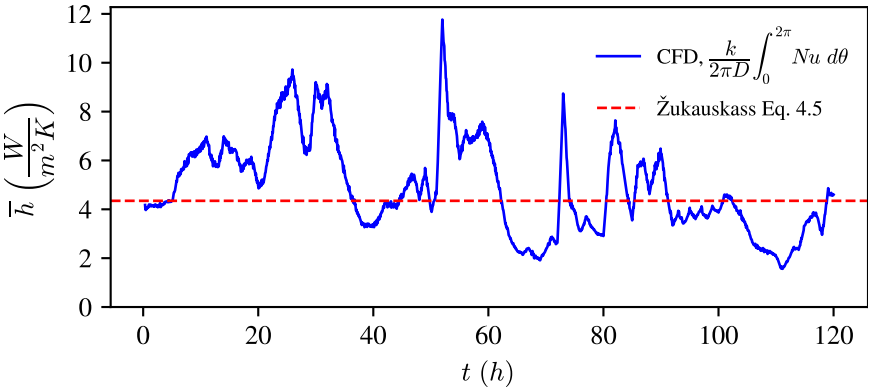

Figure 4.6: The average heat transfer coefficient ($\mathrm{W\,m^{-2}\,K^{-1}}$) from the CFD results (——) of the external flow model of the bin compared to results of the empirical correlation of Žukauskas (1972) (- - -).

Wheat was inside the bin for long periods before starting the experiment. So, natural convection currents were present at time zero of the experiment. To start with reasonable initial conditions for the main simulation, a 3D steady state internal flow model was built with no PH_3 involved. In this model, the solar effect and the heat convection boundary conditions based on the average heat transfer coefficient were employed as boundary conditions. Reynolds number based on the bin diameter (Re_D) is defined as

$$Re_D = \frac{\rho\,|\vec{V}|D}{\mu} \tag{4.4}$$

Here ρ is the air density ($\mathrm{kg\,m^{-3}}$), D is the bin diameter (m), and μ is the dynamic viscosity of the air ($\mathrm{kg\,m^{-1}\,s^{-1}}$). At the film temperature (the mean temperature of the average outside air temperature and the average temperature of the grain) and the average velocity, $Re = 1.05 \times 10^6$. The average Nusselt number is defined as

$$\overline{Nu} = \frac{1}{2\pi} \int_0^{2\pi} Nu \; d\theta = \frac{\overline{h} D}{k} \tag{4.5}$$

where, Nu is the local Nusselt number, $\overline{h}$ is the average heat transfer coefficient ($\mathrm{W\,m^{-2}\,K^{-1}}$), and k is the air thermal conductivity ($\mathrm{W\,m^{-1}\,K^{-1}}$). To obtain the average heat transfer coefficient, Žukauskas's (1972) was utilized. This correlation is valid for air at $1 \times 10^5 \leq Re \leq 1 \times 10^6$ and it takes the form

$$\overline{Nu} = 0.067 \; Re^{0.7} \tag{4.6}$$

In Eq. 4.5, the length to diameter, L/D, ratio is neglected. Substituting the value of $\overline{Nu}$ calculated at the average Re into Eq. 4.5, the average heat transfer coefficient was obtained. The diameter of the bin at 4.2 m height decreases up to the top point of the bin, 6 m. To consider the change in diameter, this relationship was used

$$D(z_o < z \leq H_{bin}) = D - \left(\frac{D - d}{H_{bin} - z_o} \right) (z - z_o) \tag{4.7}$$

Here d is the smallest diameter at H_{bin}, and z_o is where the change in diameter starts, at 4.2 m. The change in air properties with temperature was also considered. Air density was calculated from the equation of state. For both the dynamic viscosity (μ) and the thermal conductivity (k), Sutherland's formulas (White, 2006) were utilized as

$$\mu = \mu_o \left(\frac{T}{T_o} \right)^{1.5} \frac{T_o + S_\mu}{T + S_\mu} \tag{4.8}$$

$$k = k_o \left(\frac{T}{T_o} \right)^{1.5} \frac{T_o + S_k}{T + S_k} \tag{4.9}$$

Constants in Eq. 4.8 and Eq. 4.9 are $T_o = 273.11\mathrm{K}$, $\mu_o = 1.716 \times 10^{-5} \mathrm{kg\,m^{-1}\,s^{-1}}$, $S_\mu = 111\mathrm{K}$,

k_o = 0.0241W m^{-1} K^{-1}, and S_k = 194K.

The material properties of bin wall (Jia et al., 2000) are ρ_b = 7790 kg m^{-3}, k_b = 43.2 W m^{-1} K^{-1}, and the specific heat at a constant pressure, c_p = 470 J kg^{-1} K^{-1}. Figure 4.7 shows the results obtained from the steady state model; the contours of the temperature along with velocity vectors that describe the motion of the flow induced by natural convection. Since this is a steady state model, the actual change in the sun's position with respect to time was not considered; neither the wind speed, direction, nor temperature. It is meant to give some momentum, within a reasonable magnitude of velocity, to the air inside the bin at time zero.

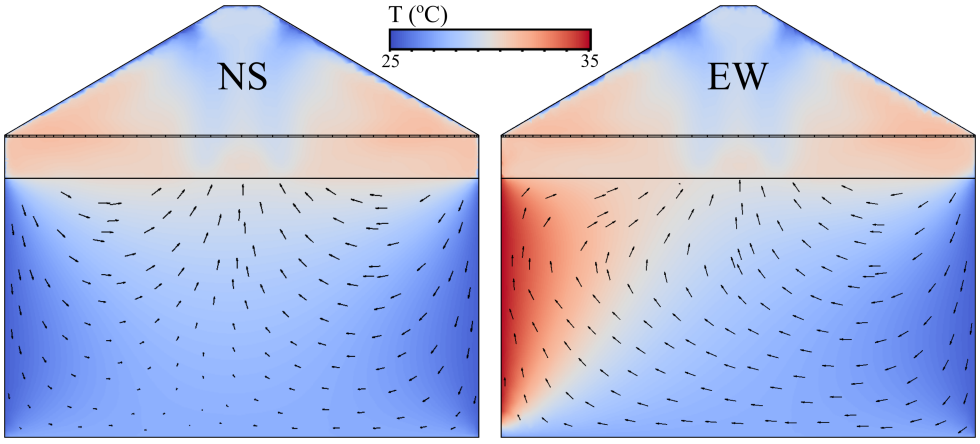

Figure 4.7: Temperature contours (°C) along with velocity vectors for the steady state model of the bin.

Information from the first two models; steady state internal flow and unsteady external flow, were used in the main CFD model of the bin. All sets of equations described in Chapter 2.3 were employed. The average concentration of PH_3 (ppm) at three different grain depths (0.4 m, 1.1 m, and 1.8 m) compared to the experimental data are shown in Figure 4.8. The comparison agreed well with the experiment specifically after the first 18 h. There is some disagreement in the beginning of the experiment. The reason behind this spike in concentration of the experiment was because the gas tubes' locations (at which PH_3 was sampled and measured) were near or at the AlP tablets' locations. Thus, the initial measured values were higher than the local average values in the simulation results.

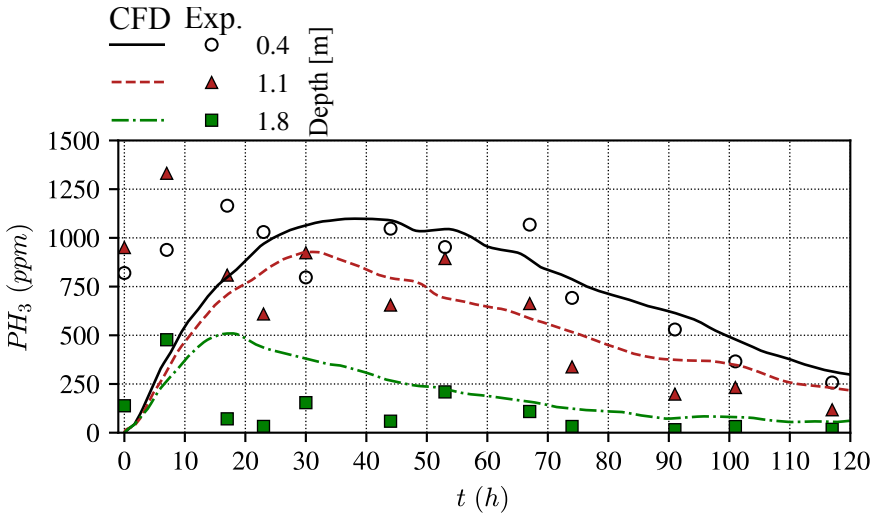

Figure 4.8: The average PH_3 concentration (ppm) between the CFD results of the main model at three different depths (0.4 m —, 1.1 m - - -, and 1.8 m -·-·) of the bin and the experimental data at the same three depths (0.4 m ○, 1.1 m ▲, and 1.8 m ■).

Figures 4.9 and 4.10 are PH_3 contours plots (ppm) at North-South (NS) and East-West (EW) at 24 h compared to contours plots of the closest experimental data in time at ~ 24h. These contours from the experiment were sampled at certain locations and interpolated at all other points. Results show the similarities between the CFD model and the experimental data. Because of gravity, both air and PH_3 should move towards the bottom of the bin if cooled. However, with the upward convection currents, they are being pushed up towards the headspace, where leakage points are located.

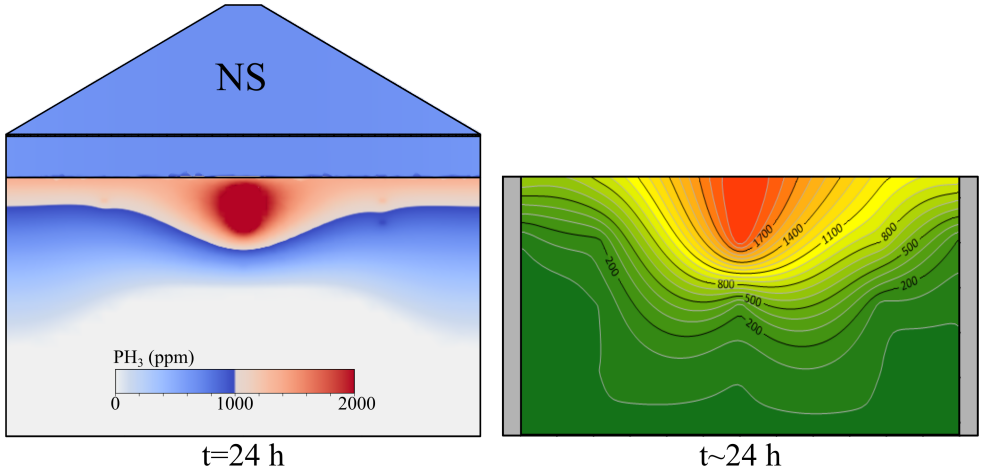

Figure 4.9: Contours plots at North-South section (NS) of PH_3 (ppm) from both the CFD results of the bin model (left) and the experimental data (right) at t = 24 h.

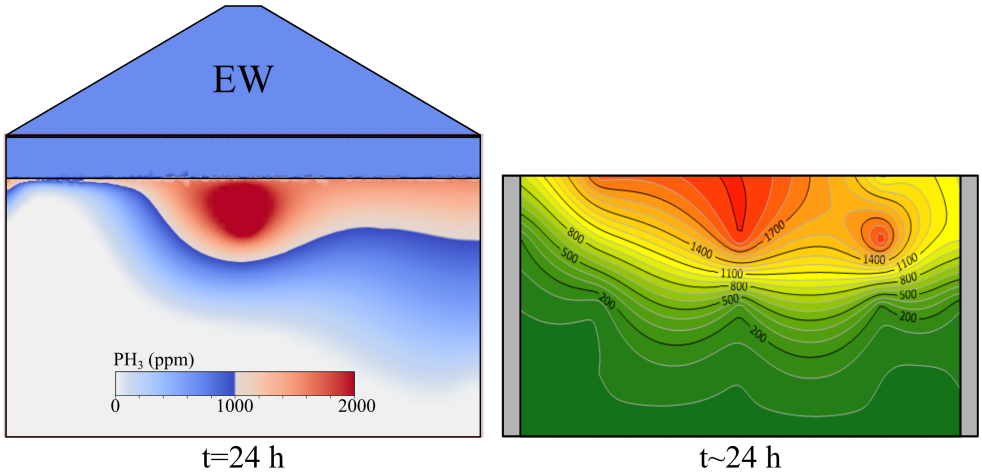

Figure 4.10: Contours plots at East-West section (EW) of PH_3 (ppm) from both the CFD results of the bin model (left) and the experimental data (right) at $t = 24\,\mathrm{h}$.

4.3 Bunker model

Figure 4.11 shows a typical 2D bunker shape. Because PH_3 fumigation of bunkers in Australia is a more frequent, critical task than in the U.S., a typical Australian bunker designs was used for the study rather than U.S. designs. In this Figure, dimensions are shown on the main model in which the AlP tablets (PH_3 release points) are located under the tarpaulin at the center of the half-left and the center of the half-right. In addition to this main scenario, three other locations are shown on the top right, illustrating the four different locations of PH_3 release that were investigated. In all cases, PH_3 was introduced at two locations, highlighted in green, with 102 AlP tablets at each location except for one case in which PH_3 was introduced only in the top middle of the bunker with 204 AlP tablets. This number of tablets is adequate to provide an application rate of $1.5\,\mathrm{g\,m^{-3}}$ (Daglish and Pavic, 2008). Figure 4.12 shows the computational domain with the general prescribed boundary and initial conditions. No-slip conditions are at all walls. The entire domain was assumed to be filled with a porous medium, to mimic the presence of wheat, that is in thermal equilibrium with the fluid (air + PH_3). In all cases unless otherwise specified, $T_H = 45\,^{\circ}\mathrm{C}$, $T_C = 35\,^{\circ}\mathrm{C}$. The steady state solution for the u (x–component of velocity), v (y–component of velocity),

p (pressure), and T (temperature) were taken as initial conditions for all transient simulations. Figure 4.13 shows the mesh with inflation layers, a very fine mesh along the walls that increases in size as it moves outwards, along all boundaries to capture the thermal, the velocity, and the concentration boundary layers.

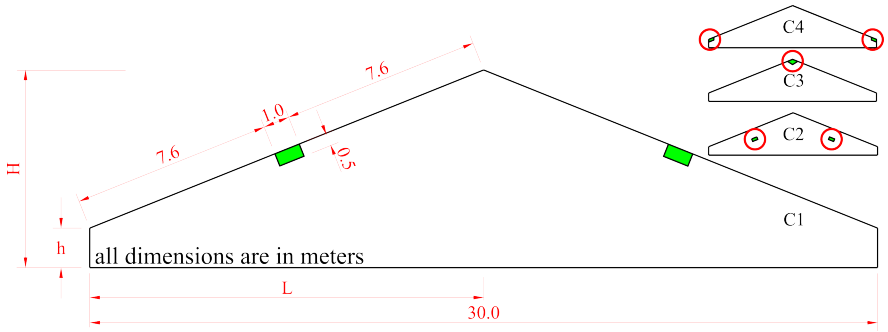

Figure 4.11: 2D bunker shape with the dimensions used for the simulation. The drawing indicates four different configurations (C1 – C4) for the PH_3 location; highlighted in green.

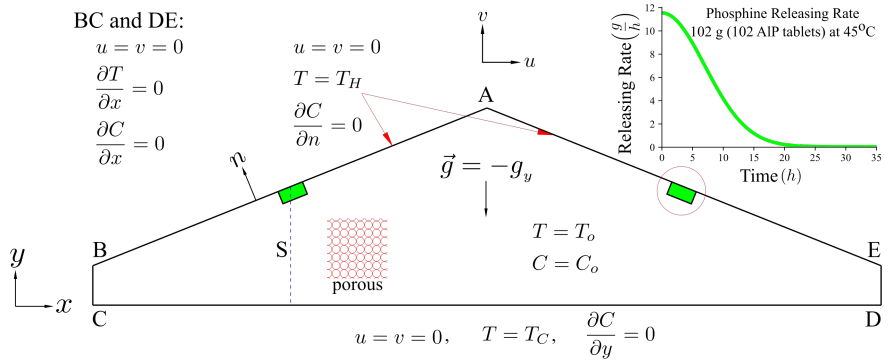

Figure 4.12: Boundary conditions used for the bunker simulation with the PH_3 evolution rate curve (—) of 102 AlP tablets at $T = 45\,°C$. Line S (- - -) is for the grid and time-step tests.

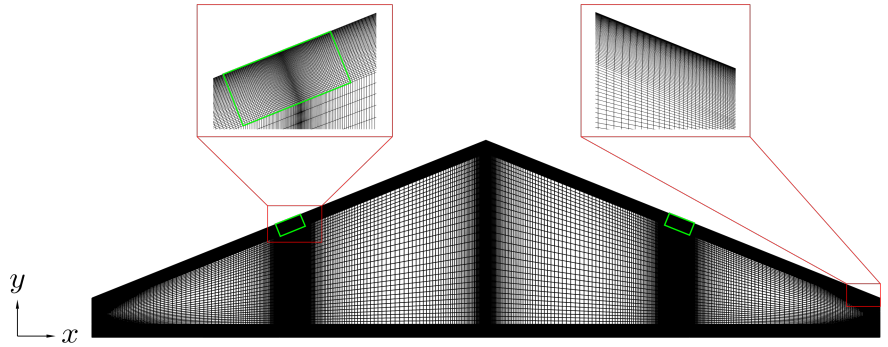

Figure 4.13: Structured mesh generated for the bunker simulation, zoomed-in at the left PH_3 location and the corner.

To find the optimum bunker size configuration that contributes to better PH_3 distribution, two different aspect ratio (AR) configurations were considered; the ratio of the maximum height of the bunker H to the half length of the bunker L (ARH) and the ratio of the side wall height h to L (ARh), as shown in Figure 4.11. The main AR in this study is ARH = 0.5 (H = 7.5 m and L = 15 m), and ARh = 0.1 (h = 1.5 m). Four different AR were compared to the main case of ARH = 0.5 and ARh = 0.1. Two of them are for the change in bunker height which is affected by the angle of repose of grain, ARH = 0.25 and ARH = 1.00. While the other two are for the effect of the side wall length, ARh = 0.05 and ARh = 0.20. In all scenarios with different aspect ratios, the number of the AlP tablets was calculated based on the new volume, i.e., the 1.5 g m^{-3} of PH_3 was maintained regardless of the change of volume.

To study how leakage may affect the PH_3 distribution and fumigation effectiveness as a result, six different leakage rates were investigated. The boundary conditions were assumed as a velocity inlet coming from the left and pressure outlet at the right, both with an area of 0.05 m^2. The six velocities are 0.0005, 0.001, 0.002, 0.003, 0.004, and 0.05 m s^{-1}.

Bunker orientation plays a rule on the convection currents inside bunkers. It may cause one side of the wall or part of it to become hotter than the other side. In addition to the main scenario, four different cases were considered, Table 4.2, named T_1, T_2, T_3, and T_4. The boundary conditions of case T_4 is a modified version of the one in Singh and Thorpe (1993), for when the outside temperature is colder than the inside.

The effect of temperature diurnal variation was studied. A sinusoidal function of temperature was assigned to the walls AB and AE shown in Figure 4.12. An additional case studied in which temperature fluctuations, leakage with velocity of 0.001 m s^{-1}, and sorption were combined in one model.

Motion in 3D gives more details on the flow mechanism, especially if the PH_3 releasing points are not continuous. In the 3D case, diurnal temperature variation, leakage and sorption were considered. Figure 4.14 shows the computational domain with dimensions. For leakage, four points at the left-side wall (x = 0 m) were assigned as inflow, and four points at the right-side wall (x = 30 m) were assigned as outflow. The magnitude of velocity was

computed to produce the same mass flow rate of the 2D case of $0.001\,\mathrm{m\,s^{-1}}$. A mesh with a combination of polyhedral and mostly hexahedral elements was built, as shown in Figure 4.15, also called a mosaic mesh, with 2,179,794 cells to ensure accurate results. Inflation layers were also considered at all walls to account for the boundary layers effects.

Table 4.2: Temperature boundary conditions for the effect of orientation scenarios.

Location	Wall ID*	Temperature Boundary Conditions (°C)			
		Case T_1	Case T_2	Case T_3	Case T_4
Top - Left	AB	40	40	40	20
Top - Right	AE	45	45	45	20
Side - Left	BC	40	$\frac{\partial T}{\partial x} = 0$	38	20
Side - Right	DE	45	$\frac{\partial T}{\partial x} = 0$	40	20
Bottom	CD	$\frac{\partial T}{\partial y} = 0$	35	35	35

*Wall IDs are shown in Figure 4.12.

For the 2D cases, ANSYS Design Modeler and ANSYS Mesh were used for geometry and mesh generation, respectively. For the 3D, ANSYS SpaceClaim and ANSYS Fluent were used for creating the geometry and mesh.

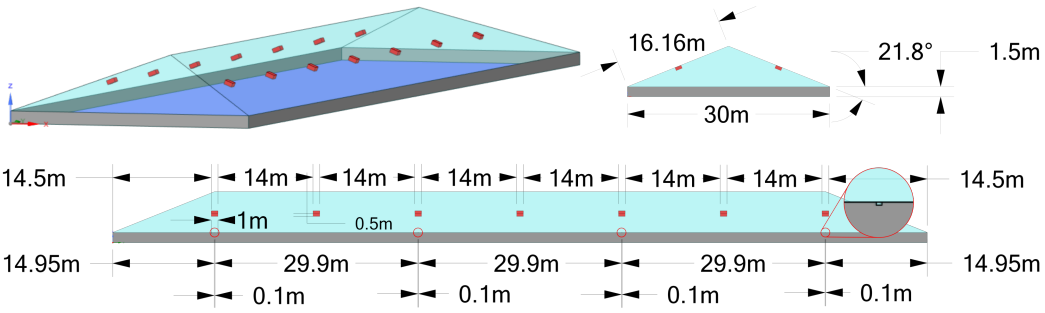

Figure 4.14: Computational domain along with the dimensions for the 3D bunker case.

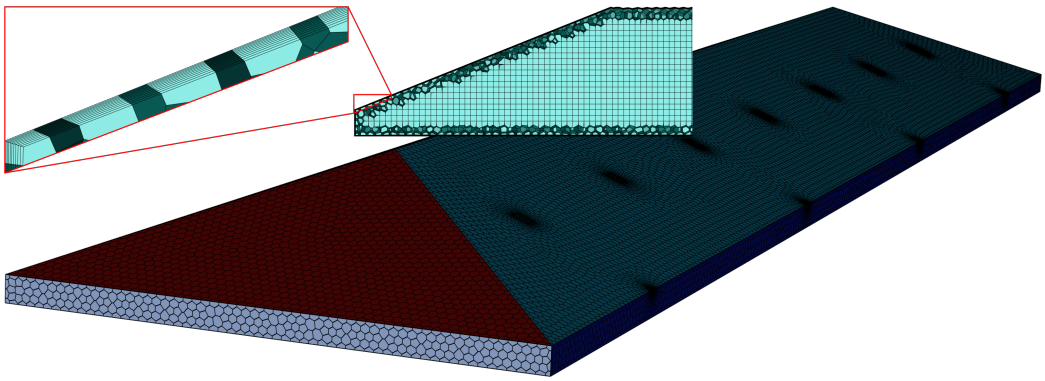

Figure 4.15: Mosaic (polyhedral and hexahedral) mesh for the 3D bunker simulation with inflation layers.

4.3.1 Grid refinement and time-step tests

A grid independency test was implemented to ensure that all results obtained do not vary with the mesh size. Three different mesh sizes were investigated; 178,920; 89,100; and 53,190 elements. All three mesh configurations had fine elements along the walls to capture boundary layer effects. The velocity magnitude along the segment S, shown in Figure 4.12, was used for comparison. As seen in Figure 4.16, the results do not deviate from the last two mesh sizes, so the medium mesh of 89,100 elements was chosen for all 2D simulations. The velocities at the top and bottom walls (no-slip) were excluded from the plot for better visualization.

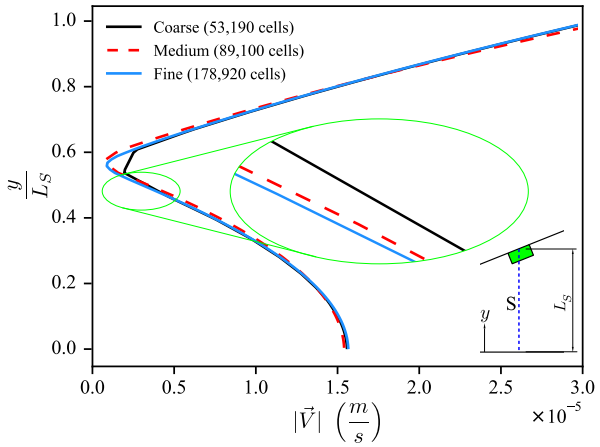

Figure 4.16: Velocity magnitude ($\mathrm{m\,s^{-1}}$) along segment S with three different mesh sizes (coarse —, medium - - -, fine —).

Another test was performed to make sure that the solution is independent of the time-step and that the chosen time-step is sufficient to capture the physics of the problem and for a stable solution. Three different time-steps were investigated, 1 s, 30 s, and 60 s. The PH_3 concentration along segment S at 24 h was the quantity of interest. As seen in Figure 4.17, the time-step of 60 s did not deviate from even the time-step of 1 s therefore, it was used in the simulations of this study.

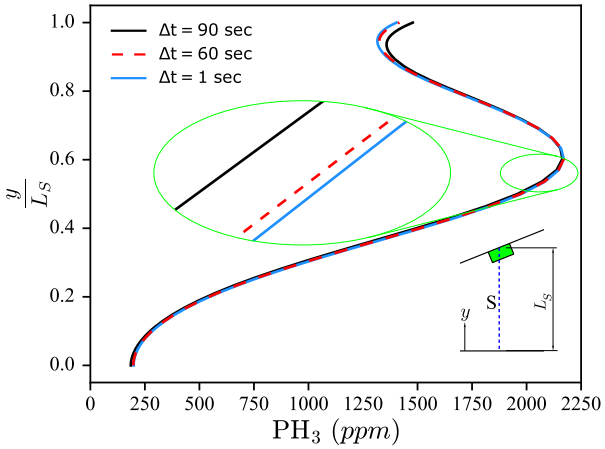

Figure 4.17: PH_3 concentration along segment S at 24 h with three different time-steps (90 s —, 60 s - - -, 1 s —).

4.3.2 CFD Results

The color of contours of PH_3 concentration in the figures follow the required dosage levels for effective treatment. For killing insects, 200 ppm – 300 ppm with an exposure time of 3 – 7 days is the recommended dosage (Wrigley et al., 2015). In all PH_3 contours (Figs. 4.20 – 4.22, 4.24, 4.26 – 4.30, 4.32, 4.33), anything that is not reddish in color is an area where the minimum 200ppm was not achieved and insects can survive. All cases were initialized with a steady state solution of temperature and velocity with no PH_3 involved, to generate natural convection currents. Many factors were studied; the effect of natural convection on PH_3 distribution, PH_3 releasing points, bunker shape, leakage, sorption, bunker orientation, ambient temperature fluctuation, and motion in 3D. Table 4.3 summarizes all cases studied for the bunker and indicates the relevant figure(s) for results of each factor investigated.

To distinguish between the contribution of each factor, a mortality fraction, η, concept

was developed. It is the ratio between the volume in which PH_3 concentration is greater than or equal to 200 ppm to the entire volume of the bunker, $\eta = \frac{V_{ppm \geq 200}}{V_{total}} \times 100$. This way if the entire bunker is occupied with the lethal concentration, the mortality fraction is 100%. Similarly, if the entire bunker has no PH_3 or PH_3 that is less than 200 ppm, the mortality fraction is 0%. This was written as conditioned expression for ANSYS Fluent as volume-weighted average of PH_3 concentration, $\frac{1}{V} \iiint PH_{3_{ppm}}\, dV$. All mortality fractions stated in this study are calculated at time = 48 h. The product of concentration and time of exposure, often called CT product, accounts for the combined effect of fumigant concentration and exposure time that is required for insect mortality at a given temperature (Phillips et al., 2012).

Table 4.3: Factors investigated by modeling studies.

Case*	Objective, study the effect of:	Results
Main(1)	Standard case for comparison	Figs. 4.18(b), 4.19, 4.20(c, d)
2	Natural convection (Rayleigh number/permeability)	Figs. 4.18(a), 4.18(c)
3	AlP tablet location	Figs. 4.21
4	Bunker aspect ratio	Figs. 4.22, 4.23
5	Side wall height	Figs. 4.24, 4.25
6	PH_3 leakage	Figs. 4.26
7	Bunker orientation	Figs. 4.27, 4.28
8	Diurnal variation	Figs. 4.29
9	Sorption of PH_3 by wheat	Figs. 4.30, 4.31
10	Combined diurnal variation, leakage, & sorption	Figs. 4.32
11	Combined diurnal variation, leakage, & sorption	Figs. 4.33

*All cases are in 2D with the exception of case 11 which is in 3D.

4.3.2.1 Standard case and effect of convection currents

It is important to see the effect of convection currents on the temperature inside the bunker. Ignoring the effect of radiation, temperature in bunkers is affected by both conduction and

convection. The convection contribution did not change the pattern of the isotherm, rather it increases the fluid temperature in the domain downwards in the direction of the gravity. Figure 4.18 shows three temperature contours for three different modified Rayleigh numbers, Ra_m = 0 (pure conduction), Ra_m = 100 (which is a reasonable value for bunkers), and Ra_m = 1000. Ra_m is affected by the permeability of wheat. As a result, the contribution of the convection is more pronounced as permeability increases.

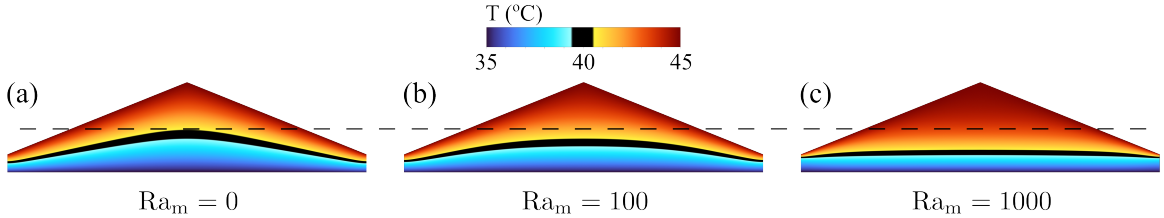

Figure 4.18: Temperature contours (°C) of the 2D bunker at three different modified Rayleigh numbers; (a) Ra_m = 0, (b) Ra_m = 100, and (c) Ra_m = 1000.

Figure 4.19 shows the velocity vector plot (a) and streamlines (b). The velocities are for the pore velocity not the superficial velocity (fluid velocity in absence of porous media). In the vector plot, there are three distinguished colors, red (around the top inclined walls), green (at the bottom wall), and blue (in the middle). While the velocity magnitude is very small, the red represents a higher velocity, the green medium velocity, and the blue for very low velocity. The contours of streamlines (b) show the air circulations inside the bunker. From both plots, the PH_3 concentration is expected to move towards the top center of the bunker near the two inclined covering tarps.

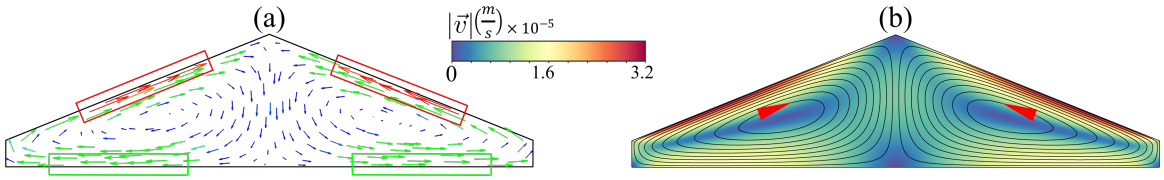

Figure 4.19: Plots of the velocity vector ($m\,s^{-1}$) (a) and the streamlines (b).

To investigate the contribution of the convection currents on the PH_3 distribution, Figure 4.20 shows a comparison between pure diffusion (a, b), in which no convection was involved and when convection (c, d) was included. Contours are shown for two different times,

after one day (a, c) and after two days (b, d). With pure diffusion, PH_3 is concentrated in a circular shape (sphere if 3D) around the AlP tablets locations, where the tablets decompose when it meets the moisture in the air. With convection, PH_3 is better distributed even with low velocity currents. In Figure 4.20(d), the effect of the velocity vector and streamlines, in Figure 4.19, can be seen on the PH_3 behavior. In terms of mortality fraction defined above, the value resulted from the pure diffusion case at 48 h is 33.5% compared to 66.8% deduced from the conduction and convection case i.e., natural convection almost doubled the region of lethal concentration inside the bunker.

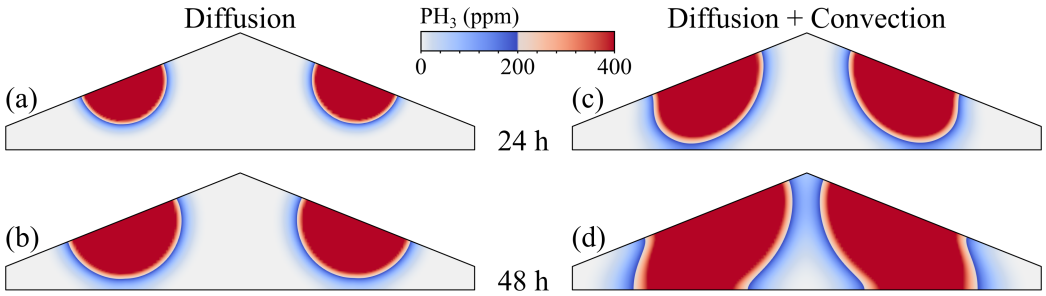

Figure 4.20: PH_3 concentration (ppm) for pure diffusion case (a, b) and diffusion + convection (c, d) at 24 h and 48 h.

4.3.2.2 Tablet location

The location of the PH_3 releasing points have a significant impact on the PH_3 distribution mechanism. Figure 4.21 shows contours plots of PH_3 (ppm) for three different locations; corner in which AlP tablets are placed near the two side walls of the bunker (a, d), middle in which the tablets were at one location in the center of the bunker (b, e), and in grain in which the tablets were located at some depth within the grain (c, f). This is in addition to the main scenario shown in Figure 4.20 (c, d). All contours are at 24 h (a, b, c) and 48 h (d, e, f). Because of the geometrical shape of the bunker and due to gravity, PH_3 tends to spread out towards the two ends of the bunker. Also, in Figure 4.19(a) velocities are higher somewhere in the middle of each side towards the center of the bunker, away from the corner. Similarly, because of the flow pattern, both the corner and middle cases provided the worst distribution of PH_3. While the in grain case (c, f) showed better distribution

similar to the main scenario of Figure 4.20(c, d). However, the main scenario provided the best distribution of PH_3 as it benefited from the convection currents. In terms of mortality fraction, the highest value was for the original case of Figure 4.20(c, d) with 66.8% compared to 60.4% for the "in grain", 29.8% for the "middle", and the lowest is for the "corner" with 23.0%. From the results, it is recommended that the AlP tablets be placed in the center of each side of the bunker either directly under the tarp or inside the grain to avoid PH_3 loss due to leakage, if any.

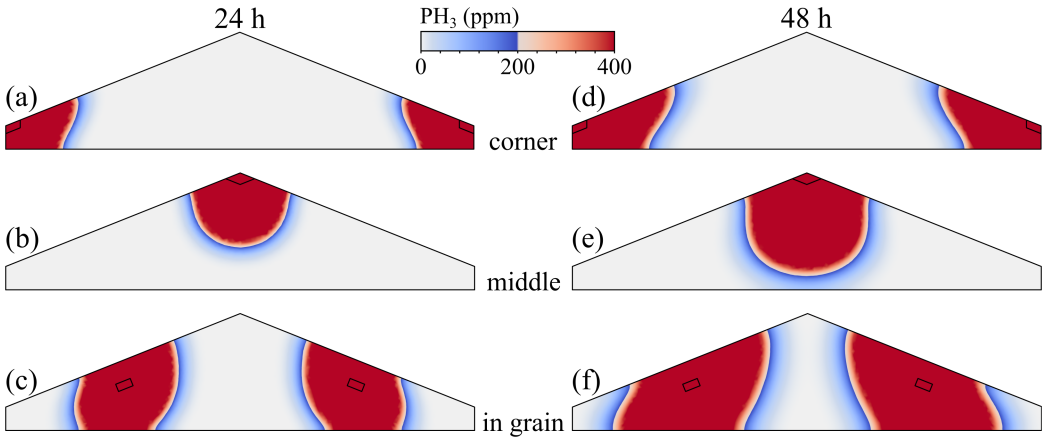

Figure 4.21: PH_3 concentration (ppm) at three different locations of the AlP tablets at 24 h (a, b, c) and 48 h (d, e, f).

4.3.2.3 Aspect ratio

If a grain storage facility has a rectangle shape and its top surface has a higher temperature than the bottom wall, no natural convection occurs without sidewall heating. The bunker shape slightly contributes to generating some convection currents. Also, in all cases, the convection currents are significant near the top surfaces. The angle of the inclined surface of the bunker is formed by the angle of repose of grain. In addition to the main case, Figure 4.20(c, d), in which there is an ARH of 0.50, two different aspect ratios in terms of the maximum height of the bunker were studied, shown in Figure 4.22: ARH = 1.00 (a, c) and ARH = 0.25 (b, d). The ARH of 1.00 more extreme than occurs with bulk grain, since it is limited by the grain angle of repose. However, this ARH is included to give an insight on how this angle affects the PH_3 movement. Visualizing the PH_3 concentration in

Figures 4.20(c, d) and 4.22, an ARH of 0.50 promotes better distribution of PH_3. Plotting the magnitude of velocity at segment S (Figure 4.12) at different ARHs, Figure 4.23, the ARH of 0.25 has the lower values of velocity i.e., worst PH_3 distribution. This is because the shape is approaching a rectangle. In contrast the velocity magnitude barely deviated when the ARH was doubled from 0.50 to 1.00. This also indicates the ARH of or near 0.50 is sufficient for good PH_3 distribution inside bunkers. The mortality fraction in the case of ARH = 0.25 is 58.6% compared to 38.4% for the case of ARH = 1.00 while the highest value is for the original scenario of ARH = 0.5 is 66.8%.

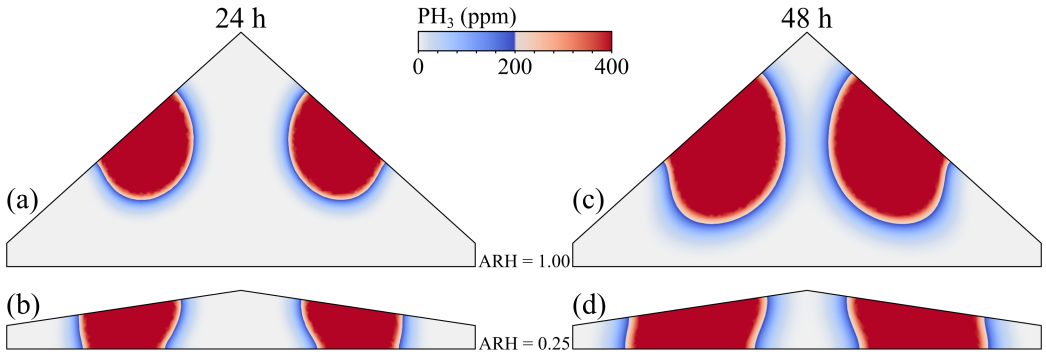

Figure 4.22: PH_3 concentration (ppm) for the case with ARH = 1.00 (a, c) and ARH = 0.25 (b, d) at 24 h (a, b) and 48 h (c, d).

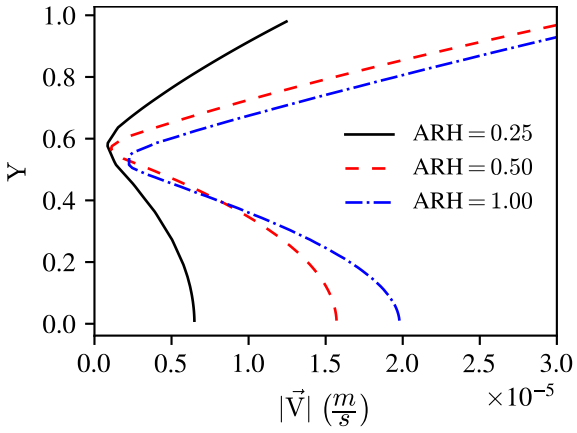

Figure 4.23: Velocity magnitude ($m\,s^{-1}$) at segment S for the three different ARHs (0.25 ——, 0.50 - - -, 1.00 -·-·-).

4.3.2.4 Side wall height

The effect of the side wall height was also studied through the aspect ratio of the bunker half-length (L) to the side wall height (h), ARh, indicated on Figure 4.11. Two different ARhs in addition to the main case of ARH of 0.50 or ARh of 0.10, are ARh = 0.05 and ARh = 0.20. Figure 4.24 shows the contours plots of PH_3 concentration (ppm) for these two cases, (b, d) for ARh = 0.05 and (a, c) for ARh = 0.20. The case of ARh = 0.10 is shown in Figure 4.20(c, d). From Figure 4.25, the velocity magnitude at segment S, the lowest velocity is for ARh = 0.20. The same concepts apply, when the shape is getting closer to a rectangular shape, it tends to reduce the strength of the convection currents. The velocity magnitudes from the three cases are close and are nearly identical between the case of ARh = 0.05 and ARh = 0.10 (the main model). The highest value of mortality fraction is still for the main scenario with 66.8% followed by 61.3% for the case of ARh = 0.20 and 60.1% for the case of ARh = 0.05. As a result, a bunker with aspect ratio, ARh, of 0.10 provided better PH_3 distribution. Based on the results, the side wall height of the bunkers seem to have less effect on the PH_3 distribution compared to the bunker aspect ratio (ARH).

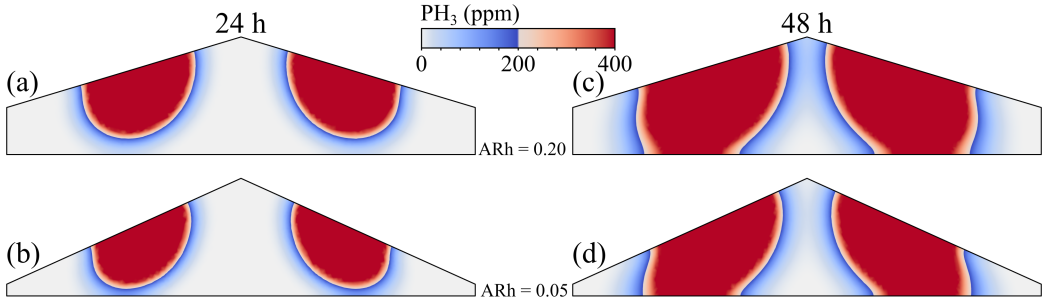

Figure 4.24: PH_3 concentration (ppm) for the case with ARh = 0.20 (a, c) and ARh = 0.05 (b, d) at 24 h (a, b) and 48 h (c, d).

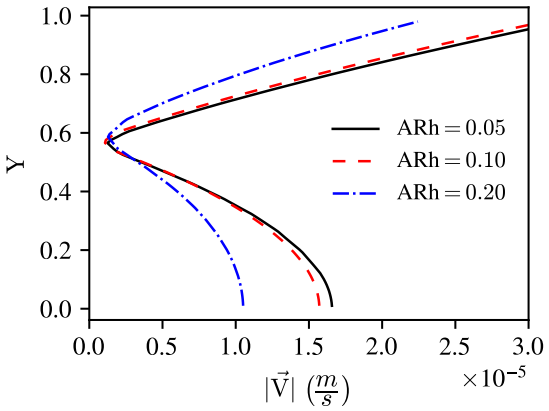

Figure 4.25: Velocity magnitude ($\mathrm{m\,s^{-1}}$) at segment S for the three different ARhs (0.05 ——, 0.10 - - -, 0.20 -·-·-).

4.3.2.5 Leakage

Leakages in bunkers are unavoidable and generally uncontrolled, with unknown amounts of leakage. Six different leakage scenarios were studied with a velocity inlet from the left side ($0.05\,\mathrm{m^2}$ out of the area of the side wall, $A_{side\ wall}$ = $1.5\,\mathrm{m^2}$) and a pressure outlet from the right side ($0.05\,\mathrm{m^2}$). The chosen values of velocity were 0.0005, 0.001, 0.002, 0.003, 0.004, and $0.005\,\mathrm{m\,s^{-1}}$. These velocity values were used to gradually increase the leakage rate. The pressure outlet boundary condition does not mean fluid must exit from that area, rather it depends on the pressure gradient between the outside (atmospheric) and the inside of the domain. Some air may enter from part of that assigned area. Figure 4.26 shows the contours of PH_3 (ppm) for all these scenarios. In each plot the value of the mortality fraction is indicated. Even with a small leakage of $0.0005\,\mathrm{m\,s^{-1}}$ the mortality fraction was reduced from 66.8% to 57.7%. From the contours, the PH_3 distribution changes as the leakage rate increases. However, no specific trend was observed between the mortality fraction and the increase in velocity. At small velocities ranging from $0.0005\,\mathrm{m\,s^{-1}}$ to $0.003\,\mathrm{m\,s^{-1}}$, the mortality fraction decreased linearly with the increase of velocity. Starting from $0.003\,\mathrm{m\,s^{-1}}$ to $0.005\,\mathrm{m\,s^{-1}}$, the value of mortality fraction remained almost unchanged. This is because fluid re-circulation occurs around the outlets with higher velocity values.

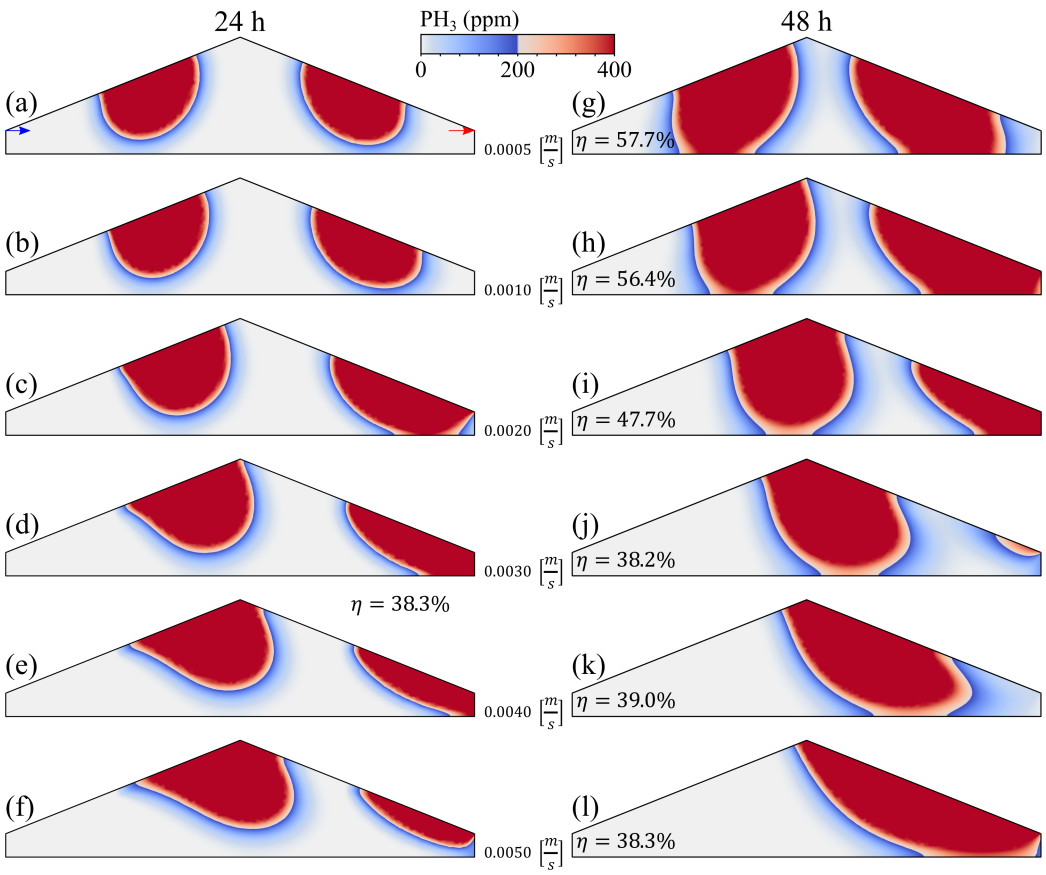

Figure 4.26: PH_3 concentration (ppm) resulted from different leakage rates at two 24 h (a – f) and 24 h (g – l).

4.3.2.6 Bunker orientation

Based on bunker orientation, some or part of the surfaces may get heated more than the others because of solar radiation. There is no standard for orientation of bunkers and many scenarios could occur in the field. There are three different cases, T_1, T_2, and T_3, described in Table 4.2. Figure 4.27 shows the contours of temperature (a, b, c) and PH_3 concentration (d, e, f). Comparing results of (a) and (d) to the main scenario of Figure 4.18(b) of temperature and Figure 4.20(c, d) for PH_3 concentration, the effect of different orientations can be seen on the PH_3 distribution. There were no significant changes in the results of cases T_2 and T_3. This implies that the temperature of the side wall has minor or no effect on the isotherm and PH_3 as a result. In the T_4 case, shown in Figure 4.28 (velocity, temperature, and PH_3

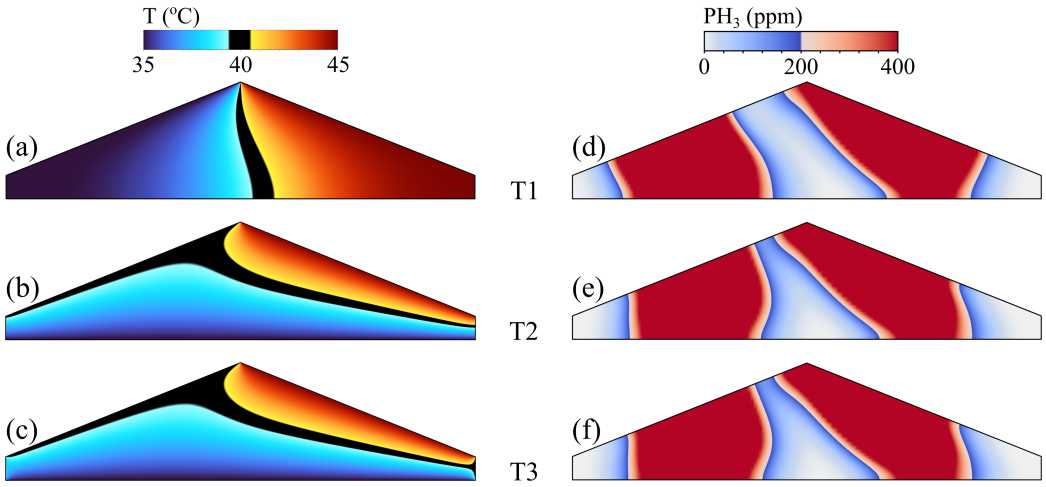

Figure 4.27: Contours of temperature (°C) (a, b, c) and PH_3 concentration (ppm) (d, e, f) illustrating the effect of bunker orientation for three different cases, T_1, T_2, and T_3 detailed in Table 4.2.

contours), since the top surface was at a lower temperature than the grain and the lower surface, convection currents had higher intensity, Figure 4.28(a), and different flow patterns. However, this was not sufficient to circulate the PH_3 everywhere in the bunker. PH_3 in this case is circulating around the sides leaving the center of the bunker with low or no PH_3. The mortality fraction in this case is 62.0% compared to 66.8% in the main scenario.

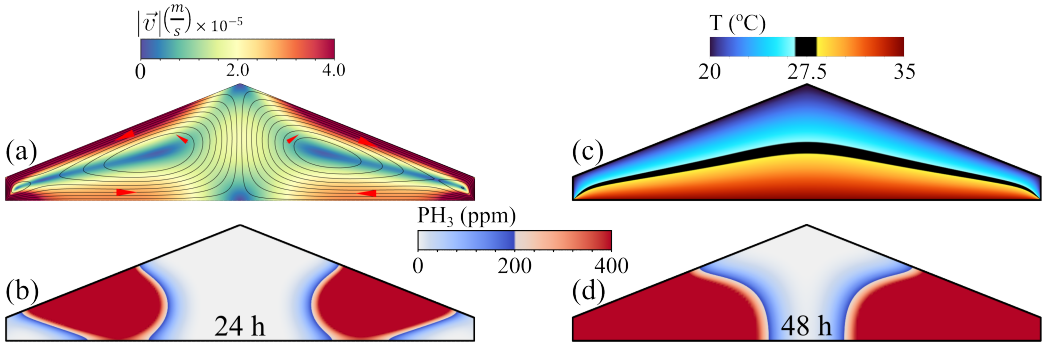

Figure 4.28: Contours of velocity ($m\,s^{-1}$) and streamlines (a), temperature (°C) (c), PH_3 concentration (ppm) at 24 h and 48 h (b, d) for the T_4 scenario.

4.3.2.7 Diurnal temperature variation

Ambient temperature fluctuation between day and night was described with a sinusoidal function with 24 h period. The velocity vector along with the streamlines in Figure 4.29(a)

show different patterns than the original case of Figure 4.19(b) at 48 h, created more circulation patterns in the central areas on each side of the bunker. The PH_3 is then restricted within those areas rather than being mixed around as seen in Figure 4.29(b, d). As for the isotherm in (c), it is divided into three vertical temperature regions with lower temperatures at layers near the top walls. This also resulted in weaker convection currents compared to Figure 4.20(c, d). The mortality fraction calculated at 48 h is 54.5% compared to 66.8% of the main case.

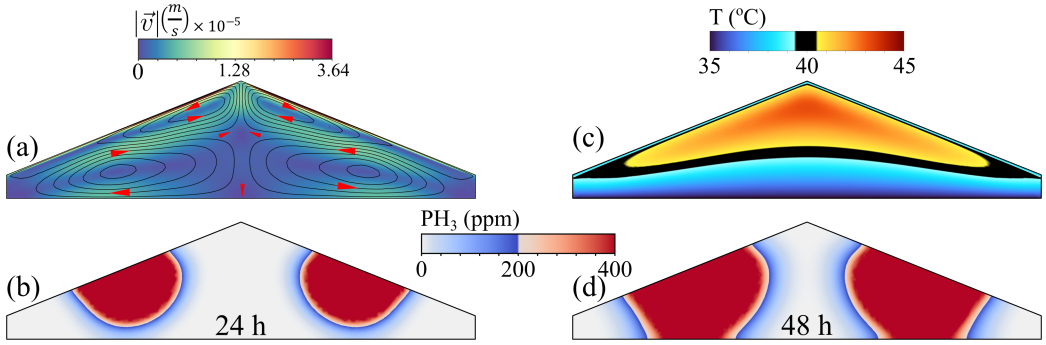

Figure 4.29: The effect of temperature fluctuation; (a) contours of velocity ($m\,s^{-1}$) and streamlines, (c) temperature (°C), (b and d) PH_3 concentration (ppm) at 24 h and 48 h, respectively.

4.3.2.8 Phosphine sorption

Wheat kernels absorb or desorb PH_3 to maintain equilibrium with the PH_3 level in the surrounding air as discussed in Chapter 3. Figure 4.30 shows the PH_3 contours at 24 h and 48 h. Comparing this to the main case of Figure 4.20(c, d), the distance $x_s = f(y_s)$, indicated on Figure 4.30(b), was reduced causing the mortality fraction to drop from 66.8% to 57.8% after 48 h. In these plots the red color is for 400 ppm or more. So, PH_3 concentration layers around x_s, without sorption, was less than 400 ppm. Those layers vanished because of PH_3 absorption. Sorption impacted the concentration in the entire domain but could not drop the values greater than 400 ppm to less than 200 ppm. If a bunker or a certain area of a bunker has exactly 400 ppm, how long does it take to get a concentration of 200 ppm or less i.e., below the lethal level? To answer this question, a separate case was run. In this case no AlP tablets were added as source terms to the governing equations, rather

the entire domain was initialized with mass fraction that is equivalent to exactly 400 ppm. Figure 4.31 shows the resulting loss in concentration with time. A bunker subjected to these conditions with an initial concentration of 400 ppm takes roughly two days to drop to 200 ppm. The change in concentration due to sorption is exponential, which matches the analytical solution of Darby's (2008) model (summation of two exponential functions, Eq. 3.10). It also implies that a simpler model similar to those of the first order kinetics (for example, Smith et al., 2001), $\frac{dC}{dt} = -k\ C(t)$, can be utilized to describe the effect of sorption. Here C is the concentration and k is the rate constant.

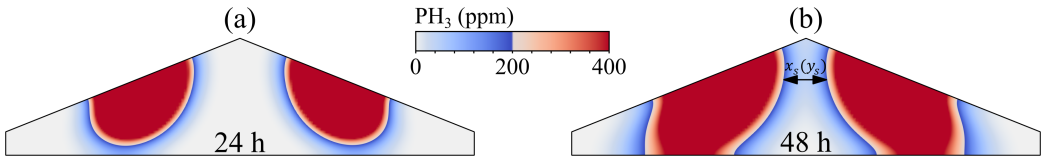

Figure 4.30: PH_3 contours (ppm) at 24 h (a) and 48 h (b) for the sorption case.

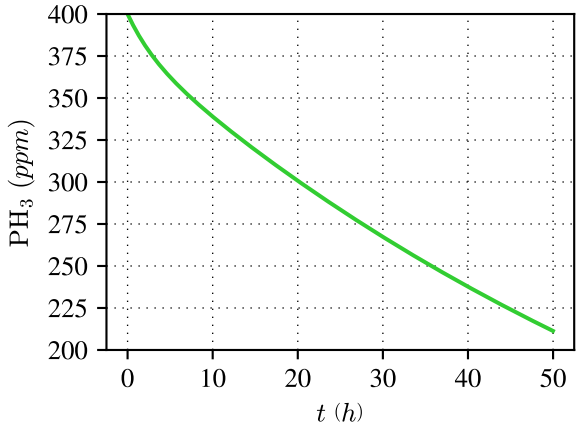

Figure 4.31: The exponential change in PH_3 (ppm) with time (h) due to absorption resulted from a hypothesis scenario of a 2D bunker that is initially at 400 ppm concentration everywhere in the domain with no AlP tablets in the governing equations.

4.3.2.9 Combined diurnal variation, leakage, & sorption

Adding the effect of sorption along with a leakage of 0.001 m s^{-1} and temperature fluctuation function, the mortality fraction drops to 47.2% versus 66.8% of the main case with no leakage nor sorption and a constant temperature. Figure 4.32 shows the resulted contours of PH_3.

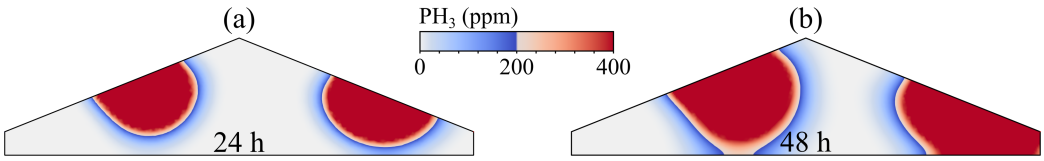

Figure 4.32: PH_3 contours (ppm) at 24 h (a) and 48 h (b) for a case with sorption, 0.001 m s^{-1} leakage, and sinusoidal temperature as boundary conditions.

A 3D model of the bunker was built. In this model the effects of sorption, leakage, and sinusoidal temperature variation were considered. In 2D, leakage locations and the AlP zones act as they are continuous along the entire length, 120 m in Figure 4.14. These are likely leakage scenarios based on the bunker construction but may or may not be the exact leakages in a specific scenario. In this 3D model specific locations were assumed for leakage and the number of AlP tablets trays were assumed to be distributed at 14 locations as shown in Figure 4.14. Figure 4.33 shows the PH_3 concentration (ppm) at different planes; (a) xy (horizontal axes) section at z = 1.5 m (vertical axis) i.e., at the same height of the side wall, (b) xz section at y = 60 m, (c) yz section at x = 15 m (the middle), and (d) is yz section at x = 7.5 m (cut through all AlP tablets). The leakage was set to produce an airflow rate that is equivalent to the 0.001 m s^{-1} of the 2D case. The case was picked as it produced an undesirable PH_3 distribution from all the 2D cases to represent a worst-case scenario. At z = 1.5 m (a), a velocity near zero and PH_3 at that height was derived mainly by diffusion in the direction of gravity. It also shows a better distribution could be obtained with more AlP locations. Based on the results, it is recommended to have the number of AlP spots equivalent to $\sim \frac{1}{8}$ of the longest side of bunker (in this study, the longest side is 120 m). That means, instead of 7 spots in each side of the bunker as of this case, 14 spots in each side is recommended. In (b), there is similar behavior as in the 2D cases. At a section in the exact middle of (b) along the entire bunker, PH_3 is around 50 ppm as shown in (c). Stronger leakages (or more leakage points for 2D) or different orientations would help move PH_3 towards the middle. In (d) as there are no convection currents in y direction, PH_3 was driven by diffusion.

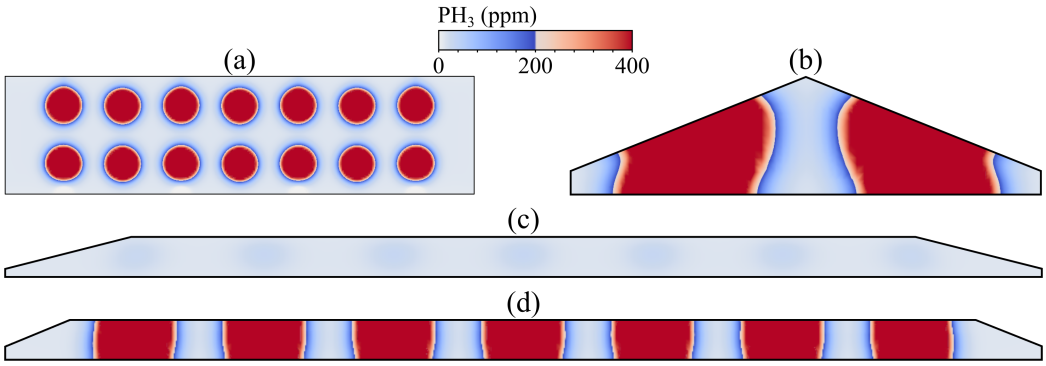

Figure 4.33: PH_3 concentration (ppm) for the 3D results; (a) top view at 1.5 m height (b) lateral side view at the center, (c) longitudinal side view in the middle, and (d) longitudinal side view that cuts through the PH_3 release points.

Chapter 5

Effect of Tarpaulin Billowing on Phosphine Behavior

5.1 Objective

The main objective of this chapter was to understand the PH_3 response to the tarpaulin motion induced by the inflow wind. This motion depends on numerous factors such as wind speed and direction, bunker orientation, the looseness of the tarpaulin (the volume of the headspace), the tightness of the tarpaulin with the side wall of the bunker, the level of crimps on the tarpaulin, the smoothness of the grain surface, the location and intensity of leakage, the grain angle of repose, and the overall shape of the bunker. Amongst those, many can be controlled such as the tightness or the smoothness of the surface while others cannot, such as wind speed and direction. The problem was divided into two main modeling techniques: (1) FSI on the bunker external body in which the response of both the fluid (outside wind) and the structure (tarpaulin) were considered through two distinct mathematical solvers with no wheat or PH_3 involved and (2) CFD with non-linear moving boundaries in which one fluid solver is utilized and the response of the fluid (air + PH_3) inside the bunker induced by the moving boundary is solved. Pure external CFD analysis was done first on three different orientations of the bunker in which one was chosen for the FSI analysis. Results from the

CFD internal flow were summarized into an artificial neural network model.

5.2 FSI - external flow

A Fluid-Structure-Interaction (FSI) simulations were built to study the effect of wind on the bunker tarpaulin. No experimental data are available for the specified problem. However, the validation and verification of the model was obtained by comparisons to published benchmarks (Glück et al., 2001; Turek and Hron, 2006).

The plastic cover of the bunker is very thin compared to its length and width and no compression could possibly occur in the direction of its thickness. Considering the thickness of the bunker cover explicitly in the geometry requires heavy unnecessary computations. Since no stress gradient across the thickness of the tarpaulin is expected, a shell element approach was adopted. In this approach, the thickness of the structure is not defined explicitly in the geometry, rather it was inferred in the calculations. Six degrees of freedom (DOFs) were allowed at each node; three translational and three rotational. Both membrane and bending behaviors are inherited in this approach i.e., the material can stretch, or bend based on the direction of the load. Although the thickness was explicitly defined in the two validation scenarios, the shell element technique was applied instead in this study and comparison made to the original cases (Glück et al., 2001; Turek and Hron, 2006). This was to make sure of the reliability of the method and settings applied to the bunker simulations.

Bunker cover is very thin and highly flexible so, it is subject to a significant impact and large deflection caused by the interacting wind. As a result, a two-way FSI approach was utilized, in which the interaction between the fluid and the solid takes place at the shared surface at each time-step and results are reflected and transferred by both participants at the interface. An implicit approach was employed for stability in which two distinct solvers were utilized along with a tool that communicates between them. In all FSI simulations in this study, ANSYS CFX 2021R1 was used as the CFD solver, ANSYS Mechanical 2021R1 was used as the structure solver, and ANSYS System Coupling 2021R1 was used to communicate between the two solvers. Forces calculated at the shared interface are supplied by the fluid

solver as loads to the structure solver. In turn, the incremental displacement, at the current time-step, is calculated by the structure model and is transferred back to the CFD solver with coupling iterations for each participant, fluid and solid, until results were converged. ANSYS CFX is based on the finite volume method while ANSYS Mechanical is based on the finite element method. The governing equations employed for both the fluid and the solid are available in the literature (e.g., Kumar et al., 2020; Lin et al., 2020).

5.2.1 Benchmark validation

5.2.1.1 Oscillating plate

The first validation problem is for a flexible plate in a fluid that is initially at rest (Glück et al., 2001). At time zero up to 0.5 s, the plate is subject to a pressure load of 100 Pa, then is released. The fluid is disturbed because of the plate motion and as time goes it forces the plate to come to a stop. The simulation is 3D with a domain thickness of 0.4 m in which symmetry boundary conditions were assigned at its lateral ends. All other boundaries, top, bottom, right, and left, were set as no-slip walls so, there is no inflow or outflow. Figure 5.1 shows the computational domain with dimensions along with the boundary and initial conditions. The properties of the solid and the fluid are also shown on Figure 5.1. The plate is located at the exact center of the domain with thickness of 60 mm. However, this thickness was not built in the geometry or the mesh, rather its effect was considered in the calculations, as discussed above in the thin structure technique. Figure 5.2 shows the hexahedral mesh generated for the entire domain and zoomed in around a segment of the plate. 35,000 cells were built for the fluid domain and only 640 were for the solid domain distributed uniformly on the lateral side of the plate. A time-step of 0.1 s was used with final simulation time of 25 s. The quantity of interest in this scenario was the x–displacement (in the horizontal axis) at point B, located at the top tip of the flexible plate as can be seen in Figure 5.1.

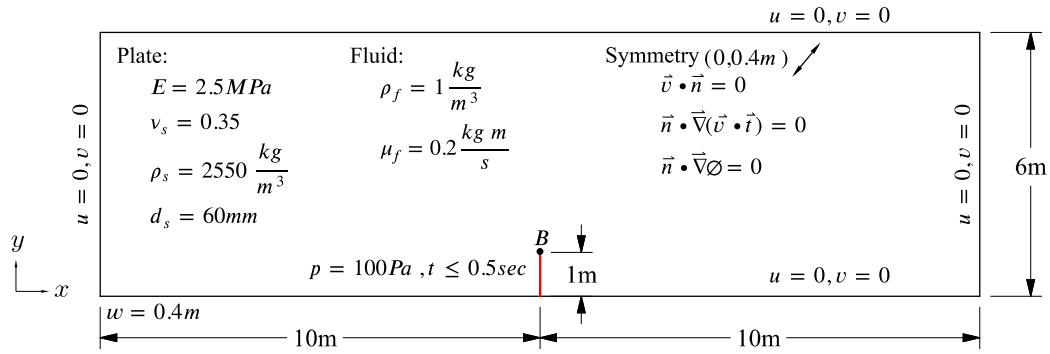

Figure 5.1: Computational domain along with the boundary and initial conditions for the oscillating plate case of Glück et al. (2001) used for validation.

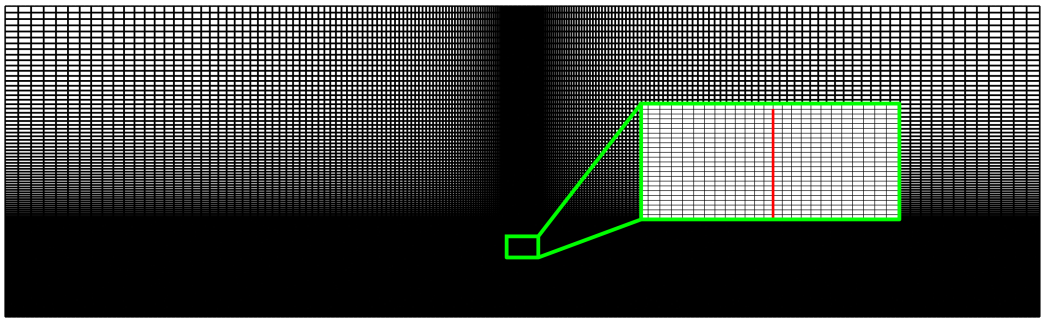

Figure 5.2: Structure mesh created for the oscillating plate problem with zoom-in around the flexible plate.

Results were compared to the numerical results of the original case (Glück et al., 2001) as well as the results of Namkoong et al. (2005). Figure 5.3 shows the obtained comparisons for the plate displacement at its tip (point B in Figure 5.1) in the x direction. In the first 10 s, results from this study, while it captured the exact motion, gives slightly higher amplitude then it matches almost identically with the original benchmark of Glück et al.. As seen in Figure 5.3, the current results with different approach (shell element) show better accuracy to the main benchmark other than the work of Namkoong et al.. The frequency of the x–displacement at point B was found to be identical to the value reported in Glück et al. (2001).

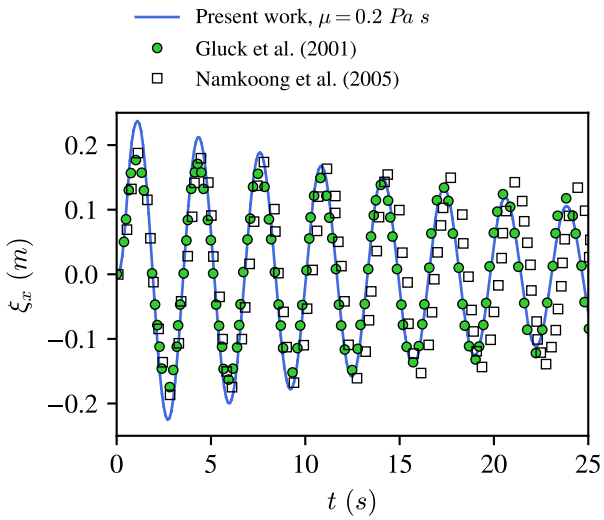

Figure 5.3: The change in the x–displacement (m) with time (s) at the tip of the flexible plate; a comparison between this study (—) against results of Glück et al. (2001) (●) and Namkoong et al. (2005) (□).

5.2.1.2 Flag

The second validation is for a flexible thin structure attached to a rigid cylinder (Turek and Hron, 2006). In this problem, the ratio of the fluid density to the density of the structure is relatively high with very large displacement of the thin solid structure in a highly viscous incompressible flow. As a result, this benchmark is numerically instable and subject to difficult conditions (Schildhauer and Spille-Kohoff, 2014). In Turek and Hron's work, the thickness of the solid structure was considered, while in this study the concept of thin structure, described above, was adopted instead.

Figure 5.4 shows the computational domain with dimensions, boundary and initial conditions, and both the fluid and solid properties. The problem was set up as a 3D geometry with a domain thickness of 0.5 m. The boundary conditions on both the lateral sides are symmetric while the top and bottom were set as no-slip walls. The inlet velocity is of the analytical solution of a fully developed flow in a channel. In the first two seconds of the simulation time, this velocity was smoothed out, as shown in the figure, to avoid numerical instabilities that may cause a high distortion of the structure and solution failure. As can be seen in Figure 5.4, the fluid is highly viscous and the structure is hyperplastic which

shares the same characteristics of the plastic cover used for grain bunkers, the tarpaulin. Figure 5.5 shows the structure mesh in the vicinity of the rigid cylinder and part of the connected flexible structure. The number of mesh elements in the fluid domain is 85,000 and 2000 cells were structured for the thin solid. Since the solid has no thickness, these elements were for the lateral side of the structure. A time-step of 0.01 s was set versus 0.001 s in the original benchmark (Turek and Hron, 2006). The final dimensionless time defined as $\frac{t\,\overline{U}}{D}$ is 150 in which t is the time (s), $\overline{U}$ is the mean velocity ($1\,\mathrm{m\,s^{-1}}$), and D is the diameter of the rigid cylinder (m). The quantity of interest in this case were the x–displacement and y–displacement at the flexible structure tip, the drag and lift coefficients at both the rigid cylinder and the flexible structure combined, and the frequency of the y–displacement at the tip of the non-rigid solid.

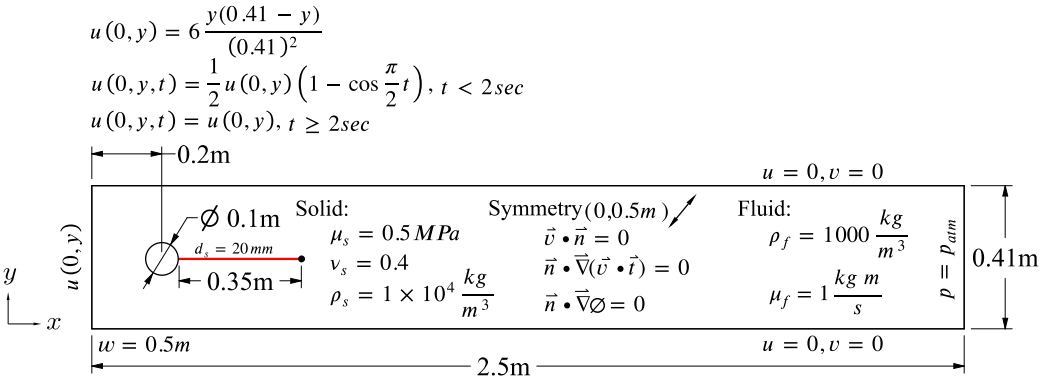

Figure 5.4: Computational domain, boundary and initial conditions, and fluid and solid properties used for the second validation scenario of Turek and Hron (2006).

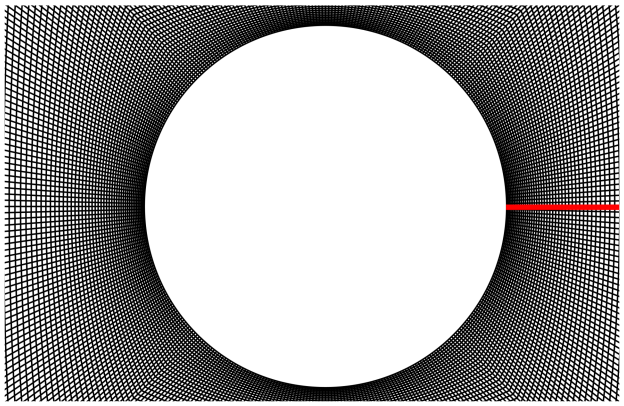

Figure 5.5: Hexahedral mesh generated in the vicinity of the cylinder and a segment of the flexible structure.

Although the time-step of the current work was chosen much coarser than the original benchmark, 0.01 s versus 0.001 s, the two results are in excellent agreement. This could be gained because of the shell element approach adopted for all FSI simulations in this study. Table 5.1 shows the concurred results obtained from the displacements in both the horizontal and the vertical directions at the free end point of the flexible plate as well as the combined forces on the rigid cylinder and the plate. Table 5.2 shows the frequencies of the displacements and forces obtained from this study and results of Turek and Hron. Figures 5.6 and 5.7 show a visualization of the two displacements (x and y) between the two results. There is a slight deviation in the magnitude of the x–displacement between the two results, Figure 5.7. This might be directly related to the fact that the thickness of the plate was not described in the geometry. Figure 5.8 shows the contours of the vorticity obtained from this study and how the motion of the structure affects the fluid behavior. The value of the drag coefficient, C_D, is closer to the original benchmark than other studies that reproduced the same simulation as a test case for the reliability of their code, with C_D = 4.03, from this study, compared to 4.13 from Turek and Hron versus 3.56 reported in Bhardwaj and Mittal (2012).

Table 5.1: A quantitative comparison between results obtained from this study and work of Turek and Hron (2006).

Variable	Turek and Hron (2006) Δt = 0.001 s	This Study Δt = 0.01 s
y–displacement (mm)	1.25±80.70	1.21±81.33
x–displacement (mm)	−14.58±12.37	−15.46±13.53
Drag Force (N)	201.29±67.61	201.27±65.80
Lift Force (N)	0.97±233.2	0.98±229.13

Table 5.2: Frequencies of the displacements and forces reported in Turek and Hron (2006) compared to values obtained from this study.

Variable	Frequency, f (Hz)	
	Turek and Hron (2006)	This Study
y–displacement	1.9-2.0	1.90
x–displacement	3.7-3.8	3.73
Drag Force	3.7-3.8	3.73
Lift Force	1.9-2.0	1.90

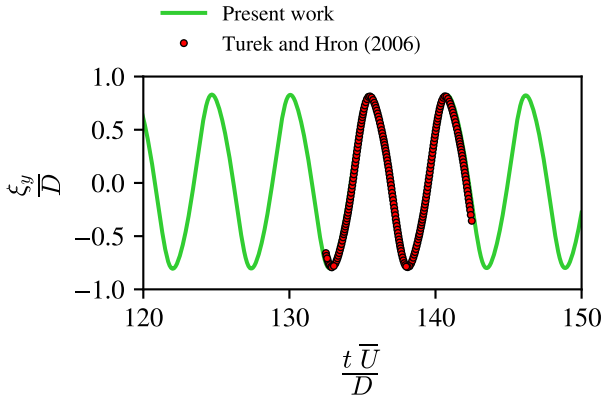

Figure 5.6: The dimensionless y–displacement ($\frac{\xi_y}{D}$) at the dimensionless time ($\frac{t\overline{U}}{D}$) between the current work (—) and results of Turek and Hron (2006) (●).

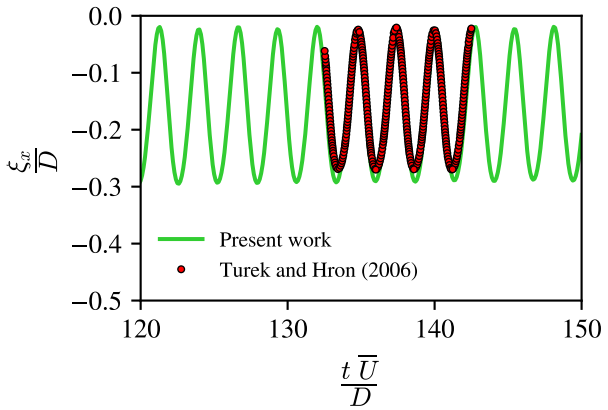

Figure 5.7: The dimensionless x–displacement ($\frac{\xi_x}{D}$) at the dimensionless time ($\frac{t\overline{U}}{D}$) between the current work (—) and results of Turek and Hron (2006) (●).

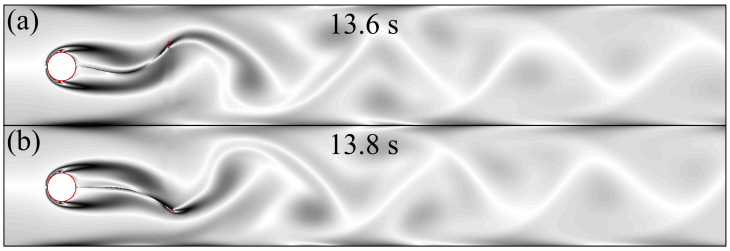

Figure 5.8: Vorticity contours obtained from this study at a dimensionless time of 13.6 s and 13.8 s show the fluid response to the motion of the flexible plate.

5.2.2 Bunker model

The FSI model was built on a 3D slice of the bunker. Forces acting on bunker surfaces depend on the direction of the wind or the orientation of the bunker. As a result, bunker covers may experience different pressure loads. To identify a case that is subject to the highest pressure loads on the surface, three CFD (no structure analysis is involved) cases were built. Based on results obtained from those three CFD analyses, a slice of the bunker was chosen for the FSI investigation.

5.2.2.1 Choosing a slice (CFD)

Three separate 3D-CFD simulations were built at three different Angle of Attack (AoA); 0°, 45°, 90°. Figure 5.9 shows the orientation of those scenarios. The height of a typical bunker is 7.5 m with 30 m width and 120 m length. The actual dimensions were considered with no scaling. A domain size was chosen in such a way that the flow is not affected by the boundaries (Singh and Roy, 2019). The domain height is $8H$ (H is the height of the bunker) with $5H$ upstream, $15H$ downstream, and $5H$ for the lateral sides. Since each case had different orientation, the overall domain size was also different. The mesh created was built to maintain the same cell size and quality in the three scenarios. Fine layers around the bunker walls were considered in the three models to capture the boundary layer effects. A mosaic mesh (polyhedral and hexahedral elements) was generated with 1,562,503 cells for the case of $AoA0°$, shown in Figure 5.10, 14,593,392 cells for $AoA45°$, and 9,058,475 cells for the $AoA90°$. Although the mesh elements are relatively high and a smaller number of

elements might be sufficient, no grid test was performed in this simulation as the purpose was a qualitative comparison between the three cases. Figure 5.10 shows a section cut of the mesh for the case of $AoA0°$. The three simulations were under steady state conditions. Reynolds number based on the height of the bunker (Re_H) of 1×10^6 was chosen for this test so, the flow is turbulent. The choice of the turbulence model depends on the level of accuracy needed, and on the nature of the problem being studied. In the large eddy simulation (LES) model, for example, the small length scales are modeled, while the Naiver-Stokes equations are filtered and solved for large length scales. On the other hand, Reynolds averaged Navier–Stokes (RANS) equations are time averaged fluid flow equations. They are not expensive computationally and could be utilized with high Reynolds numbers and complicated geometries. In RANS, all ranges of time and length scales are modeled and not solved. Detailed information on the structure of the turbulent vortices is not needed in this study. As a result, the Shear Stress Transport (SST) $k-\omega$ turbulence model was employed in all simulations as it provides accurate results for those kind of applications (Kim et al., 2017).

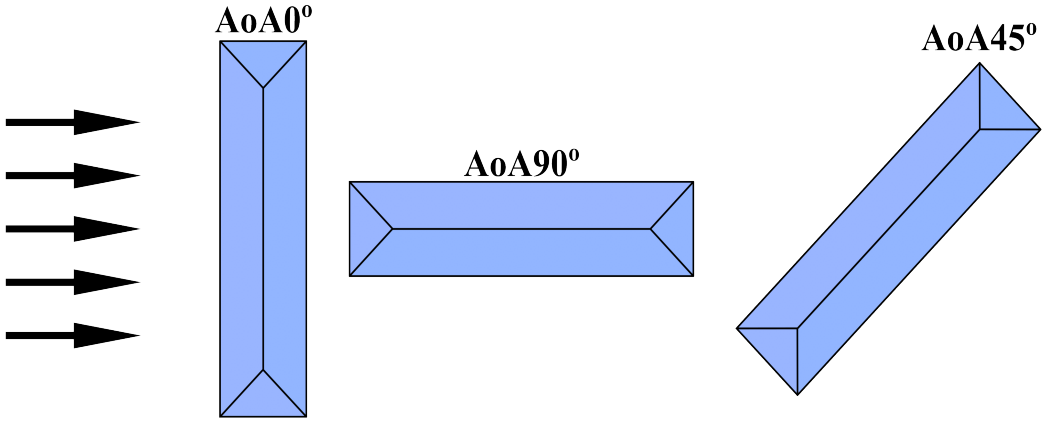

Figure 5.9: Top-view illustration of the three bunker orientations for the external flow model.

The inlet velocity was assumed of a turbulent boundary layer over a flat plate with a thickness equivalent to the height of the bunker (H) and follow the $\frac{1}{7}$ power law (De Nayer et al., 2018). Symmetry boundary conditions were assigned to the top and the two lateral sides while no-slip conditions were set for both the bottom wall (ground) and all bunker's

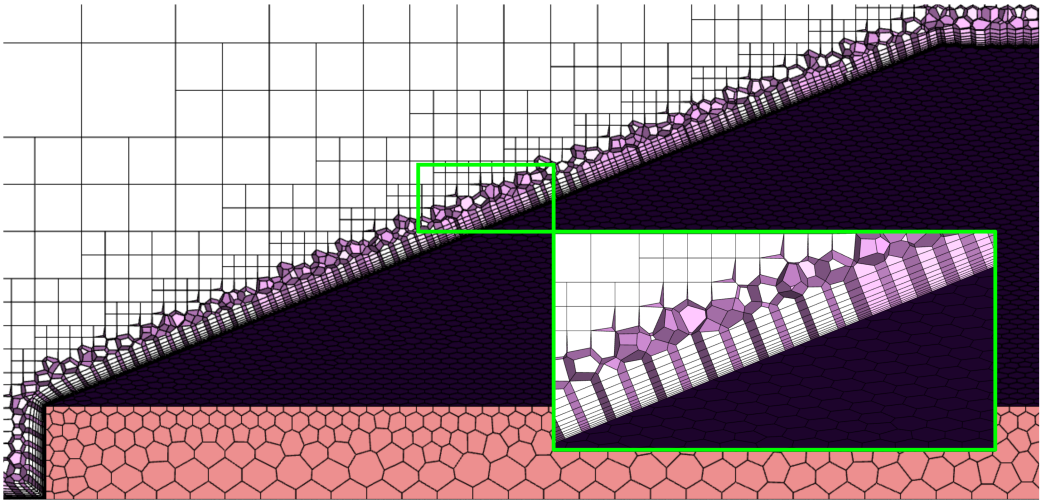

Figure 5.10: Section of the mesh generated for the $AoA0°$ CFD model.

surfaces. No heat transfer was considered in all simulations. The quantity of interest was the pressure coefficient, $c_p = \frac{p - p_o}{0.5\rho U_H^2}$, in which p and p_o are the static pressure at the wall and the reference pressure, respectively, ρ is the air density (kg m^{-3}), and U_H is the air velocity at the height of the bunker (m s^{-1}). Both the mesh generation and the computational calculations were done using ANSYS Fluent version 2021R1.

Results of the pressure coefficient on the tarpaulin in each case are shown in Figure 5.11; $AoA0°$ (a), $AoA45°$ (b), and $AoA90°$ (c). The highest value of the pressure coefficient is for the $AoA0°$ in which the long side of the bunker is subject to wind directed horizontally, followed by $AoA45°$ and the lowest is for the $AoA90°$. Unlike $AoA0°$ and $AoA90°$, the $AoA45°$ show non-uniformity distribution on one of the bunker surfaces. As a result, the $AoA0°$ scenario was considered for all FSI simulations in this study as it subjects to a higher force than the other two orientations and, due to the uniform distribution of those forces, considering a slice for the FSI study as a representative on the entire bunker is more pronounced.

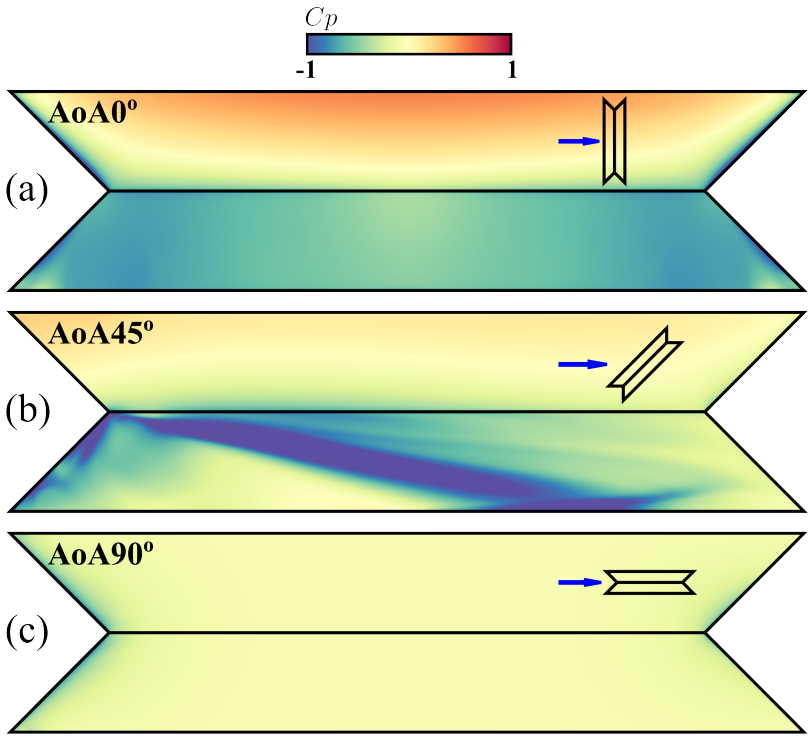

Figure 5.11: Pressure coefficient on the tarpaulin surface of a bunker at different orientations; 0° (a), 45° (b), and 90° (c).

5.2.2.2 FSI simulation

A 3D slice of the bunker with 0.5 m width was considered. Figure 5.12 shows the computational domain with dimensions, boundary conditions, and the fluid and the solid properties. The two lateral surfaces of the domain were defined as symmetry boundary conditions with free-slip at the top and no-slip conditions at the bottom and all bunker walls. A pressure outlet at the left side of the domain boundary for the outflow was assigned. The bunker was assumed to be immersed in a turbulent boundary layer on a flat plate similar to the external flow cases. The velocity inlet was smoothed out in the beginning of the simulation (two seconds) to gradually increase the wind load on the bunker surface and to avoid the high distortion on the tarpaulin within the structure solver. Two scenarios were employed, a constant velocity and a fluctuating velocity. For the constant velocity, the velocity at the inlet varies along the height but does not change with time. Three different Re was chosen; 1×10^5, 5×10^5, and 2×10^6. In contrast, the fluctuating velocity at the inlet is both spatial

and temporal dependent. This was to mimic wind condition scenarios that could happen in real life situations. In this case, Re was fluctuating between 0 and 2×10^5. The material of the tarpaulin was assumed to have similar tent material characteristics (Glück et al., 2001). The number of mesh elements chosen is 40,000 for the fluid domain and 2000 for the solid domain (a no-thickness surface represents the top left wall of the bunker with 0.5 m width). Figure 5.13 shows the structure mesh generated for the fluid domain. The variables of interest in these simulations were the displacement in the vertical direction at three points ($p-$, $p0$, and $p+$ as indicated on Figure 5.12) and its frequency, and the drag and left forces on the top left wall of the bunker surface.

A group of bunkers may be constructed in one location. Steady state CFD simulations with $Re = 5 \times 10^5$ were conducted on the effect of two bunkers built in series. Three scenarios were considered with a single bunker, two bunkers spaced 5 m, and two bunkers with 25 m distance. These distances were picked up from real bunkers on the field to investigate the effect of the distance between bunkers. This is followed by an FSI simulation of the two 5 m distanced bunkers. The interaction between the fluid and the structure solvers were done only on the top left wall of the second bunker. The oscillating velocity condition were adopted for the inlet boundary.

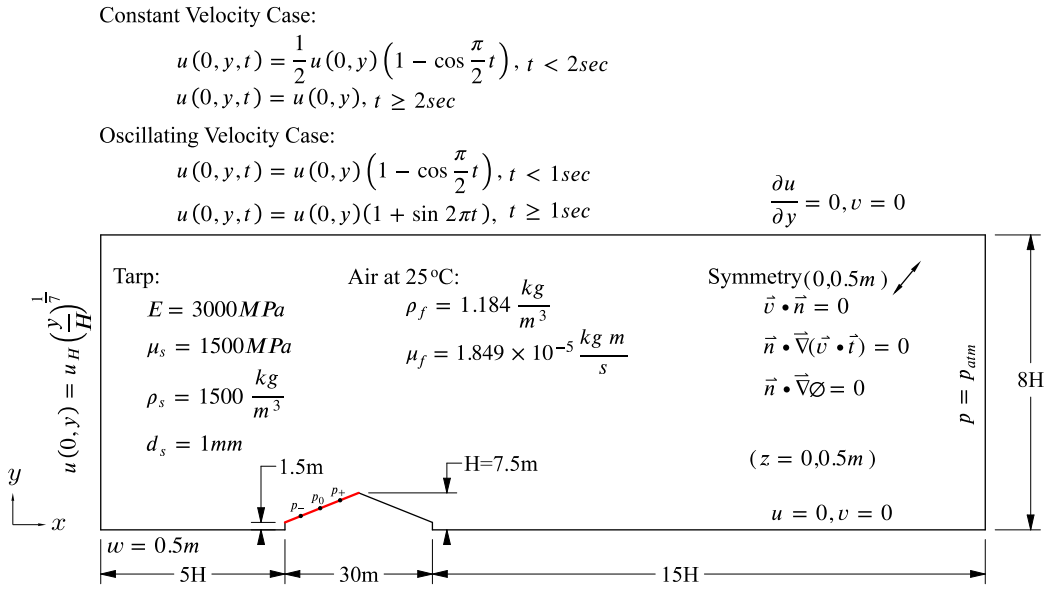

Figure 5.12: The computational domain, boundary conditions, and fluid and solid properties used for the FSI bunker simulations.

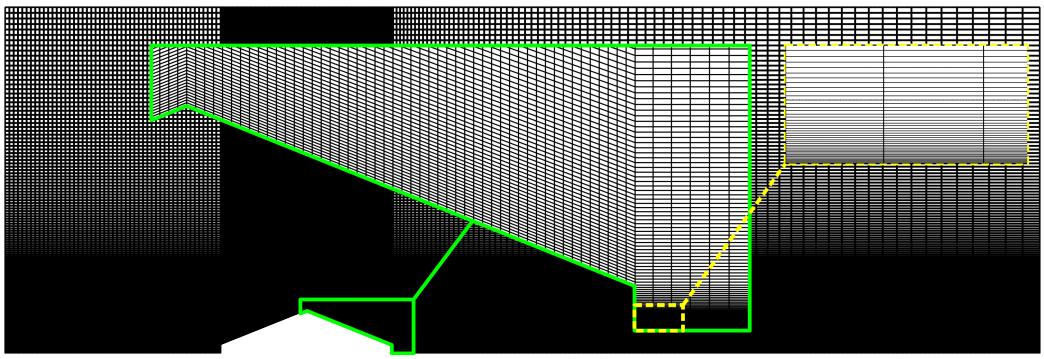

Figure 5.13: Structure mesh generated in the fluid domain for the FSI bunker simulation with zooming in at two locations showing the gradual increase in the mesh size as it moves away from the bunker bottom and the bunker walls.

5.2.2.2.1 Grid and time-step tests The grid test was done on a CFD steady state case. Three different mesh sizes were considered: 19,250 (coarse mesh), 40,000 (medium mesh), and 82,750 (fine mesh) elements. The test was performed on the pressure coefficient on the top left surface of the bunker. FSI simulations are extremely time consuming and a tradeoff between reasonable accuracy and the computation time is crucial. The resulted relative error between the medium and the fine mesh sizes was 1.5% versus 10.3% between the coarse and the fine mesh sizes. As a result, the medium mesh was chosen for all the FSI simulations in this study.

A test on the size of the time-step was also performed with three sizes of 0.08 s, 0.05 s, and 0.01 s. The dimensionless y–displacement (ξ_y) with the height of the bunker (H) and its frequency (f) at three points ($p-$, $p0$, and $p+$) on the top left wall of the bunker as indicated on Figure 5.12, were the variables of interest in this test. Results collected between the simulation time of 20 s to 25 s at Re of 5×10^5 are shown in Table 5.3. Results are of line between the time-step of 0.01 s and 0.05 s and show some differences with the time-step of 0.08 s. However, the time-step of 0.01 s was chosen for all the FSI simulations because it shows better resolution of the displacements. The wall–clock time (excluding the setting up) of each FSI run required about 3 weeks on a 4–core machine (due to software license restriction).

Table 5.3: The non-dimensionalized y–displacement ($\frac{\xi_y}{H}$) and its frequency (f) resulted from the three different time-step sizes (Δt = 0.08, 0.05, 0.01 s) at points ($p-$, $p0$, and $p+$) on the top left wall of the bunker.

Variable	$\Delta t(s)$	Points on the top left wall (Figure 5.12)		
		$p-$	$p0$	$p+$
$\frac{\xi_y}{H}$	0.01	$-0.0645 \pm 7.3 \times 10^{-4}$	$-0.0852 \pm 1.0 \times 10^{-3}$	$-0.0632 \pm 7.6 \times 10^{-4}$
	0.05	$-0.0642 \pm 6.9 \times 10^{-4}$	$-0.0852 \pm 9.9 \times 10^{-4}$	$-0.0631 \pm 7.3 \times 10^{-4}$
	0.08	$-0.0642 \pm 4.7 \times 10^{-4}$	$-0.0852 \pm 6.7 \times 10^{-4}$	$-0.0629 \pm 4.9 \times 10^{-4}$
$f(Hz)$	0.01	1.00	1.00	1.00
	0.05	1.00	1.00	1.00
	0.08	0.79	0.79	0.79

5.2.2.2.2 Constant inlet velocity In this scenario, a constant (with respect to time) velocity was considered with Re of 5×10^5. The top left wall of the bunker was the interface between the fluid solver and the structure solver i.e., all other walls were rigid. The y–displacement (the displacement in the vertical direction) was collected at each time-step at three points ($p-$, $p0$, and $p+$; shown on Figure 5.12). The drag and lift forces per unit depth were calculated at the top left surface of the bunker. The frequency of the y–displacement at the center of the top left wall, point $p0$, was computed using Fourier analysis written in Python and the dominant frequency in the spectrum was identified. Figure 5.14 shows the y–displacement and its frequency at point $p0$, and forces per unit depth on the left surface of the tarpaulin. In the displacement plot, point $p0$ experienced the highest impact from the inflow wind as it is the farthest point from the two rigid ends of the left wall. The displacement at the three points started with high amplitude then decayed with time to a lower amplitude; followed the forces behavior in Figure 5.14. As seen, the motion mechanism of the tarpaulin was found to be sinusoidal with dominant frequency of 1Hz.

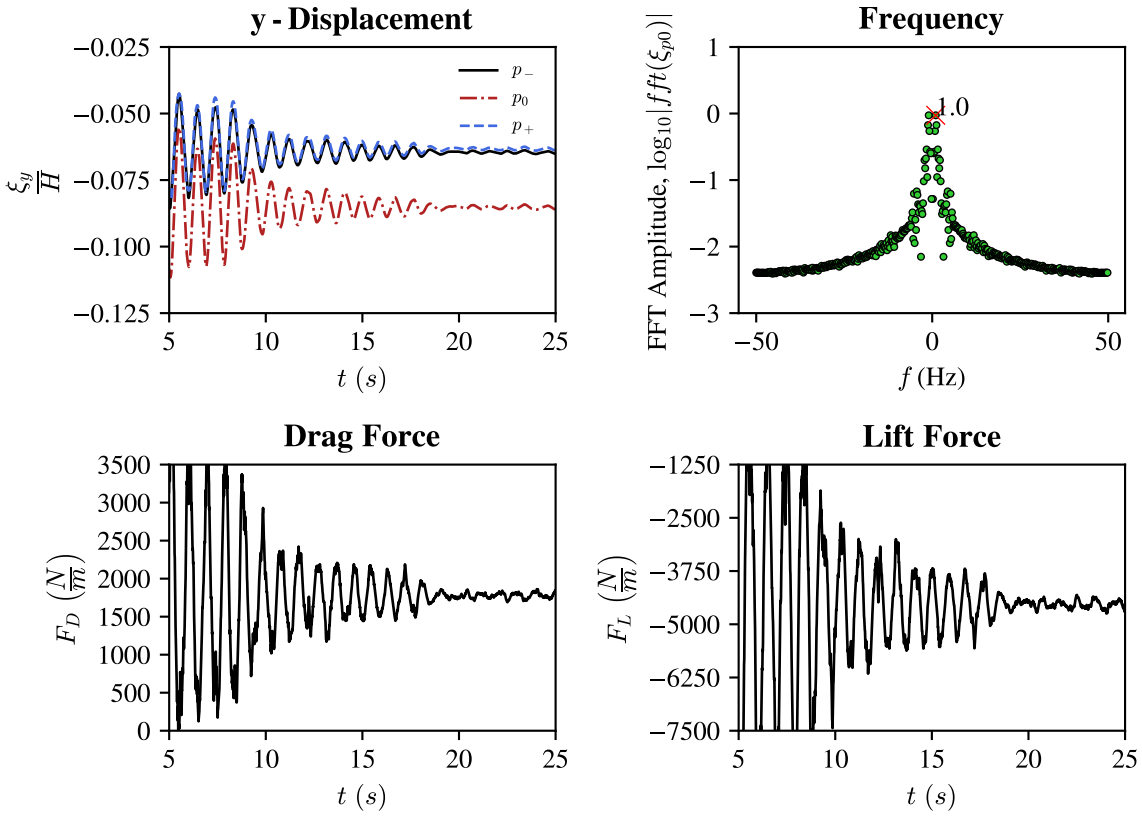

Figure 5.14: The dimensionless y–displacement ($\frac{\xi_y}{H}$) at three points ($p-$ ——, $p0$ ·-·-·, $p+$ - - -), the frequency (Hz) of the y–displacement at point $p0$ (●), and the drag and lift forces per unit depth ($\mathrm{N\,m^{-1}}$) (——) at the left wall of the tarpaulin resulted from the constant inlet velocity case versus time (s).

5.2.2.2.3 Effect of Reynolds number The intensity of the wind speed depends on the location where bunkers are built and the season of the year. Three FSI simulations with constant inlet velocity at three different Reynolds numbers were performed; $Re = 1 \times 10^5$, $Re = 5 \times 10^5$, and $Re = 2 \times 10^6$. Figure 5.15 shows the y–displacement at point $p0$ resulted from the three cases. As seen, in the first 10 s, the lower the Re the higher the amplitude. That is, a lower velocity seemed to trigger the tarpaulin motion more than a higher velocity. Then, they all started to dip to lower values while the Re of 2×10^6 showed more chaotic behavior as a response to a high value of Re. Regardless of the amplitude and the increase in Re, the dominant motion mechanism is still sinusoidal.

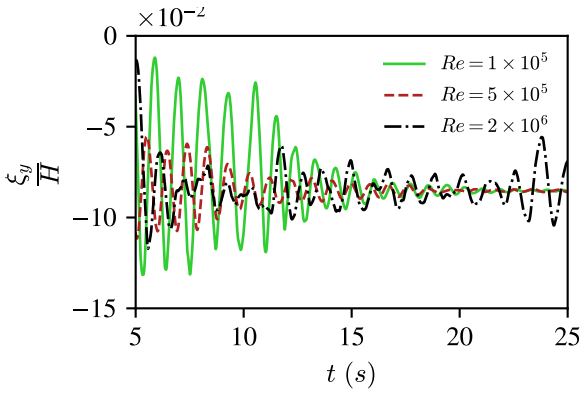

Figure 5.15: The dimensionless y–displacement ($\frac{\xi_y}{H}$) at point $p0$ at three Reynolds numbers of 1×10^5 (——), 5×10^5 (- - -), and 2×10^6 (-·-·-) versus time (s).

5.2.2.2.4 Oscillating inlet velocity In real life situations, velocity varies with time. A case in which the inlet velocity oscillates over time was studied. In this scenario, Re fluctuates between 0 and 2×10^5. The y–displacement at three points, $p-$, $p0$, and $p+$, on the left wall of the tarpaulin is shown in Figure 5.16. The fluctuation velocity had triggered the tarpaulin at a higher intense than the constant inlet velocity even with higher Re. A pattern of an increase in the amplitude followed by a decrease was observed as shown in the figure. This pattern is resulted from the ups and downs in the inlet velocity. As before, there was no change in the motion mechanism itself.

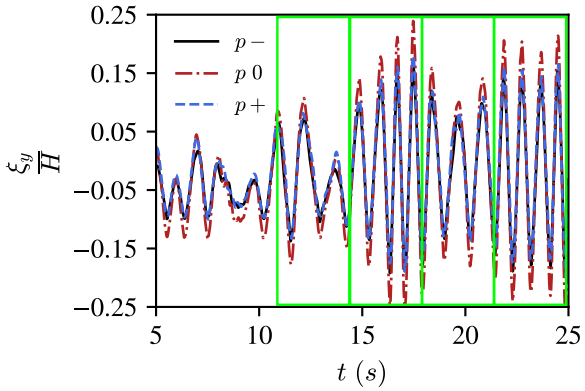

Figure 5.16: The dimensionless y–displacement ($\frac{\xi_y}{H}$) at three points located on the left side of the tarpaulin ($p-$ ——, $p0$ -·-·-, and $p+$ - - -) resulted from the oscillating inlet velocity case versus time (s).

Figure 5.17 shows the sinusoidal motion of the tarpaulin at different times, 0 s – 20 s (a –

f). Figure 5.18 shows the vorticity contours at 25 s. From the contours the right side of the tarpaulin is subject to much less wind vortices in turn it may not move.

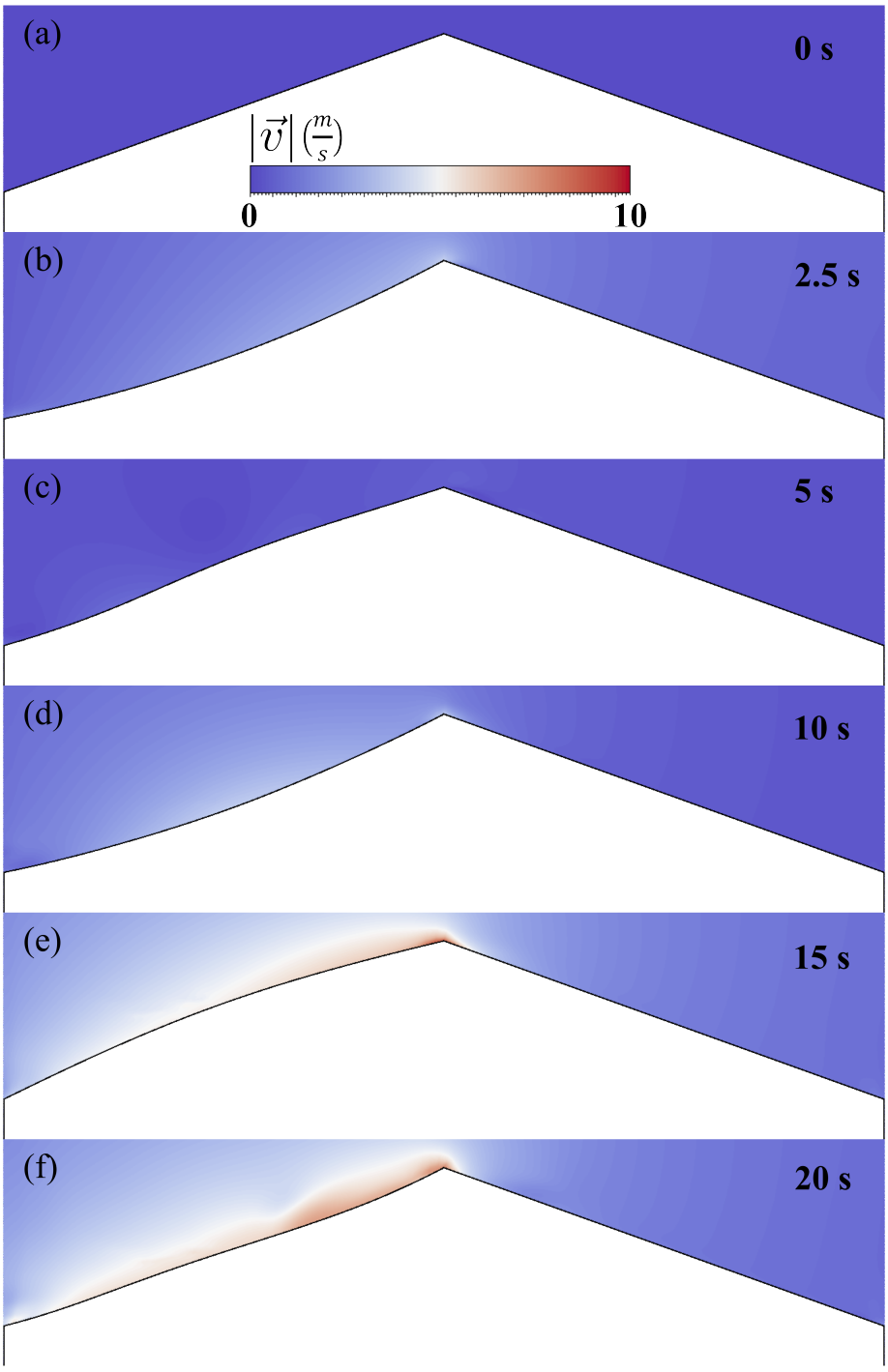

Figure 5.17: The motion mechanism of the tarpaulin at different times resulted from the oscillating inlet velocity case.

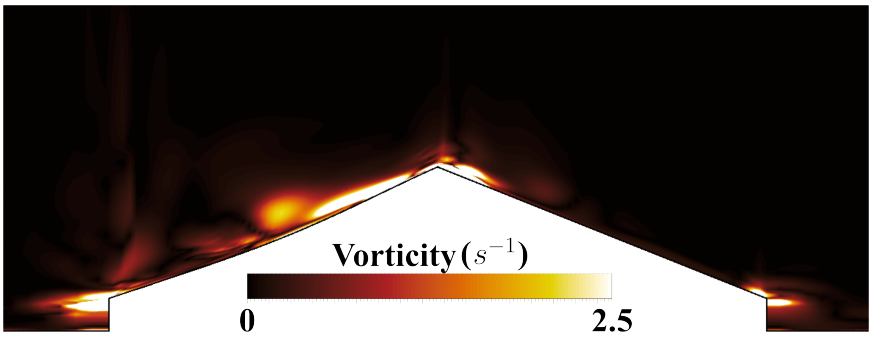

Figure 5.18: Contours of vorticity at 25 s from the oscillating inlet velocity scenario.

5.2.2.2.5 Multiple bunkers Usually there is more than a single bunker at a grain storage location, with no specific spacing or orientation between them. A qualitative steady state CFD simulation was conducted on the effect of the distance between two bunkers. Two distances were chosen from a real-life site: 5 m and 25 m. Figure 5.19 shows the turbulent intensity of (a) a single bunker, (b) two bunkers spaced 5 m, and (c) two bunkers distanced 25 m. As seen, the first bunker acts as an obstacle to those behind it so, other bunkers downstream the first one may experience more intense wind load. Comparing between the three situations, the smaller the distance between bunkers, the less wind intensity on the left side tarpaulin of the second bunker.

A 15 s FSI simulation was done on a case with two 5 m spaced bunkers. In this scenario the oscillating inlet velocity was employed with Reynolds number ranging between 0 to 2×10^5. The shared wall between the fluid and the structure solver was the left side of the second bunker downstream. The resulted y–displacement was compared to a case with a single bunker in which the shared wall is the left side of the tarpaulin. Figure 5.20 shows this comparison obtained at the center of the left side wall for both cases; a single bunker and the second bunker in two bunkers scenario. The displacement from the case of two bunkers has a higher amplitude but is more harmonic and can be simplified by a sin function.

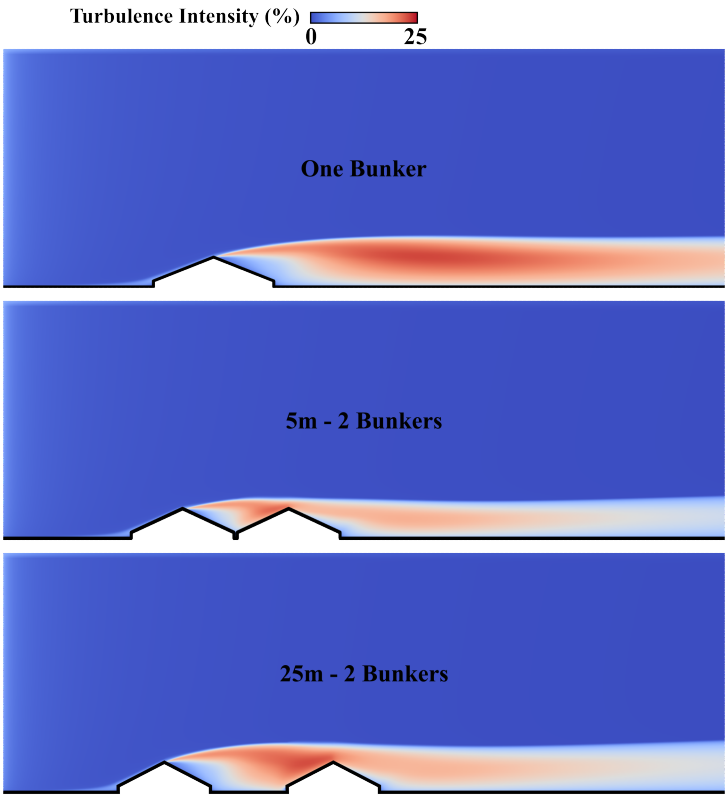

Figure 5.19: Turbulent intensity (%) from steady state CFD simulation on a single bunker (a), two bunkers spaced 5 m (b), and two bunker spaced 25 m (c).

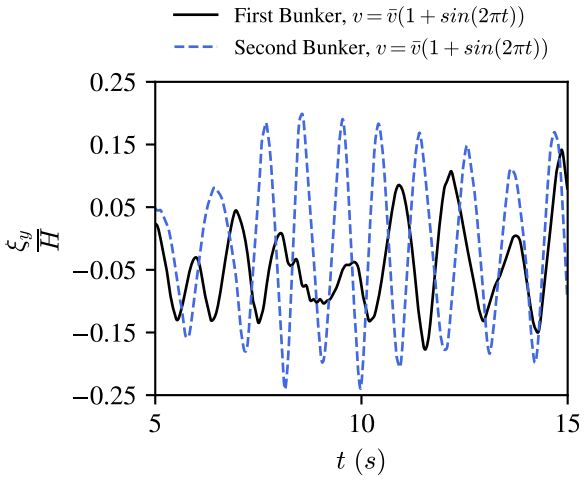

Figure 5.20: The dimensionless y–displacement ($\frac{\xi_y}{H}$) at the center of the left side wall in a case with a single bunker (——) and a case with 5 m spaced two bunkers (- - -) in which the left wall of the second bunker downstream was the target versus time (s).

5.3 Dynamic walls – internal flow

5.3.1 Equation for tarpaulin motion

Based on the results from the FSI simulations on bunker, a mathematical correlation that describe the tarpaulin motion was defined based on the standing wave concept. A standing wave is constructed when two waves of the same amplitude, but different directions meet. The formed wave propagates up and down with double the amplitude but no traveling. Mathematically, the resulted standing wave is the summation of those two waves. Characteristics of standing waves, in general, can be found in literature (e.g., Tipler and Mosca, 2003). The motion of one side of the tarpaulin was defined as a standing wave that is initially at rest then it moves up and down while the two ends are fixed. To satisfy these criteria, the displacements of the two waves were assumed as

$$\xi_1(x,t) = Acos(\omega t - kx) \tag{5.1}$$

and

$$\xi_2(x,t) = -Acos(\omega t + kx) \tag{5.2}$$

Summing up Eqs. 5.1 and 5.2, and using the trig identities,

$$\xi_s(x,t) = A_s sin(kx) sin(\omega t) \tag{5.3}$$

In Eqs. 5.1, 5.2, and 5.3, ξ_1, ξ_2, and ξ_s ($\xi_s = \xi_1 + \xi_2$) are the displacements of the first wave, the second wave, and the resultant standing wave (m), respectively, A and A_s ($A_s = 2A$) are the amplitude of the original wave and the amplitude of the standing wave (m), respectively, $k = \frac{2\pi}{\lambda}$ is the wave number (m^{-1}) in which $\lambda = \frac{2L}{n}$ is the wavelength (m) with n is the number of loops and L is the length of one side of the top surfaces of the bunker (left or right), $\omega = 2\pi f$ is the angular frequency (rad s^{-1}) in which $f = \frac{1}{T}$ is the frequency (Hz) while T is the period (s), and x is a position vector (m) along the length L. Between the two ends

of the surface (top left or top right of a bunker) one or more loops can be constructed. This depends on several factors such as wind condition, bunker orientation, the smoothness of the grain surface, and the tightness of the tarpaulin. Figure 5.21 illustrates the wave behavior of different loops; 1, 2, 3, and 10 loops, on a bunker surface.

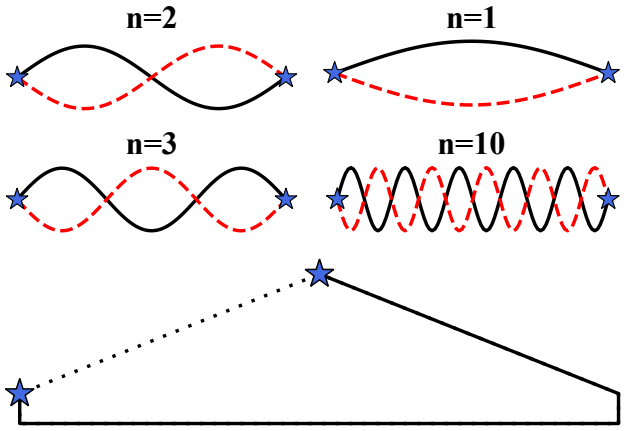

Figure 5.21: Illustration on the number of loops constructed on the top left side of the bunker surface.

Eq. 5.3 was coded, in C, as a dynamic wall and linked to ANSYS Fluent version 2021R1. In this case, the wall moves with an amplitude and number of loops that are predefined. In this code the top surface of the bunker is divided into nodes, based on the generated mesh. The two nodes at the two ends are fixed while the other nodes in between, respond to the prescribed motion. Modeling PH_3 does not require a small time-step, however, the time-step size was very small – adjusted based on the frequency (f) – to capture the tarpaulin motion. In the case of the moving tarpaulin, a time-step that is at least 10 times smaller than the frequency is required. The mesh in the computational domain in the bunker is then deformed at each time-step to respond to the change in the shape induced by the moving wall. PH_3 gas is then redistributed to respond to the dynamic wall that mimics the motion of the tarpaulin. For the mesh deformation in response to the moving wall of the bunker, the diffusion method was found to give best performance for the domain shape of the bunker and the hexahedral mesh used and, as a result, was used in all simulations. In this method, the motion of each node is based on the velocity of that node. The velocity is calculated from the defined displacement at the node using a diffusion equation. The boundary distance

with zero diffusion parameter was set. GMRES with smoothing from a reference position was defined for the AMG stabilization.

Figure 5.22 shows a case resulted from the Fluent solver every 0.2 s of 10 s simulation with n = 4 loops, f = 1Hz, A = 0.15m, and Δt = 0.1 s. This approach can be applied to the top right wall of the bunker or even both the top walls. The smoothness of grain and how the tarpaulin is tightened up at some node around the bunker's side wall plays a role in the tarpaulin movement. As a result, part of the same tarpaulin may move with certain amplitude or number of loops while other parts have different values or do not move. The code and the approach can simply be applied with specific amplitude, frequency, and number of loops along a certain length (area) of the bunker surface, while other parameters are to be set to other areas of the same surface. It also can be applied on 2D as well as 3D domains.

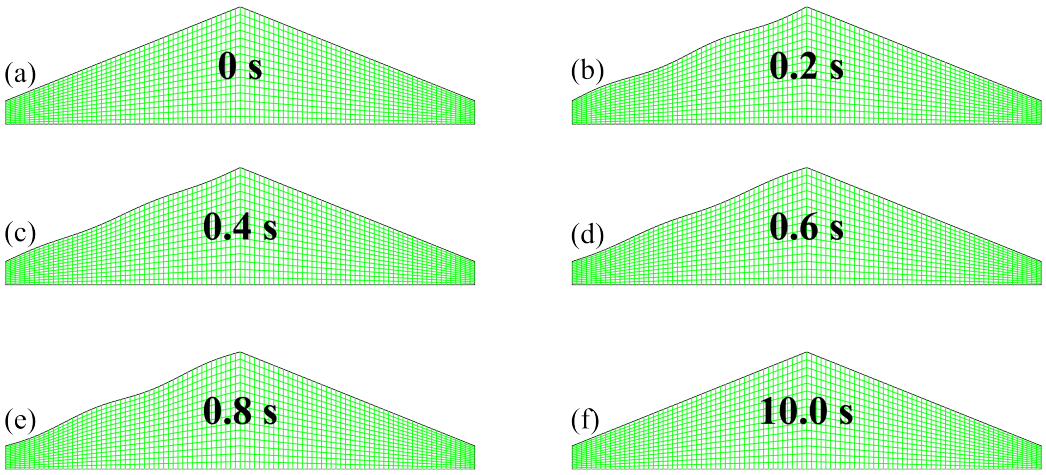

Figure 5.22: Results of a dynamic wall case at 0.2 s in 10 s simulation that mimics a tarpaulin billowing with n = 4 loops, f = 1Hz, A = 0.15m, and Δt = 0.1 s.

5.3.2 Bunker with moving boundaries

The computational domain of the bunker was divided into two regions or zones; a porous zone (wheat) and a non-porous zone (headspace) in which no grain is present. Unlike other grain storage facilities such as bins, the exact size of the headspace in bunkers is unknown and depends on many factors mostly the smoothness of the top surface of the grain and the tightness of the tarpaulin. Leakage in bunkers is unavoidable so, two points for the inflow

and outflow were considered. Figure 5.23 shows the boundary and zone conditions. As seen, within the porous zones, two separate sub-zones were defined for PH_3 releasing points and placed directly under the headspace and immersed entirely in the wheat. Figure 5.24 shows the computational domain along with the dimensions. Structure mesh was created with 10,700 elements shown in Figure 5.25.

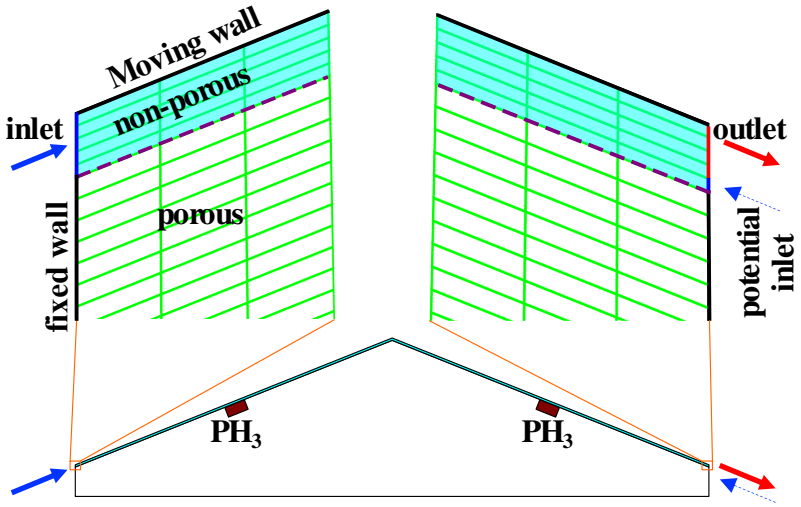

Figure 5.23: Zones and boundary conditions set for internal flow simulations of the bunker.

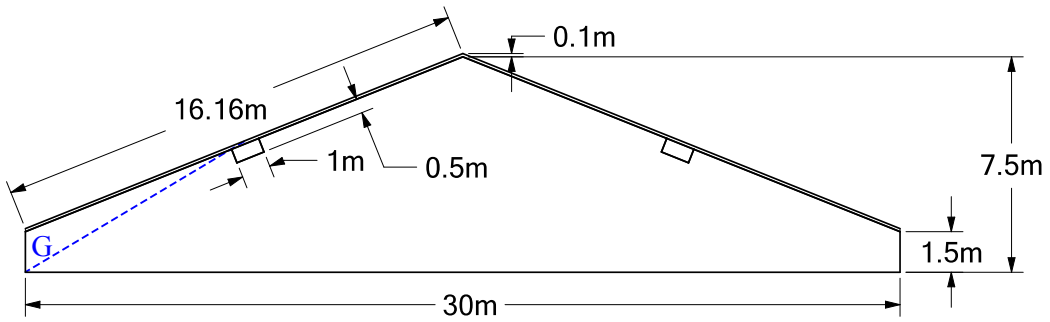

Figure 5.24: The computational domain with dimensions used for the internal flow simulations of bunkers. Line G (- - -) was used for the grid test.

Grid test was done on a case with pure diffusion at segment G indicated on Figure 5.24. Three different mesh sizes were tested: a coarse mesh with 10,700 hexahedral cells, a medium mesh with more than three times the number of elements of the coarse mesh (39,900), and a fine mesh with more than seven times the number of elements of the coarse mesh (76,850). The quantity of interest in this test was for the PH_3 concentration (ppm) at one

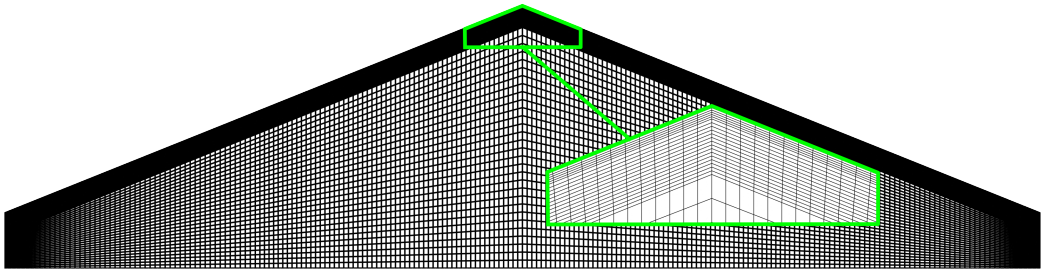

Figure 5.25: Hexahedral mesh generated for the internal flow simulations of bunkers with zooming in at the top center.

day simulation time and sampled along line G. The concentration between the medium and the fine mesh is almost coincided with a slight difference between the coarse mesh, especially towards the headspace. This change in the concentration is insignificant in terms of fumigation. The mesh in the headspace area is subject to deformation at each node along the entire wall caused by the motion of the boundary. Fine mesh may cause elemental distortion especially with hexahedral cells as the one in this study. As a result, a tradeoff between the accuracy and the complication of the mesh deformation was made and the coarse mesh was chosen for the simulation of PH_3.

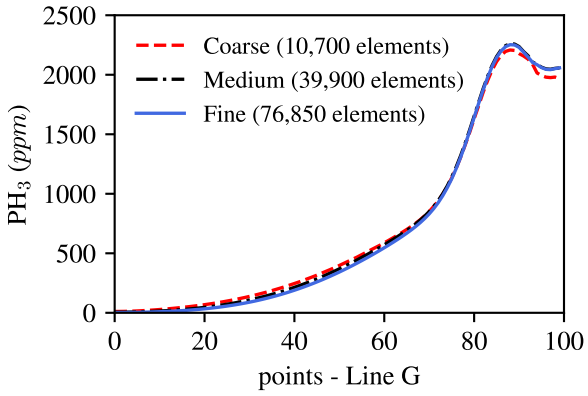

Figure 5.26: PH_3 concentration (ppm) along line G (Figure 5.24) at 24 h with three different mesh sizes (coarse - - -, medium -·-·-, fine ——).

Tarpaulin covering grains in bunkers is mostly done by handwork. The smoothness of the grain surface and the looseness of the tarpaulin is case-to-case dependent. The way tarpaulin is tightened causes some areas to be crimpy which may change the motion mechanism of the tarpaulin. The amount and locations of leakage are highly unpredictable. Bunkers have

different orientations in a single site as a result, the tarpaulin motion response to one bunker is different from another bunker that is at the same location. The distance between bunkers is also case-to-case dependent or even the configuration of each bunker to its neighbor varies from one site to another or even within a single site. Based on the FSI results, the tarpaulin motion can be simplified as a standing wave of two multiplied sinusoidal functions that vary with both space and time. However, because of all those reasons, it is impossible to know the exact amplitude of the tarpaulin motion. Moreover, which area of the tarpaulin may move, and the duration of the movement are also unknowns; unless a case-by-case simulation is done in which many parameters such as leakage, smoothness, etc., need to be controlled or known. This approach of a dynamic wall with a standing wave function gives the freedom and the applicability to be applied in any situation that may occur in real-life scenarios. Different amplitudes, frequencies, or number of loops can be assigned to different areas of the tarpaulin. Not only that, but those parameters can also be time dependent.

5.3.2.1 Effect of headspace

To study the impact of the headspace on the PH_3 distribution without the effect of tarpaulin movement, two transient CFD cases were run, with and without headspace. The mortality fraction discussed in Chapter 4 was adopted to distinguish between the results quantitatively. A mortality fraction of 100% is when the entire bunker is filled with a lethal dosage and vice versa. Figure 5.27 shows the PH_3 contours obtained from the two scenarios at 24 h. Air and PH_3 within wheat, represented as a porous medium, experience a decrease in the mass diffusivity. That is, gases move freely or faster in the headspace. Then because of gravity, PH_3 moves downwards. These (diffusion and gravity) are reflected on the PH_3 behavior in Figure 5.27(b). In terms of the mortality fraction, it is 31.3% with headspace versus 19.9% without headspace. So, leaving more room between the grain surface and the tarpaulin is desired if leakage can slightly be controlled or monitored.

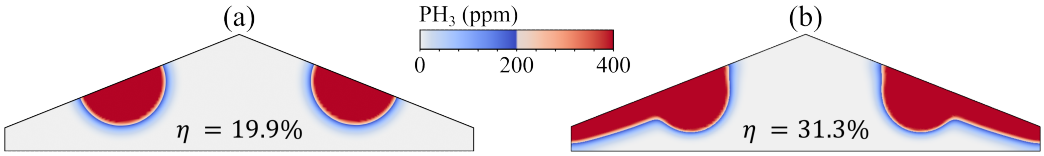

Figure 5.27: PH_3 contours (ppm) at 24 h showing the effect of headspace on PH_3 distribution; (a) no headspace and (b) with headspace.

The 2D case was compared to a 15 m width 3D slice as shown in Figure 5.28 – the PH_3 contours at 24 h. The mortality fraction from the 3D was 29% versus 31.3% of the 2D. This difference is an accumulated numerical error mainly from the evolution rate equation discussed in Chapter 3. As there was no significant difference between the two results, the 2D model was considered for the rest of the analysis.

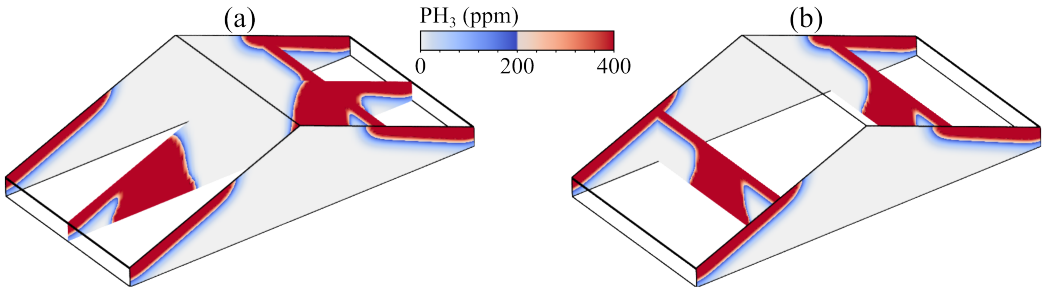

Figure 5.28: PH_3 contours (ppm) at 24 h of a 3D slice of the bunker with neither leakage nor tarpaulin movement.

5.3.2.2 Effect of leakage

Three different leakage rates were considered to represent three situations that could possibly occur in the field; a leakage rate that has low or no effect on the PH_3 distribution, a leakage rate that has a medium impact, and a leakage rate that has a significant effect on the gas distribution. Those three values in terms of mass flow rate are 0.0005, 0.001, and 0.005 $kg\,s^{-1}$. Figure 5.29 shows how the PH_3 respond to each case along with the mortality fraction. The mortality fraction of the low mass flow rate is almost the same as no leakage (30.5% versus 31.3% of no leakage) then gradually decreases as the leakage rate increases. As explained, because there is no wheat in the headspace, PH_3 moved at a faster rate from the inlet towards the outlet and almost disappeared in the case of the highest leakage rate, Figure 5.28(c).

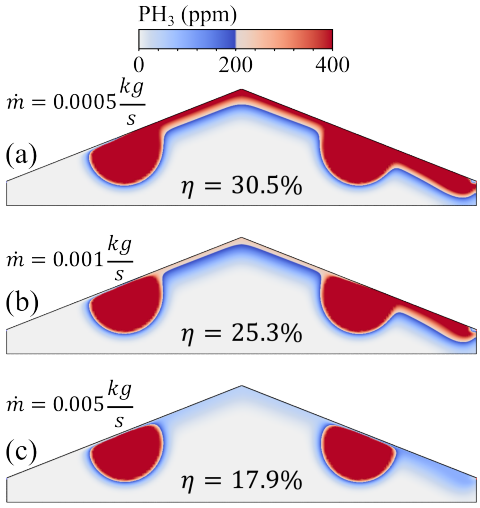

Figure 5.29: PH_3 contours (ppm) at 24 h for three different leakage rates; 0.0005 (a), 0.001 (b), and 0.005 $kg\,s^{-1}$ (c).

5.3.2.3 Effect of tarpaulin billowing

Frequency of the y-displacement resulted from the FSI simulation is 1 Hz. Which means the tarpaulin moves up from its original position then moves down then returns to its original position in 1 s. In reality, and because of all the reasons mentioned above, no tarpaulin moves continuously during the 24 h of the day even with continuous wind. Neither will it keep the same frequency, amplitude, nor number of loops. To visualize the effect of one parameter, number of loops, of the tarpaulin billowing on PH_3 behavior in bunkers, a large frequency of 0.1Hz was chosen for a slower, but continuous, motion of the tarpaulin. In this show case, two number of loops were considered, 1 and 10 loops with the same amplitude of 5 cm. Only the left side of the tarpaulin was subject to motion while the right side was assumed to be rigid. Figure 5.30 shows the PH_3 contours (ppm) 24 h duration with 10 loops (a) and one loop (b). This had a significant impact on the PH_3 distribution as a result of changing a single parameter, the number of loops. One loop showed much better performance for the PH_3 distribution than the 10 loops. The mortality fraction in the case of one loop is 93.4% versus 53.6% from ten loops.

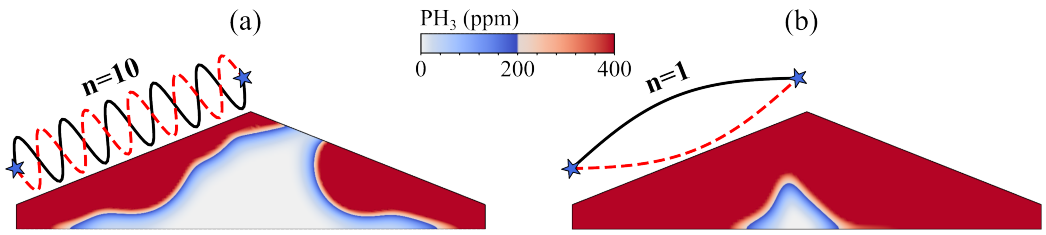

Figure 5.30: PH_3 contours (ppm) at 24 h and tarpaulin moving continuously with 0.1 Hz, 5 cm amplitude, 10 loops (a), and 1 loop (b).

5.3.3 Predicting the mortality fraction

As there are numerous unknown factors on the tarpaulin motion that may affect the PH_3 behavior, a deep learning model was built to correlate between those motion parameters and the mortality fraction. That is without the need to CFD modeling, the Deep Neuron Network (DNN) model can predict the mortality fraction at any given number of loops and amplitude between the two surfaces of the bunker. The model is intended to give a measure of sensitivity on the effect of different parameters on the mortality fraction. The model can be fed with real experimental data along with the CFD simulations results. More inputs can be added to enhance the generalization of the model such as the longitude and latitude of the bunker location, dominant wind speed and direction, the observed dominant duration per day of the tarpaulin movement, if the movement occurs on the entire surface or part of the surface, and the application rate. As more data is fed to the model, the fumigation success rate can be predicted beforehand and as a result, the application rate of the PH_3 can be increased or decreased based on the outcome to ensure a successful fumigation process. The model can be altered to predict the spatial variation of the PH_3 concentration at specific time or a different DNN architecture to add the temporal variation, but this might be appropriate to a more controlled storage environment such as bins.

The main inputs to this model are the amplitude and the number of loops in each side of the bunker. The actual frequency of 1 Hz, resulted from the FSI simulation, was considered. The two releasing points of the PH_3 were initialized with a mass fraction of 1 for the PH_3 and 0 for the air, with no PH_3 in the rest of the computational domain i.e., mass fraction of

0 for the PH_3. Hundreds of simulation cases were run for 500 s with time-step of 0.1 s. Each run required about 5 hours on a 4–core processor. The effect of leakage was insignificant due to the small duration of the simulation time as a result, it was discarded from the model. Multiple tests were done on the architecture of the network. Based on the results of those tests, the DNN, shown in Figure 5.31, consists of one input layer with nine variables, two hidden layers; one with 256 neurons while the other has 128 neurons, and one output layer that gives the mortality fraction in percentage. The cost function considered was the mean squared error (MSE) and the gradient descent optimizer (SGD) with a learning rate of 1×10^{-4} (tested and found to be the optimal value) was used to minimize this cost function. The mean absolute error was monitored during the training of the model to judge its performance. The two hidden layers were regularized using the $L2$ method as a weight penalty to avoid overfitting the model with a regularization factor of 1×10^{-5} (also, tested and found as the optimal value). The Rectified Linear Unit (ReLU) activation function was used for both the hidden and the output layers. The input layer was normalized using the mean and the standard deviation of the training data.

The main input to the algorithm was the CFD data at four different number of loops (n = 1, 2, 5, 10) and three different amplitudes (A = 0.01, 0.025, 0.05 m) under different scenarios. Some interpolations, when appropriate, were applied to generate more samples. The algorithm then split these data into six configurations: (1) the movement is only at the right side of the bunker, (2) the movement is only at the left side of the bunker, (3) the movement is at both sides with the same n at both surfaces and the same A, (4) the movement is at both sides with the same n at both surfaces but different A, (5) the movement is at both sides with different n but with the same A, and (6) the movement is at both sides with different n and different A. Once data was categorized, each group was randomly split into 80% for training and 20% for validation. The randomization seed was controlled to ensure consistent results. Then the six training matrices were concatenated into one matrix to represent the training set which was divided into a matrix that consist of the values of n and A, and a vector of the corresponding mortality fraction. The same process was applied to the validation set. Five more features were then extracted to help the DNN model find the

non-linear relations between all variables i.e., the total number of inputs were nine instead of four. These steps are shown in Figure 5.31. The model was trained for 750 epochs with a batch size of 12. Table 5.4 shows the range and limitations that the model was built and tested on.

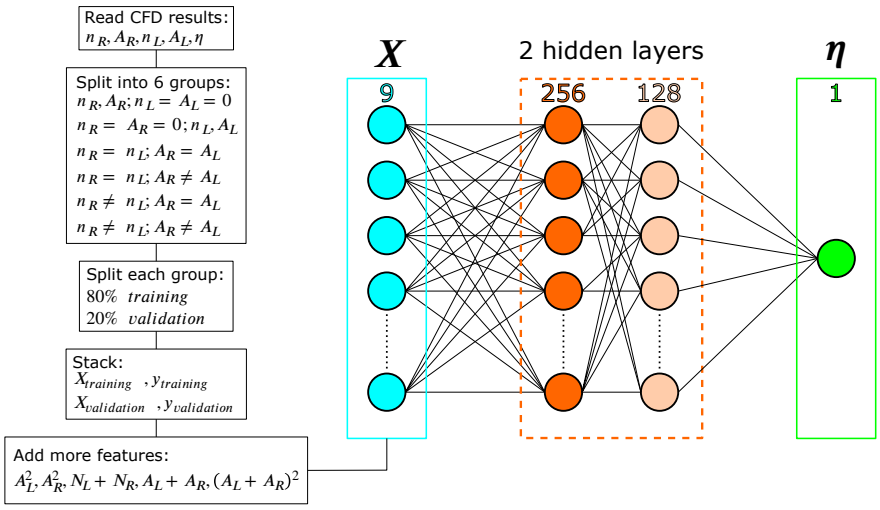

Figure 5.31: The DNN structure with a flowchart of the main steps of the algorithm.

Table 5.4: The range and limitations of the mortality fraction DNN model.

Parameter	Limitation
Number of loops (n)	0 – 10
Amplitude (A)	0 – 0.07 m
Moving Surface*	one or two surfaces (left, right, or both)

*The motion for part of a surface was not considered.

Figures 5.32 and 5.33 show the mean squared error (MSE) and the means absolute error (MAE), respectively, at each epoch. No more improvement was monitored after the 750 epochs for the validation set. The MSE and MAE of the training data at 750 epochs was 0.387 and 0.363%, respectively, compared to 5.976 and 0.976% of the validation data. New CFD runs were conducted with different number of loops and different amplitudes (e.g., n = 3, 6, 7, and 8 loops, and A = 0.015, 0.035, 0.02, 0.065, and 0.07 m) than the ones used in the DNN was utilized for testing the model along with some unseen data, during the training,

with similar n and A of those of the DNN model. That was to ensure the reliability and the generalization of the model. The MSE and the MAE resulted from the testing data was 3.6 and 1.59%, respectively, with R^2 of 0.985. Figure 5.34 shows the DNN model prediction versus the CFD results. The DNN predictions show a good and consistent agreement with the CFD results.

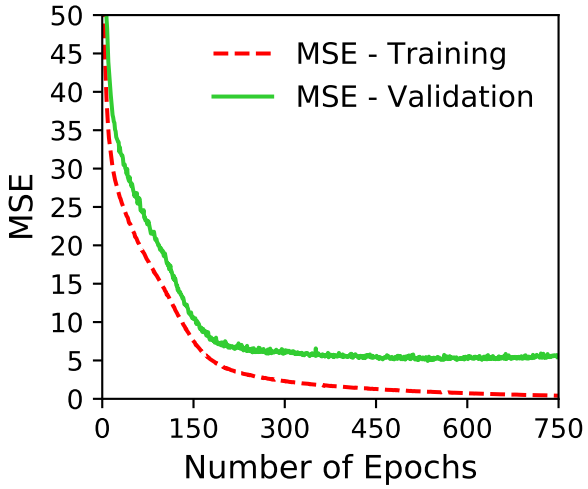

Figure 5.32: The mean squared error of both the training (---) and validation (—) data at each epoch.

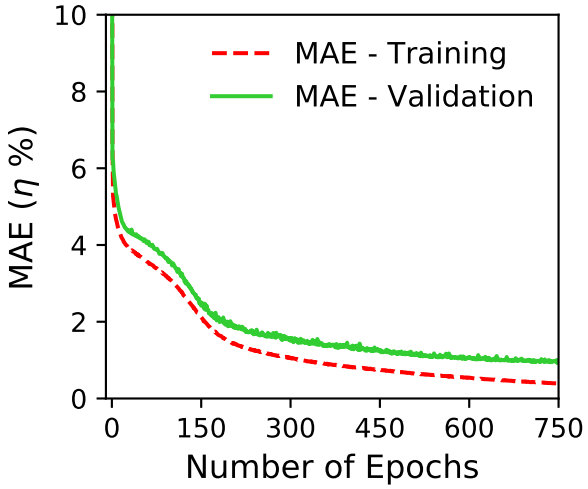

Figure 5.33: The mean absolute error of both the training (---) and validation (—) data at each epoch.

To describe the results used in the DNN model, Figure 5.35 visualizes the effect of the number of loops; n = 1 (a, c, e) and n = 10 (b, d, f) at three different motion locations. These

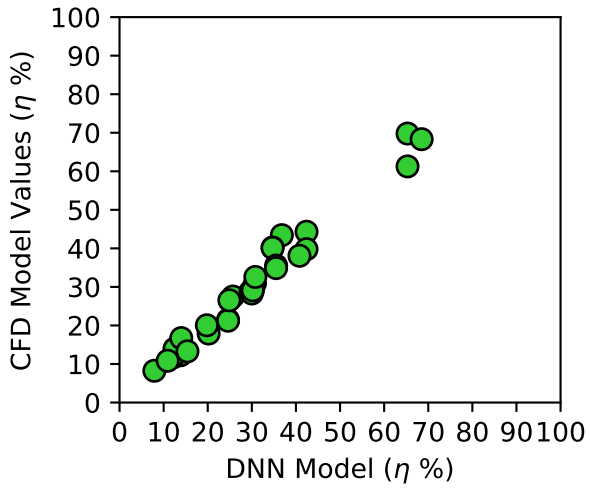

Figure 5.34: Comparison between the DNN model prediction and the CFD results of the mortality fraction (η) on the testing dataset.

locations are (1) only the right side of the tarpaulin moves (a, b), (2) only the left side moves (c, d), and (3) both sides move (e, f). It can be seen that the motion of one wall, either left or right, improves the mortality fraction (η) significantly. However, if both walls are moving the η slightly improves. As a result, the η does not double in value obtained from a single wall movement, when both walls are moving.

The contribution of the amplitude (A) is as significant as the contribution from the number of loops (n) as shown in Figure 5.36 (A = 0.01 m (a) and A = 0.05 m (b) at the same n of 1). That is, either decreasing the number of loops or increasing the amplitude will immensely enhance the fumigation process in bunkers. Both factors can be forced while building bunkers or covering the grain with tarpaulin. Some guidance for achieving this goal are provided in Chapter 6.

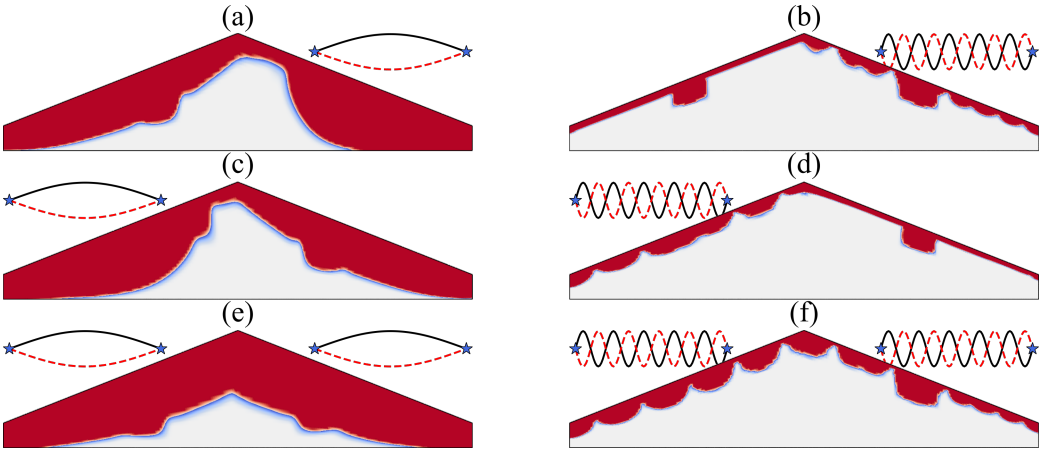

Figure 5.35: PH_3 contours (ppm) at two different number of loops; $n = 1$ (a – e) and $n = 10$ (b – f). (a, b) only the right wall moves, (c, d) only the left wall moves, and (e, f) both walls move.

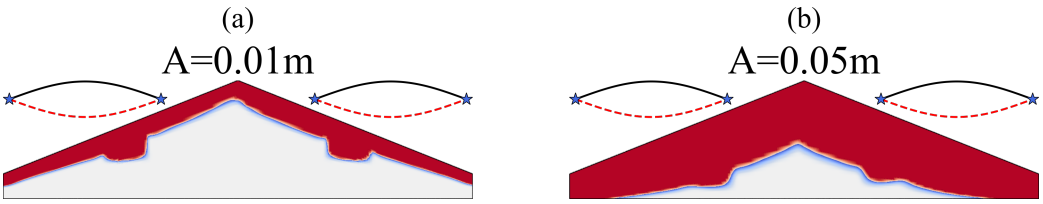

Figure 5.36: PH_3 contours (ppm) at two different amplitudes; (a) $A = 0.01\,\mathrm{m}$ and (b) $A = 0.05\,\mathrm{m}$, with the same number of loops ($n = 1$) and both walls moving.

Chapter 6

Summary and Conclusion

The main objectives of this study were primarily to develop a reliable CFD model that predicts PH_3 behavior in grain storage bunkers. Based on this behavior, recommendations for best management practices for phosphine fumigation in bunkers can be made. The problem was divided into three stages; internal flow, external flow, and a model that involves both. The internal flow involved developing the evolution rate of phosphine from aluminum phosphide (AlP) tablets/pellets, different ways of mathematically representing wheat as a porous medium, the phosphine absorption into wheat, the change in the absorption rate due to temperature, and the effects of heat transfer on the phosphine behavior under various physical parameters, such as location of PH_3 releasing points, bunker shape, leakage, sorption, bunker orientation, and temperature fluctuation. The external flow model utilized FSI simulations to understand the movement mechanism of tarpaulin induced by different wind conditions. Finally, a model was created that combines both the external results as a boundary condition and the internal flow to examine the effects of the tarpaulin movements on the phosphine distribution, and how to control different parameters to ensure the lethal concentration everywhere within the bunker.

In Chapter 2, a detailed literature review with visual quantitative comparisons on the wheat resistance to gas flow was provided. This review showed that Ergun's (1952) equation in terms of the tortuosity factor and sphericity could be suitable for grain applications.

This was tested only for wheat so, more tests on different types of grains are required for generalization. Different factors that affect wheat resistance to gas flow were discussed in Section 2.2.2. Resistance coefficients of the experimental work of Hood and Thorpe (1992) were used in all the simulations to reasonably mimic a bulk of wheat. A description on the governing equations employed for the internal flow simulation of this study was made. A new method, using CFD modeling, that can be utilized for estimating the resistance coefficients without experiments was introduced and the results agreed fairly well with the experimental data of Molenda et al. (2005a). Further investigations on different types of grains with different orientations are needed for completeness of this technique.

In Chapter 3, a mathematical relationship as a function of temperature and absolute humidity was developed for predicting the PH_3 evolution rate from standard solid formulations (tablets and pellets) based on experimental data from Tan (1994). The mathematical relationship compared well with additional experimental data from Couch and Shaheen (1984) at both moderate (50%) and high (90%) relative humidity (RH) levels. Darby's (2008) coupled ordinary differential equations were solved analytically and numerically through CFD simulations, and the results were identical, accounting for the PH_3 sorption rate. From Darby's experiment in 2011, it was found that the sorption rate increased as the temperature increased, and changing the value of the irreversible binding coefficient (K_{bind}) could be used to account for the rate change. Both the evolution rate and sorption rate equations at different temperatures were employed in a CFD model through a user-defined function (UDF) written in C and compiled with ANSYS Fluent solver. Results from the CFD model showed reasonable agreement with results of three experiments with sealed barrels that were empty, half-filled, or full of wheat with an AlP pellet placed in each barrel. The experimental and modeling results had similar curve characteristics and final concentrations that agreed within 30ppm with at least one of the replicates. The maximum deviations in the final concentrations between each replicate for the three cases (empty, half-filled, and full) were 157, 202, and 127ppm, respectively. These deviations showed the need for more experiments to evaluate the effects of temperature, wheat age and history, leakage, and other factors. A similar CFD model for full–size bins, based on this successful approach, can be used to establish

optimal strategies for grain fumigation with PH_3, as showed in Chapter 4.

In Chapter 4, CFD simulations were built that examine different physical configurations and important factors for PH_3 fumigation of bunkers. The CFD model was validated with published benchmarks on natural convection in porous media and experimental data from a full–scale grain bin subject to natural convection, leakage, and PH_3 absorption into wheat. Results from the CFD simulations agreed well with both the benchmark and the experimental data of the bin. The results, from the bunker simulations, identified several issues to improve bunker and phosphine fumigation design.

PH_3 release points are best placed under the tarpaulin and along the center of each side of the bunker. These points should be spaced at an interval of about one-eighth of the longest length of the bunker. An aspect ratio ARH (the ratio of the maximum height of the bunker to the half length of the bunker) of or around 0.5 showed better PH_3 distribution. Similarly, the ARh (the ratio of the height of the side wall to half the length of the bunker) of 0.1 gave better fumigant distribution results.

The PH_3 behavior was influenced significantly by leakage changes, however it is impossible to predict the actual value of the leakage rate or its location unless it is measured for a specific case. This is like the bin model in this study in which the actual locations of leakages were specified. With a small leakage, PH_3 loss increases as the inlet air flow rate increases. At high leakage rates, small flow re-circulation occurs around the outlet points and results in fluid blockages. As a result, PH_3 loss did not follow a specific trend with high flow rates.

Sorption did not affect the PH_3 distribution pattern. However, its rate is exponential so, the use of higher application rates may be useful. Finally, the bunker orientation or diurnal temperature variation may change the distribution pattern of PH_3, but the overall results showed that both diffusion and convection currents are not generally sufficient for spreading PH_3 in the entire bunker with a lethal dosage. As a result, further research on the effect of tarpaulin billowing on distributing fumigants in bunkers was needed.

Finally Chapter 5 investigated the effect of tarpaulin billowing on phosphine behavior in bunkers. FSI simulations were used to describe the effect of different wind conditions on the tarpaulin movement. The slice of the bunker which was used in all FSI cases was

based on a CFD external flow model built at three different Angle of Attack (AoA); 0°, 45°, 90°. The 0° angle of attack was chosen based on the pressure coefficient and its uniformity. The FSI investigated cases were; a constant velocity wind with different Reynolds numbers, oscillating velocity to mimic a real situation, and the effect of multiple bunkers on the tarpaulin motion. It was found that the main motion mechanism is sinusoidal regardless of the intensity or behavior of the inflow wind.

Based on the FSI simulation results, the tarpaulin motion was simplified mathematically according to the standing wave theory, in which its parameters can be adjusted to capture the actual amplitude and number of loops observed by tarpaulins. Coding this motion as a non-linear dynamic boundary gives flexibility to apply it on all or part of the bunker surface or even to define different motion parameters along the surface to mimic real scenarios. This makes it easier for other researchers to utilize this finding when simulating fumigants in specific bunkers.

A DNN model was coded to predict the mortality fraction, without further CFD simulations, as a function of the motion parameters (location of the moving wall, amplitudes, and number of loops) of the tarpaulin. The model predicts the mortality fraction with an R^2 of 0.985.

Tarpaulin billowing is a free and effective source for distributing PH_3 in bunkers. To be used properly, there should be more considerations while building bunkers. It is recommended that enough headspace be maintained for high amplitude, avoid crimps while tightening the tarpaulin, and smooth the grain surface as much as possible. If a dominant wind direction is known in a certain location, bunkers should be built in such a way that they face a zero angle of attack with the incoming wind to generate more uniform distribution for the PH_3 and to force a small number of loops for the highest mixing energy. Bunkers have very long sides compared to their width which make it difficult to control leakage compared to other storage facilities such as bins. A better sealing mechanism needs to be developed to avoid highly uncontrolled and unexpected leakages. Without following those recommendations, fumigation processes in bunkers may be successful for some and fail for others, or with even the same bunker it may be successful sometimes and fail other times.

FSI models are complicated and time consuming. Building such models for each possible scenario in the field is unrealistic, especially with the large volume of bunkers. The CFD model, with the non-linear moving boundary and dynamic mesh, can be tailored to capture specific scenarios. Robust experimental data are needed along with various CFD simulations proposed in this study. This should be followed by a reliable deep learning model that indicates a reasonable application rate for a successful fumigation process in bunkers. The model can be used as a computer or phone application based on longitude and latitude of the bunker, weather conditions and so on with no need for extra CFD analysis or experimental measurements. The CFD simulations may help in building an artificial network model that predicts both the spatial and temporal variation of PH_3 in bunkers, subject to different wind conditions, or any other variables.

6.1 Significance and contribution

The evolution rate of phosphine from its solid form (aluminum phopshide tablets or pellets) as a function of temperature, relative humidity, and number of tablets was developed. This can be used in other CFD modeling and for estimating the time it takes for tablets to decompose under different conditions. The variable that accounts for the change in phosphine sorption rate into wheat due to temperature was found. This can be used for modeling or estimating phosphine sorption in wheat under different temperatures. Detailed discussion on the wheat resistance to gas flow was provided with quantitative comparisons between all the available correlations in literature. This also can be used in other CFD modeling to avoid over estimating fumigant for accurate results. A new technique on estimating the resistance coefficient of wheat to gas flow was introduced. This technique can be applied to any type of grain and can reveal the detailed information that experiments cannot on the contribution of all factors that affect the resistance. A detailed analysis on the proper scaling of the effective diffusion coefficient was introduced and can be used by other researchers to avoid misleading results. In general, the CFD model and technique provided in this study can be applied to any grain storage facility.

The effect of tarpaulin motion on the phosphine behavior was unknown and experiments failed to describe information on this behavior. Results from this study showed the phosphine response to different motion parameters for the first time. Based on the results, recommendations for achieving a successful fumigation process in bunkers were given. The modeling technique based on the standing wave theory as a non-linear boundary provided in this study, can be applied to any motion mechanism that may be observed on a tarpaulin in the field. It can be used by other researchers to study different tarpaulin motions on phosphine distribution in bunkers. The DNN model can be generalized with more scenarios and used as a phone or computer application.

6.2 Limitations

- The focus of this study was only on phosphine gas as a fumigant and wheat as the grain.
- Only one bunker orientation (normal to the flow) was considered.
- The wheat surface was assumed to be smooth and uniform.
- The effect of the motion of part of the tarpaulin on phosphine distribution in bunkers was not investigated.
- The DNN model that predicts the mortality fraction as a function of different motion parameters is limited to number of loops between 0 and 10 and an amplitude of 0 and 0.07 m.

6.3 Recommendations for future work

Robust experiments on phosphine distribution in bunkers are needed to generalize the results. The CFD technique provided here can be applied to generate more data along with the

experiments. Both results can be used in a DNN model and used by workers in the filed to predict the successful rate of each fumigation process.

Bibliography

Afful, E., Elliott, B., Nayak, M. K., and Phillips, T. W. (2018). Phosphine resistance in north american field populations of the lesser grain borer, Rhyzopertha dominica (Coleoptera: Bostrichidae). *Journal of Economic Entomology*, 111(1):463–469.

Agrafioti, P., Kaloudis, E., Bantas, S., Sotiroudas, V., and Athanassiou, C. G. (2020). Modeling the distribution of phosphine and insect mortality in cylindrical grain silos with computational fluid dynamics: Validation with field trials. *Computers and electronics in agriculture*, 173:105383.

Annis, P. and Banks, H. (1993). A predictive model for phosphine concentration in grain storage structures. In Navarro, S. and Donahaye, E., editors, *Proceedings of the International Conference on Controlled Atmospheres and Fumigation of Grain Storages*, pages 299–312. Caspit Press.

ASABE Standards (2016). ASAE D272.3 MAR1996 (R2021): Resistance to airflow of grains, seeds, other agricultural products, and perforated metal sheets. Standard, American Society of Agricultural and Biological Engineers, St. Joseph, MI, USA.

Bakker-Arkema, F., Patterson, R., and Bickert, W. (1969). Static pressure-airflow relationships in packed beds of granular biological materials such as cherry pits. *Transactions of the ASAE*, 12(1):134–0136.

Banks, H. (1986). Sorption and desorption of fumigants on grains: Mathematical descriptions. In Champ, B. and Highley, E., editors, *Pesticides and Humid Tropical Grain Storage Systems: Proceedings of International Seminar, Manila, Philippines*, number 14, pages 179–193. Australian Centre for International Agricultural Research, Canberra.

Banks, H. (1991). Influence of water and temperature on release of phosphine from aluminium phosphide-containing formulations. *Journal of stored products research*, 27(1):41–56.

Bartosik, R. and Maier, D. (2006). Effect of airflow distribution on the performance of NA/LT in-bin drying of corn. *Transactions of the ASABE*, 49(4):1095–1104.

Baytas, A. C. and Pop, I. (1999). Free convection in oblique enclosures filled with a porous medium. *International Journal of Heat and Mass Transfer*, 42(6):1047–1057.

Bejan, A. (1979). On the boundary layer regime in a vertical enclosure filled with a porous medium. *Letters in Heat and Mass Transfer*, 6(2):93–102.

Bhardwaj, R. and Mittal, R. (2012). Benchmarking a coupled immersed-boundary-finite-element solver for large-scale flow-induced deformation. *AIAA journal*, 50(7):1638–1642.

Bolton, D. (1980). The computation of equivalent potential temperature. *Monthly weather review*, 108(7):1046–1053.

Braga, E. J. and de Lemos, M. J. (2004). Turbulent natural convection in a porous square cavity computed with a macroscopic κ–ε model. *International Journal of Heat and Mass Transfer*, 47(26):5639–5650.

Bruggeman, V. D. (1935). Berechnung verschiedener physikalischer konstanten von heterogenen substanzen. i. dielektrizitätskonstanten und leitfähigkeiten der mischkörper aus isotropen substanzen. *Annalen der physik*, 416(7):636–664.

Bundus, C., Jayas, D., Muir, W., White, N., and Ruth, D. (1996). Average convective-pore velocity of carbon dioxide gas through grain bulks. *Canadian Agricultural Engineering*, 38(2):91–98.

Carman, P. C. (1937). Fluid flow through granular beds. *Trans. Inst. Chem. Eng.*, 15:150–166.

Casada, M. and Young, J. (1994a). Heat and moisture transfer during transportation of shelled peanuts. *Transactions of the ASAE*, 37(6):1939–1946.

Casada, M. and Young, J. (1994b). Model for heat and moisture transfer in arbitrarily shaped two-dimensional porous media. *Transactions of the ASAE*, 37(6):1–1938.

Cavasin, R., DePalo, M., Tumambing, J., et al. (2006). Updates on the global application of Eco2Fume and Vaporph3OS® phosphine fumigants. In *Proceedings of the 9th International Working Conference on Stored-Product Protection, ABRAPOS, Passo Fundo, RS, Brazil, 15-18 October 2006*, pages 642–650. Brazilian Post-Harvest Association (ABRAPOS).

Chang, C., Converse, H., and Martin, C. (1983). Bulk properties of grain as affected by self-propelled rotational type grain spreaders. *Transactions of the ASAE*, 26(5):1543–1550.

Chapman, S. and Cowling, T. G. (1990). *The mathematical theory of non-uniform gases: an account of the kinetic theory of viscosity, thermal conduction and diffusion in gases*. Cambridge university press.

Chaudhry, M. (2000). Phosphine resistance. *Pesticide outlook*, 11(3):88–91.

Collins, P., Daglish, G., Nayak, M., Ebert, P., Schlipalius, D., Chen, W., Pavic, H., Lambkin, T. M., Kopittke, R., and Bridgeman, B. (2001). Combating resistance to phosphine in australia. In *International conference on controlled atmoshphere and fumigation in stored products*, volume 593, page 607. Executive Printing Services Fresno, CA.

Couch, L. S. and Shaheen, D. G. (1984). Hydrolysis rates of degesch hydrogen phosphide fumigants. Unpublished.

Cuomo, M. and Lanza, S. (2019). Design of a membrane structure subjected to blast load. In *Conference of the Italian Association of Theoretical and Applied Mechanics*, pages 1441–1458. Springer.

Daglish, G. J. and Pavic, H. (2008). Effect of phosphine dose on sorption in wheat. *Pest Management Science: formerly Pesticide Science*, 64(5):513–518.

Darby, J. A. (2008). A kinetic model of fumigant sorption by grain using batch experimental data. *Pest Management Science: formerly Pesticide Science*, 64(5):519–526.

Darby, J. A. (2011). Technology to overcome inadequate fumigations and resistance selection. Final Report CRC50059, Cooperative Research Centre for National Plant Biosecurity, Black Mountain, ACT, Australia.

Darcy, H. (1856). *Les fontaines publiques de la ville de Dijon: Exposition et application des principes à suivre et des formules à employer dans les questions de distribution d'eau: Ouvrage terminé par un appendice relatif aux fournitures d'eau de plusieurs villes, au filtrage des eaux et à la fabrication des tuyaux de fonte, de plomb, de tôle et de bitume*, volume 2. V. Dalmont.

De Nayer, G., Apostolatos, A., Wood, J. N., Bletzinger, K. U., Wüchner, R., and Breuer, M. (2018). Numerical studies on the instantaneous fluid–structure interaction of an air-inflated flexible membrane in turbulent flow. *Journal of Fluids and Structures*, 82:577–609.

Ergun, S. (1952). Fluid flow through packed columns. *Chem. Eng. Prog.*, 48:89–94.

Forchheimer, P. (1901). Wasserbewegung durch boden. *Z. Ver. Deutsch, Ing.*, 45:1782–1788.

Formato, A., Naviglio, D., Pucillo, G. P., and Nota, G. (2012). Improved fumigation process for stored foodstuffs by using phosphine in sealed chambers. *Journal of agricultural and food chemistry*, 60(1):331–338.

Giner, S. and Denisienia, E. (1996). Pressure drop through wheat as affected by air velocity, moisture content and fines. *Journal of Agricultural Engineering Research*, 63(1):73–85.

Glück, M., Breuer, M., Durst, F., Halfmann, A., and Rank, E. (2001). Computation of fluid–structure interaction on lightweight structures. *Journal of Wind Engineering and Industrial Aerodynamics*, 89(14-15):1351–1368.

Gross, R., Baer, M. R., and Hickox Jr, C. (1986). The application of flux-corrected transport

(FCT) to high rayleigh number natural convection in a porous medium. In *International Heat Transfer Conference Digital Library*. Begel House Inc.

Hackenberg, U. (1972). Chronic ingestion by rats of standard diet treated with aluminum phosphide. *Toxicology and Applied Pharmacology*, 23(1):147–158.

Haque, E. (2011). Void fraction as a function of depth and pressure drops of packed beds of porous media formed by granular materials. *Transactions of the ASABE*, 54(6):2239–2243.

Haque, E., Ahmed, Y., and Deyoe, C. (1982). Static pressure drop in a fixed bed of grain as affected by grain moisture content. *Transactions of the ASAE*, 25(4):1095–1098.

He, W. (2016). *Numerical Study of Effective Fumigation in Grain Storage Bunkers*. PhD thesis, University of Western Australia.

Hood, T. and Thorpe, G. (1992). The effects of the anisotropic resistance to airflow on the design of aeration systems for bulk stored grains. In *Conference on Engineering in Agriculture, 1992: Quality Soils, Quality Food, Quality Environment: Albury, N.S.W.4-7: Preprints of Papers*. Institution of Engineers, Australia.

Hukill, W. and Ives, N. (1955). Radial airflow resistance of grain. *Agricultural Engineering*, 36(5):332–335.

Hunter, A. (1983). Pressure difference across an aerated seed bulk for some common duct and store cross-sections. *Journal of Agricultural Engineering Research*, 28(5):437–450.

Isa, Z., Farrell, T., Fulford, G., and Kelson, N. (2016). Mathematical modelling and numerical simulation of phosphine flow during grain fumigation in leaky cylindrical silos. *Journal of Stored Products Research*, 67:28–40.

Jayas, D. and Muir, W. (1991). Airflow-pressure drop data for modeling fluid flow in anisotropic bulks. *Transactions of the ASAE*, 34(1):251–0254.

Jayas, D. and Sokhansanj, S. (1989). Design data on resistance of airflow through canola (rapeseed). *Transactions of the ASAE*, 32(1):295–0296.

Jayas, D., Sokhansanj, S., Moysey, E., and Barber, E. (1987). Airflow resistance of canola (rapeseed). *Transactions of the ASAE*, 30(5):1484–1488.

Jia, C.-C., Sun, D.-W., and Cao, C.-W. (2000). Mathematical simulation of temperature fields in a stored grain bin due to internal heat generation. *Journal of Food Engineering*, 43(4):227–233.

Kay, R., Bern, C. J., Hurburgh, C., et al. (1989). Horizontal and vertical airflow resistance of shelled corn at various bulk densities. *Transactions of the ASAE*, 32(2):733–0736.

Khatchatourian, O., Toniazzo, N., and Gortyshov, Y. (2009). Simulation of airflow in grain bulks under anisotropic conditions. *Biosystems Engineering*, 104(2):205–215.

Kheiralipour, K., Karimi, M., Tabatabaeefar, A., Naderi, M., Khoubakht, G., and Heidarbeigi, K. (2008). Moisture-depend physical properties of wheat (Triticum aestivum L.). *Journal of Agricultural Technology*, 4(1):53–64.

Kim, R.-w., Lee, I.-b., and Kwon, K.-s. (2017). Evaluation of wind pressure acting on multi-span greenhouses using CFD technique, part 1: Development of the CFD model. *Biosystems engineering*, 164:235–256.

Knight, J., Lucey, A., and Shaw, C. (2010). Fluid–structure interaction of a two-dimensional membrane in a flow with a pressure gradient with application to convertible car roofs. *Journal of wind engineering and industrial aerodynamics*, 98(2):65–72.

Kozeny, J. (1927). Uber kapillare leitung der wasser in boden. *Royal Academy of Science, Vienna, Proc. Class I*, 136:271–306.

Kumar, A. and Muir, W. (1986). Airflow resistance of wheat and barley affected by airflow direction, filling method and dockage. *Transactions of the ASAE*, 29(5):1423–1426.

Kumar, N., Khader, S. A., Pai, R., Khan, S., and Kyriacou, P. (2020). Fluid structure interaction study of stenosed carotid artery considering the effects of blood pressure. *International Journal of Engineering Science*, 154:103341.

Lage, J. (1992). Effect of the convective inertia term on bénard convection in a porous medium. *Numerical Heat Transfer*, 22(4):469–485.

Lauriat, G. and Prasad, V. (1989). Non-darcian effects on natural convection in a vertical porous enclosure. *International Journal of Heat and Mass Transfer*, 32(11):2135–2148.

Lawrence, J. and Maier, D. E. (2011). Three-dimensional airflow distribution in a maize silo with peaked, levelled and cored grain mass configurations. *Biosystems engineering*, 110(3):321–329.

Li, W. and Sokhansanj, S. (1994). Generalized equation for airflow resistance of bulk grains with variable density, moisture content and fines. *Drying Technology*, 12(3):649–667.

Lin, Z.-h., Li, X.-j., Jin, Z.-j., and Qian, J.-y. (2020). Fluid-structure interaction analysis on membrane behavior of a microfluidic passive valve. *Membranes*, 10(10):300.

Łukaszuk, J., Molenda, M., Horabik, J., Szot, B., and Montross, M. D. (2008). Airflow resistance of wheat bedding as influenced by the filling method. *Research in Agricultural Engineering*, 54(2):50.

McCabe, W. L., Smith, J. C., and Harriott, P. (1993). *Unit Operations of Chemical Engineering*, volume 5. McGraw-hill New York.

Millington, R. and Quirk, J. (1961). Permeability of porous solids. *Transactions of the Faraday Society*, 57:1200–1207.

Molenda, M., Montross, M. D., McNeill, S. G., and Horabik, J. (2005a). Airflow resistance of seeds at different bulk densities using ergun's equation. *Transactions of the ASAE*, 48(3):1137–1145.

Molenda, M., Qukaszuk, J., and Horabik, J. (2005b). Airflow resistance of wheat as affected by grain density and moisture content. *Agricultural Engineering*, 8(4):67.

Montross, M. D. and McNeill, S. G. (2005). Permeability of corn, soybeans, and soft red and white winter wheat as affected by bulk density. *Applied Engineering in Agriculture*, 21(3):479–484.

Morgan, V. T. (1975). The overall convective heat transfer from smooth circular cylinders. In *Advances in heat transfer*, volume 11, pages 199–264. Elsevier.

Namkoong, K., Choi, H., and Yoo, J. (2005). Computation of dynamic fluid–structure interaction in two-dimensional laminar flows using combined formulation. *Journal of fluids and structures*, 20(1):51–69.

Neethirajan, S., Jayas, D., White, N., and Zhang, H. (2008). Investigation of 3d geometry of bulk wheat and pea pores using x-ray computed tomography images. *computers and electronics in agriculture*, 63(2):104–111.

Neethirajan, S., Karunakaran, C., Jayas, D., and White, N. (2006). X-ray computed tomography image analysis to explain the airflow resistance differences in grain bulks. *Biosystems Engineering*, 94(4):545–555.

Nguyen, T. (1985). Movement of fumigants in bulk grain. *Pesticides and Humid Tropical Grain Storage Systems, eds. BR Champ and E. Highley*, pages 195–201.

Nguyen, T. (1987). Natural convection effects in stored grains - a simulation study. *Drying Technology*, 5(4):541–560.

Nield, D. A. and Bejan, A. (2017). *Convection in Porous Media*, volume 5. Springer.

Oxley, T. and Henderson, F. (1944). The properties of grain in bulk. i. instruments for making measurements in grain stored in bulk. *J. Soc. chem. Ind., Land*, 63:48.

Patterson, R., Bakker-Arkema, F., and Bickert, W. (1971). Static pressure-airflow relationships in packed beds of granular biological materials such as grain-ii. *Transactions of the ASAE*, 14(1):172–0174.

Phillips, T. W., Thoms, E., DeMark, J., and Walse, S. (2012). Fumigation. In Hagstrum, D. W., Phillips, T. W., and Cuperus, G., editors, *Stored Product Protection*, volume S156, chapter 14, pages 157–177. Kansas State University, Manhattan, Kansas.

Prasad, V. and Kladias, N. (1991). Non-darcy natural convection in saturated porous media. In *Convective heat and mass transfer in porous media*, pages 173–224. Springer.

Proudfoot, A. T. (2009). Aluminium and zinc phosphide poisoning. *Clinical toxicology*, 47(2):89–100.

Rajeshekar, Y., Vanitha Reddy, P., Khamrunissa, B., Leelaja, B., and Rajendran, S. (2006). Studies on aluminium phosphide tabled formulation. *Pestology*, 30(4):41–45.

Reddy, V. P., Rajashekar, Y., Begum, K., Chandrappa Leelaja, B., and Rajendran, S. (2007). The relation between phosphine sorption and terminal gas concentrations in successful fumigation of food commodities. *Pest Management Science: formerly Pesticide Science*, 63(1):96–103.

Schildhauer, M. and Spille-Kohoff, A. (2014). Numerical simulation of fluid-structure interaction: Turek benchmark and kinetics of a reed valve. *Progress in Computational Fluid Dynamics, an International Journal*, 14(1):38–48.

Shedd, C. K. (1953). Resistance of grains and seeds to air flow. *Agricultural Engineering*, 34(9):616–619.

Shunmugam, G., Jayas, D., White, N., and Muir, W. (2005). Diffusion of carbon dioxide through grain bulks. *Journal of Stored Products Research*, 41(2):131–144.

Singh, A. and Thorpe, G. (1993). A grid generation technique for numerical modelling heat and moisture movement in peaked bulks of grain. *Journal of food process engineering*, 16(2):127–145.

Singh, D., Muir, W., and Sinha, R. (1984). Apparent coefficient of diffusion of carbon

dioxide through samples of cereals and rapeseed. *Journal of Stored Products Research*, 20(3):169–175.

Singh, J. and Roy, A. K. (2019). Effects of roof slope and wind direction on wind pressure distribution on the roof of a square plan pyramidal low-rise building using cfd simulation. *International Journal of Advanced Structural Engineering*, 11(2):231–254.

Smith, E., Jayas, D., and Ville, A. d. (2001). Modelling the flow of carbon dioxide through beds of cereal grains. *Transport in porous media*, 44(1):123–143.

Stephens, L. and Foster, G. (1978). Bulk properties of wheat and grain sorghum as affected by a mechanical grain spreader. *Transactions of the ASAE*, 21(6):1217–1218.

Tan, X. (1994). Evolution of phosphine from aluminium phosphide formulations at various temperatures and humidities. In *Proceeding of the 6th international working conference on stored product protection*, volume 1.

Thorpe, G. (1981). Moisture diffusion through bulk grain. *Journal of Stored Products Research*, 17(1):39–42.

Thorpe, G. (2002). Airflow distribution in ventilated beds of grain. In Navarro, S. and Noyes, R. T., editors, *The Mechanics and Physics of Modern Grain Aeration Management*, volume 1, chapter 11, pages 585–614. CRC Press Inc.

Thorpe, G. R. (2008). The application of computational fluid dynamics codes to simulate heat and moisture transfer in stored grains. *Journal of stored products research*, 44(1):21–31.

Tipler, P. A. and Mosca, G. (2003). *Physics for Scientists and Engineers, Volume 1: Mechanics, Oscillations and Waves; Thermodynamics*. Macmillan.

Turek, S. and Hron, J. (2006). Proposal for numerical benchmarking of fluid-structure interaction between an elastic object and laminar incompressible flow. In *Fluid-structure interaction*, pages 371–385. Springer.

Van Brakel, J. and Heertjes, P. (1974). Analysis of diffusion in macroporous media in terms of a porosity, a tortuosity and a constrictivity factor. *International Journal of Heat and Mass Transfer*, 17(9):1093–1103.

Waterford, C., Whittle, C., and Winks, R. (1994). New aluminum phosphide formulations for controlled generation of phosphine. In *Proceedings of the 6th International Working Conference on Stored-product Protection*, volume 1, pages 226–230.

White, F. M. (2006). *Viscous Fluid Flow*, volume 3. McGraw-Hill New York.

Wrigley, C. W., Corke, H., Seetharaman, K., and Faubion, J. (2015). *Encyclopedia of Food Grains*. Academic Press.

Wüchner, R., Kupzok, A., and Bletzinger, K.-U. (2007). A framework for stabilized partitioned analysis of thin membrane–wind interaction. *International journal for numerical methods in fluids*, 54(6-8):945–963.

Yang, X. and Williams, D. (1990). Airflow resistance of grain sorghum as affected by bulk density. *Transactions of the ASAE*, 33(6):1966–1970.

Žukauskas, A. (1972). Heat transfer from tubes in crossflow. In *Advances in heat transfer*, volume 8, pages 93–160. Elsevier.

Appendix A

Extra Material

A.1 Inhomogeneous porosity with anisotropic resistance

Chapter 2, discussed that foreign material can cause inhomogeneous porosity in a grain storage space. Figure A.1 shows this concept applied on a 2D bunker shape; (a) shows the contours of porosity (a) along with the variation of the porosity in the horizontal direction, (b) the contours and contour lines of the viscous resistances (b, c), and the contours and contour lines of the inertial resistances (d, e). These resistances are for coefficients of Molenda et al. (2005a) in the vertical direction and 70% (ASABE Standards, 2016) of that for the resistances in the horizontal direction. It can be seen that with the low porosity towards the center of the bunker, higher resistances were occurred. The contour lines of the viscous resistance (c) are of straight vertical lines, while for the inertial resistance (e) has the non-linearity behavior in it.

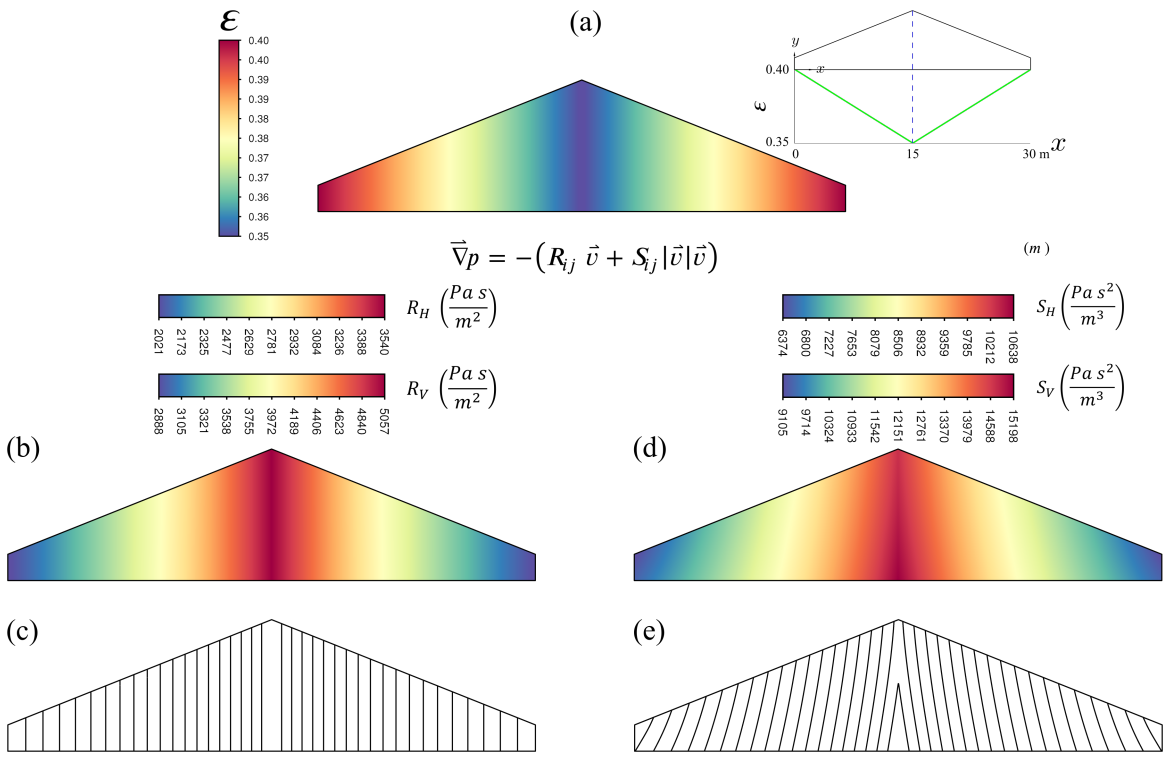

Figure A.1: Porosity contours along with its linear function (a), the viscous (b, c) and inertial (d, e) resistances to airflow of an inhomogeneous porosity. (c, d) are the contour lines.

A.2 Corn resistance to airflow - CFD test

In Chapter 2, Section 2.2.3 a CFD implementation test was discussed for wheat. To test the applicability of the CFD model on a different grain, a bin of corn with available experimental data (Bartosik and Maier, 2006) was chosen. The same experiment was investigated through CFD simulations by Lawrence and Maier (2011) and was concluded that a porosity that varies (inhomogeneous porosity) linearly along the horizontal axes is reasonable in predicting the air velocity at the grain surface. In this simulation, the resistance coefficients, and the volume equivalent diameter of corn (6.23×10^{-3} m) at 14.6% moisture content were obtained from Molenda et al. (2005a). A linear function of porosity that varies from 0.35 (center) to 0.4 (bin surface) in the radial direction was employed. Experiment#14 ((Bartosik and Maier, 2006)) was selected. The velocity, as inlet boundary conditions, was calculated from the flow rate per tonne of grain. In that experiment, the grain height is 4.9 m and the bin

diameter is 8.3 m. There was no change in the velocity and pressure in the circumferential direction, as a result, the CFD model was assumed to be 2D axisymmetric in which the circumferential derivatives of $\vec{v}$ and p are zeros. Figure A.2 shows both the velocity (a) and pressure (b) contours of the simulation of the bin filled with corn. The velocity here represents the superficial velocity. The inlet velocity based on the flow rate per tonne of grain for experiment#14 is 0.067 m s^{-1}.

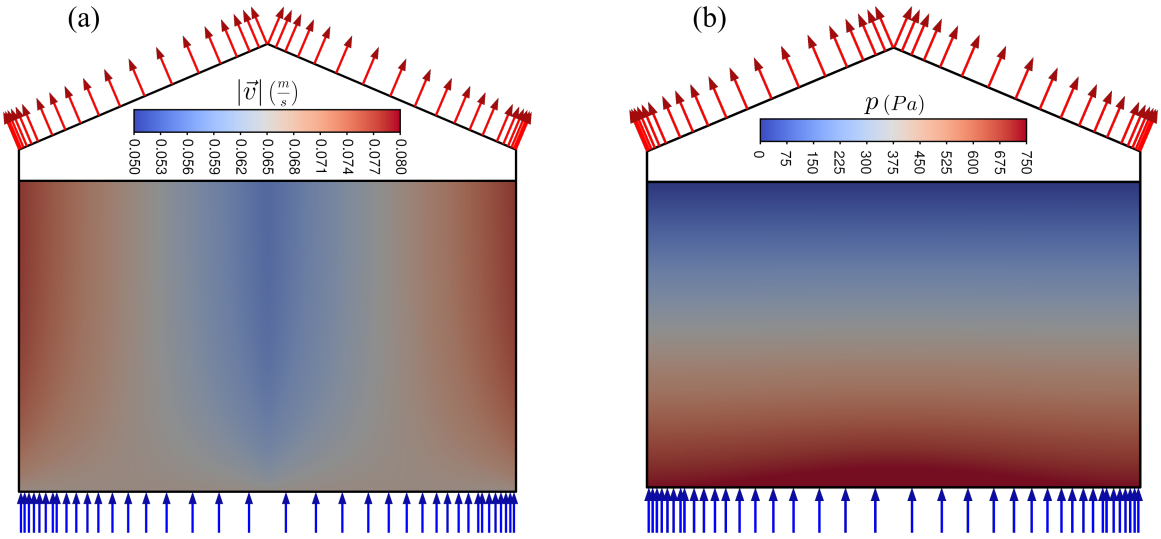

Figure A.2: Contours of velocity (a) and pressure (b) of the bin of corn simulation.

A comparison between the CFD results and the experimental data of Bartosik and Maier (2006) for the velocity at the surface of the corn is shown in Figure A.3. Results show a good agreement which ensures the applicability of the CFD model to capture other grains in other storage facilities.

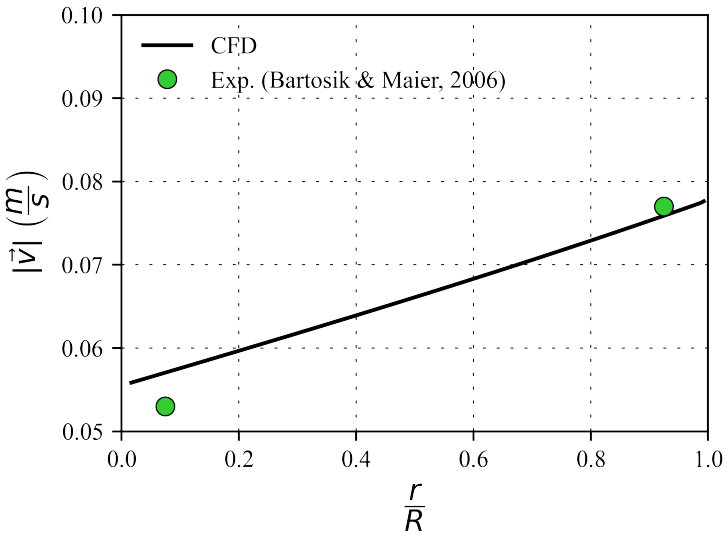

Figure A.3: Magnitude of velocity ($\mathrm{m\,s^{-1}}$) along the non-demonopolized radius of the bin resulted from the CFD simulation (—) compared to the experimental data of Bartosik and Maier (2006) (●).

Figure A.4. shows that an average porosity between the low and high could be used and results of the pressure drop will be identical to results when using a linearly varying porosity. This can be applied in simulating bunkers in which higher resistance can substitute the effect of varying porosity.

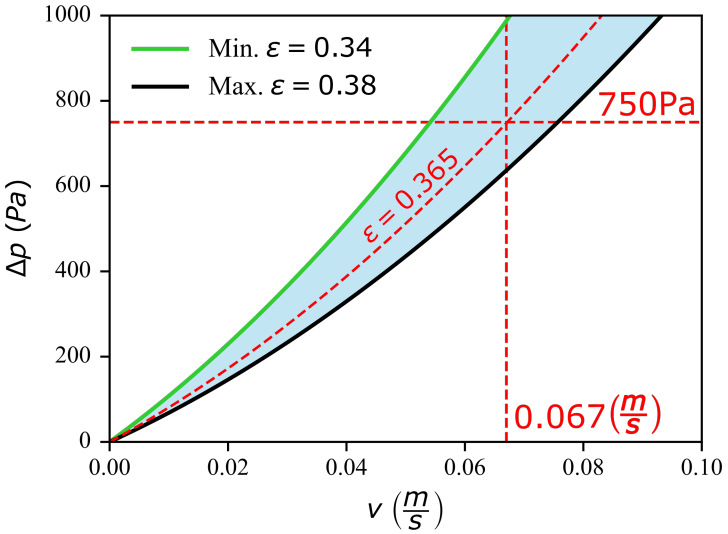

Figure A.4: Pressure drop (Pa) vs velocity ($\mathrm{m\,s^{-1}}$) using coefficients of Molenda et al. (2005a) for corn at three different porosities; minimum (ε = 0.34 —), average (ε = 0.365 - - -), and maximum (ε = 0.365 —).